AD-A278 142

‖‖‖‖‖‖‖‖‖‖

QUANTITATIVE MODELING OF BOTTOM
MORPHOLOGY AND SUBBOTTOM PROPERTIES

FINAL TECHNICAL REPORT

TO THE OFFICE OF NAVAL RESEARCH

GRANT NO: N00014-90-J-1584

NOVEMBER 1989 - MAY 1993

DTIC
S **ELECTE**
APR 1 4 1994
F **D**

Thomas H. Jordan, Principal Investigator

Department of Earth, Atmospheric and Planetary Sciences
Massachusetts Institute of Technology
77 Massachusetts Avenue
Cambridge, MA 02139

94-11226

‖‖‖‖‖‖‖‖‖‖‖‖‖‖‖

DTIC QUALITY INSPECTED 5

94 4 12 144

Objective

The objectives of this research were threefold: (1) to provide the methodology needed to quantify the two-dimensional variations in bottom topography and three-dimensional variations in subbottom properties observed within the ARSRP Central Atlantic study area; (2) to apply this methodology to geological data sets collected in the study area; and (3) to use the resulting geological models to understand the bottom reverberations observed at long ranges across the study area and other parts of the deep ocean.

Background

Previous research by marine morphologists, including the work done by the P.I. and his colleagues [Goff and Jordan, 1988, 1989a,b, 1990; Goff, Jordan, Edwards, and Fornari, 1991], has demonstrated that realistic models of the seafloor can be formulated by combining deterministic descriptions of large-scale features with stochastic parameterizations of small-scale features. Most of the analyses done to date, however, have concentrated on stochastic descriptions of the hard-rock topography generated by seafloor spreading at ridge crests. In particular, little attention has been given to the variations of topography and subbottom properties caused by sedimentation and post-depositional sediment transport, which play a major role in controlling the subsurface properties of the seafloor, including elastic and anelastic properties, porosity, and permeability. A major focus of our recent research has been to develop methods for describing sediment distributions on a rough seafloor and to incorporate these descriptions into environmental models.

Approach

We first prescribe *sediment deposition and post-depositional transport* by a simply parameterized model and solve the *forward problem*: given the values of the parameters, which include a description of the underlying basement topography, predict the sediment distribution and observable aspects of seafloor structure. The observables are (1) the bathymetry of the sediment-water interface obtained by a multibeam swath-mapping system, and (2) the apparent sediment thickness measured from a single-channel 3.5-kHz echosounder and/or seismic profiler. We then set up and solve the *inverse problem*: given these observations and a description of their uncertainties, estimate the model parameters. Finally, we *evaluate and interpret* the results: if the fit to the data is satisfactory, we proceed with a geological interpretation of the model; if not, we seek modifications to our parameterizations that deliver better descriptions of the data, and we return to the inversion step.

Results

The results during this period of performance period are described in the following documents; which are included as sections 1, 2 and 3 of this report:

Section 1: Webb, Helen F. and Thomas H. Jordan, Quantifying the Distribution and T ansport of Pelagic Sediments on Young Abyssal Hills, submitted to *Geophys. Res. Lett.* May 14, 1993.

Section 2: Webb, Helen, Modeling Sedimentation of a Rough Seafloor, submitted as partial fulfillment of the requirements of the Generals Examination, MIT/WHOI Joint Program in Oceanography, advised by Thomas H. Jordan, August 5 1992.

Section 3: Goff, John A., Helen F. Webb and Thomas H. Jordan, Stochastic Interpolation of Wide-Beam Bathymetric Profile Within the ONR-ARSRP Acoustic Reverberation Corridor, *Office of Naval Research S.R.P. on Acoustic Reverberation,* Technical Report No. 2, 1992.

Our basic forward-modeling tools are efficient numerical algorithms for characterizing the sediment distribution on very rough (fractal) models of seafloor topography. Sediment-particle dynamics are described by a diffusive redistribution process in which the diffusivity parameter κ and the sediment flux rate F can vary in time and space. We have developed a 3D version of the algorithm and implemented it on a massively parallel supercomputer, the NRL 8000-processor Connection machine [Webb and Jordan, 1992a]. Numerical simulations have been run for various values of κ, F, and the five parameters of a Goff-Jordan description of the underlying basement topography. From a stochastic analysis of these simulations, we have constructed the functional relationships between the model parameters and two sets of observables: (1) the apparent RMS height $\bar{H}$, apparent characteristic wavenumber $\bar{k}$, and apparent fractal dimension $\bar{D}$ estimated from a multibeam swath by the inversion algorithm of Goff and Jordan [1988], and (2) the cumulative slope distribution function $P(s,\Delta x)$ estimated from a single-channel, narrow-beam echosounder sampled with a horizontal spacing Δx.

Using these functional relationships, we have inverted the data collected by the *R/V Ewing* Hydrosweep multibeam system during the ARSRP Geology and Geophysics Reconnaissance Cruise in Jul-Aug, 1992. The preliminary map of the average sediment load L (the time integral of F) for the ARSRP survey region is shown in Fig. 1. We note that L is highly variable across the study area, reflecting spatial variations in sea-floor age, variations in F controlled by temporal variations in the CCD, and lateral transport of sediments controlled by large-scale variations in bottom topography.

We also developed a DAT-based system for the digitization and playback of 3.5-kHz profiler returns. This system was installed on *R/V Ewing* and successfully collected data continuously during the ARSRP Geology and Geophysics Reconnaissance Cruise. These data will be analyzed for small-scale variations in reflectivity associated with volumetric heterogeneities in sediment ponds, to be used as input to numerical simulations of sediment backscattering by the ARSRP Modeling Group.
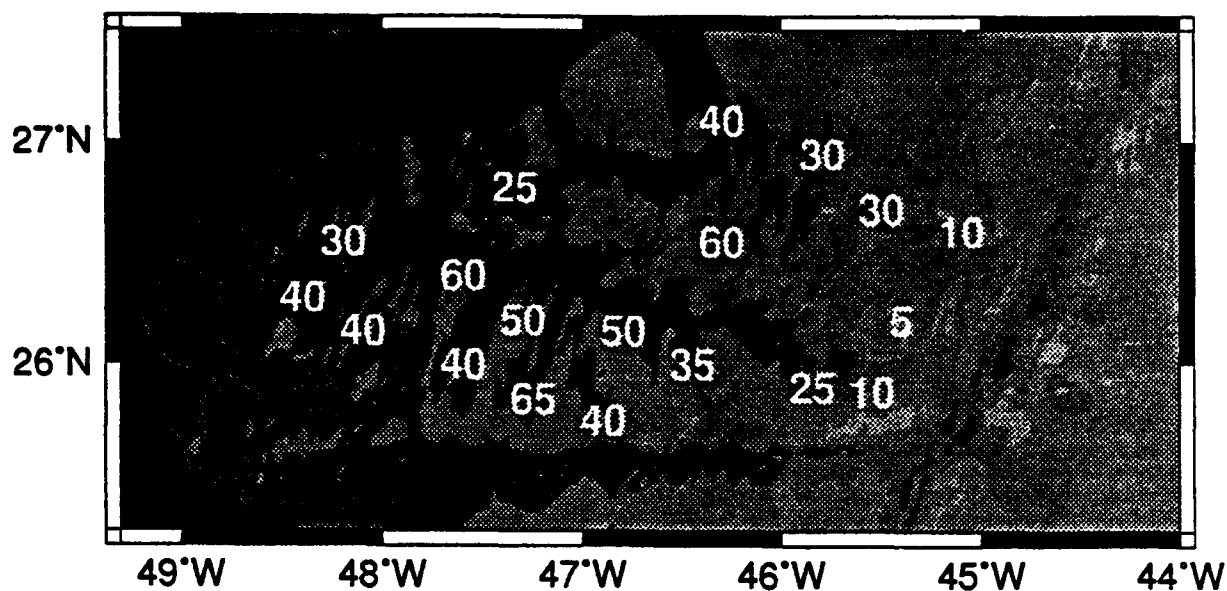
FIGURE 1. A preliminary map of the average sediment load L, shown by the numbers in meters, obtained by inverting multibeam slope-distribution data collected for the ARSRP survey region in Jul-Aug, 1992. L is highly variable across the study area, reflecting spatial variations in sea-floor age, variations in F controlled by temporal variations in the CCD, and lateral transport of sediments controlled by large-scale variations in bottom topography. The data from some areas, including the large "Site A" sediment pond (46.3°W, 26.3°N), have not been analyzed.

QUANTIFYING THE DISTRIBUTION AND TRANSPORT OF PELAGIC SEDIMENTS ON YOUNG ABYSSAL HILLS

HELEN F. WEBB AND THOMAS H. JORDAN

Department of Earth, Atmospheric and Planetary Sciences, MIT, Cambridge.

Abstract. In pelagic environments, the redistribution of sediments can be modeled as a diffusive process in which material is transported from topographic highs to lows at a rate determined by an apparent diffusivity κ. We have developed a statistical methodology for estimating the κ together with the average sediment load L and the root-mean-square height H of the abyssal-hill basement. Our approach is to generate synthetic basement topographies based on the Goff-Jordan description of abyssal-hill morphology, distribute sediments over these topographies according to the diffusion assumption, and calculate the slope distributions of the resulting sediment-water interfaces; we then determine κ, L, and H by fitting the slope-distribution function to the values observed from narrow-beam bathymetric profiles. The local values of these parameters have been derived from center-beam Hydrosweep data collected on young (5–25 Ma) abyssal hills in the Acoustic Reverberation Special Research Project corridor on the west flank of the Mid-Atlantic Ridge. The average value of the apparent diffusivity is $\overline{\kappa} = 0.13 \pm .014$ m^2/yr, which is the first determination of this parameter in a deep-sea environment. H varies between 188 and 285 m, with a mean of 230 ± 7 m. L is estimated to be as thin as 10 m on 5-Ma crust near the ridge crest, thickening to values of greater than 50 m at 10–15 Ma and then decreasing to less than 30 m on 25-Ma crust in the western portion of the corridor. The decrease in sediment load with age may be associated with a shallower carbonate compensation depth prior to the late Miocene, hypothesized by previous authors. The trends in our sediment-load estimates agree with single-channel data collected in the region.

INTRODUCTION

Pelagic sedimentation is the primary modifier of seafloor topography on the flanks of the mid-ocean ridges, smoothing and eventually burying the abyssal hills generated by seafloor spreading. Understanding the distribution of sediments on young seafloor and the processes that govern their post-depositional transport are central problems in marine morphology. Thin pelagic sediments are notoriously difficult to study, however, because the scattering by rough abyssal-hill topography obscures the wide-beam sediment profiles obtained from surface ships. In this report, we outline a new methodology for quantifying sediment distribution and transport that utilizes only bathymetric data routinely collected by narrow-beam echosounders.

Considered in detail, the processes that govern deep sea sedimentation, such as the generation of small-scale turbidity currents, the interactions of bottom currents with pre-existing topography, and bioturbation, are complex. But averaged over geological time, these processes act to transport sediments from topographic highs to topographic lows at all scales [e.g. Marks, 1981]. We therefore model sedimentation as a simple diffusive process in which the lateral flux of sediments is proportional to the local topographic gradient [Culling, 1960]. Diffusion models have been used to explain the evolution of scarp-like landforms [Hanks et al., 1984], as well as the stratigraphy found in foreland basins [Flemings and Jordan, 1989] and shallow marine settings [Kaufman et al., 1991]. To our knowledge, however, sedimentation in pelagic environments has not been addressed from this perspective.

FORWARD MODELING

Let $h(x,t)$ be the height of a durable basement $b(x)$ covered by an erodible layer of sediment $s(x,t)$, let $F(x,t)$ be the sedimentation rate, and let κ be the diffusivity of lateral sediment transport. The sediment transport equation is

$$\frac{\partial s}{\partial t}(x,t) = \kappa \nabla_x^2 h(x,t) + F(x,t) \tag{1}$$

where ∇_x^2 is the surface Lapacian. Eqn. (1) is to be solved for $h(x,t) = b(x) + s(x,t)$ subject to

---

the constraint that $s(x,t) \geq 0$. The inequality makes the problem highly non-linear. Complexity is also introduced by the structure of the basement topography $b(x)$, which has a fractal character.

We have obtained representations of the sediment-water interface by numerically integrating (1), starting from basement topographies generated as realizations of the stochastic process of Goff and Jordan [1988, 1990]. The Goff-Jordan model represents the seafloor as a spatially stationary, anisotropic Gaussian random field specified by five parameters: the root-mean-square (rms) height H, the characteristic length λ_s and width λ_n of the abyssal hills, the abyssal-hill azimuth ζ_s, and a fractal dimension D. For the applications discussed here, we fixed the scale lengths and fractal dimension at values typical of the western flank of the Mid-Atlantic Ridge [Goff and Jordan, 1990; J. Goff, personal communication, 1992]: $\lambda_s = 22$ km, $\lambda_n = 5.4$ km, and $D = 2.2$.

The computations were performed on the Naval Research Laboratory's CM-2 Connection Machine using a horizontal grid with dimensions of 100 km $\times$ 100 km and a grid point spacing of $\Delta x = 100$ m. The flux rate F was assumed to be constant in space and time, so that the total sediment load for a seafloor of age T is $L = FT$. In this case, the diffusivity scales as $\kappa = KL^2/T$, where K is a dimensionless diffusivity. Synthetic topographies were calculated for $L \leq 100$ m for a wide range of K, T, and H.

<center>PARAMETER DETERMINATION</center>

Two examples of our calculations are shown in Figure 1. Low values of κ produce seafloor morphologies in which sediments drape hillsides, while higher values transport the sediments downslope, exposing the peaks and creating flat sediment ponds. This behavior is reflected in the slope distribution, which is a sensitive indicator of deviations from the Gaussian character assumed for the basement topography [Shaw and Smith, 1990]. For a profile of constant orientation with respect to the topographic axis ζ_s, sampled at a constant horizontal interval u, we define the cumulative slope distribution function $S(\theta,u)$ as the fraction of profile length with an apparent slope angle, $\arctan[(h(x+u)-h(x))/u]$, less than θ.

$S(\theta,u)$ can be estimated directly from single-channel, narrow-beam echograms and, as illustrated in Figure 2, its shape is diagnostic of H, L, and κ. For large values of the

dimensionless diffusivity and for sediment loads that are a significant fraction of the basement topography, the ponds are well defined, and $S(\theta,u)$ displays a sharp kink at a slope angle θ_0 that separates the ponds from hillsides; i.e., $S(\theta_0,u)$ measures the fraction of the profile occupied by ponded sediments. This fraction decreases as L decreases and the rate of this decrease is most rapid when L/H is small. The slope of $S(\theta,u)$ at $\theta << \theta_0$ is sensitive to κ, and the slope of $S(\theta,u)$ at $\theta >> \theta_0$ depends primarily on H. In other words, by least-squares fitting the theoretical values of $S(\theta,u)$ to the observed values, we can determine H, L, and κ. Although the results are conditional on the values assumed for λ_s, λ_n, and D, which we have fixed in our inversions, numerical experiments show that $S(\theta,u)$ is only weakly dependent on these additional parameters.

APPLICATION TO THE ARSRP CORRIDOR

This procedure has been tested on a data set collected during Cruise 9208 of the R/V Maurice Ewing (14 Jul–18 Aug 92) as part of the Office of Naval Research (ONR) Acoustic Reverberation Special Research Project (ARSRP). The study area is shown in Figure 3; it occupies 75,000 km^2 on the west flank of the Mid-Atlantic Ridge north of the Kane Fracture Zone and comprises crust with ages ranging from 3 to 30 My. The underway geophysical data collected in digital format during the survey include Atlas Hydrosweep multibeam bathymetry, Hawaii MR1 sidescan sonar, magnetometer and gravimeter profiles, 3.5-kHz echosoundings, and single-channel watergun profiles [Tucholke et al., 1993]. The track lines were run at an average speed of 9.8 knots on a WSW-ENE trending grid subparallel to plate flow lines with a spacing that varied from 4-6 kilometers near the ridge crest to 8-9 kilometers in deeper water, a configuration designed to optimize the bathymetric coverage and insonification of the dominant topographic grain. Global Positioning System navigation was available throughout the survey.

The primary data employed in this study are the interpolated depth values logged each minute from the center beam of the Hydrosweep system. The average along-track spacing between data points is ~300 m, which we took as the value of u in calculating the slope statistics. Based on a detailed examination of the swath maps, the track segments were grouped into 19 small areas (1000–3000 km^2) where the statistical character of the abyssal hills was more or less

homogeneous. We avoided regions where the abyssal hills were interrupted by ridge-segment boundaries, which are typified by deeper bathymetry, thicker sediments, and inhomogeneous statistics [Tucholke et al., 1993]. The track lengths in each area varied from 130 km to 360 km, with an average of about 200 km. Average crustal ages were determined from the magnetic-anomaly data processed by M. Tivey [personal communication, 1993].

H, L, and κ were estimated for each area by fitting the center-beam slope distributions using a weighted least-squares algorithm; the results plotted as numbers on Figure 3. In Figure 4, we illustrate how the slope-distribution data for the area centered at 26.0° N, 46.5° W are matched by the theoretical model, and we display the resulting uncertainties in the model parameters by contouring their 95% confidence region. The best estimates are $H = 220 \pm 7$ m, $L = 34 \pm 3$ m, and $\kappa = 0.09 \pm .02$ m^2/yr. The relative sizes of the standard errors (4%, 10%, and 20%, respectively) are typical of the other areas. The confidence regions deviate from an elliptical shape, reflecting the non-Gaussian character of the estimation uncertainties. Their basic properties can be easily understood from the variations shown in Figure 2. The strong, positive correlation between H and L, for example, is related to the smoothing of the topography by the sediments; e.g., a large value of $S(\theta_o, \mu)$ may correspond either to thin sediments on low-amplitude basement or to thick sediments on high-amplitude basement. There is essentially no tradeoff between L and κ, although the 95% confidence region for the latter is distinctly asymmetric. The upper bound on the diffusivity is less well constrained than its lower bound, because the part of the slope distribution sensitive to κ becomes compressed to smaller values of θ as κ increases.

With these uncertainties in mind, we turn our attention to the regional differences evident in Figure 3. H varies from 188 m to 285 m, with a mean $\bar{H} = 230 \pm 7$ m. The variation is not large, but it does correlate with the ridge-segment boundary that passes through the center of the corridor. The average abyssal-hill amplitude in the seven areas north of the segment boundary is significantly larger ($\bar{H} = 255 \pm 12$ m) than in the twelve areas to the south ($\bar{H} = 214 \pm 5$ m), implying a persistent discontinuity in the ridge-crest processes that give rise to the abyssal-hill topography. In contrast, the variation in L is primarily in an east-west direction, along the plate flow lines. In Figure 5, we plot the sediment load as a function of crustal age. It is thin on the young crust near the ridge crest, increasing westward to maximum thicknesses as high as 55 m on

crust with ages of 10-15 Ma. A least-squares regression of the data out to 12 Ma yields an apparent sedimentation rate of 3.4 m/My.

On older seafloor, L decreases with age, dropping to values as low as 20 m at 25 Ma. This observation agrees with the 3.5-kHz and single-channel seismic data collected during the ARSRP survey. A detailed discussion of the trends in Figure 5 is beyond the scope of this initial report, but we note that the non-monotonic character of L can plausibly be related to a change in the carbonate compensation depth (CCD). Tucholke and Vogt [1979] have hypothesized that, prior to the late Miocene, the CCD in the central North Atlantic was shallower. According to their Figure 3, the most rapid change in the CCD occurred in the mid-Miocene, which coincides with the sediment peak observed in our data. Carbonates dominate the upper-ocean sediment flux in this region, and their rate of dissolution would have been greater prior to this time. Taken at face value, however, the rapid decrease in L between 15 and 25 Ma is inconsistent with a constant CCD and sediment flux throughout the early Miocene. One possibility is that the CCD at the end of the Oligocene was even shallower than Tucholke and Vogt have estimated, and that the period over which it deepened included the early Miocene.

The individual areas show apparent diffusivities ranging from 0.04 to 0.26 m^2/yr. Some variation in this parameter is evidently warranted by the data; attempts to fit the data with a constant value of κ led to unsatisfactory results, consistent with the error analysis in Figure 4, which indicates that the observed order-of-magnitude change should be resolvable. The physical significance of the differences, if any, is unclear. No pattern emerges from Figure 3, for example. The mean values north and south of the segment boundary are statistically identical ($0.15 \pm .020$ and $0.12 \pm .019$ m^2/yr, respectively), as are those east and west of 47° W ($0.13 \pm .017$ and $0.13 \pm .023$ m^2/yr). The estimates of L and κ, like those of L and H, are uncorrelated.

More important, the mean value of the apparent diffusivity obtained from the cumulative slope distributions is precisely estimated by our technique: $\bar{\kappa} = 0.13 \pm .014$ m^2/yr. To our knowledge, this is the first quantitative estimate of sediment diffusivity in a deep-sea environment. For comparison, we note that pelagic sediments in the central North Atlantic are transported at a rate about two orders of magnitude greater than compacted sediments in arid regions, where $\kappa \approx 10^{-3}$ m^2/yr [e.g. Hanks et al., 1984], but several orders of magnitude less rapidly than those in deltaic

and near-shore marine settings, which yield apparent diffusivities of $\sim 10^4 \ m^2/yr$ [e.g. Flemings and Jordan, 1989].

DISCUSSION

Our methodology obtains good estimates of the sediment load, apparent diffusivity, and rms amplitude of the basement topography from single-channel, narrow-beam echosounding profiles in rough abyssal-hill terrains where standard sediment profiling techniques cannot be applied. Although the diffusion approximation used to invert for these parameters undoubtedly oversimplifies the processes that govern post-depositional transport, it represents a first step towards a dynamical model of sedimentation on young oceanic crust. Application of the statistical techniques presented here to dense, high-quality data sets like those being collected in the ARSRP corridor will lay the foundation for future improvements. In the short term, however, using them to process existing narrow-beam data may be helpful in mapping the distribution of sediments on the flanks of the mid-ocean ridges.

REFERENCES

Culling, W. E. H., Analytical theory of erosion, *J. Geol.*, *68*, 336-344, 1960.

Flemings, P. B. and T. E. Jordan, A synthetic stratigraphic model of foreland basin development, *J. Geophys. Res.*, *94*, 3851-3866, 1989.

Goff, J. A. and T. H. Jordan, Stochastic Modeling of Seafloor Morphology: Inversion of Sea Beam data for second-order statistics, *J. Geophys. Res.*, *93*, 13589-13608, 1988.

Goff, J. A. and T. H. Jordan, Pacific and Atlantic models of small-scale seafloor topography, *Office of Naval Research S. R. P. on Acoustic Reverberation*, Technical Report No. 1, 1990.

Hanks, T. C., R. C. Bucknam, K. R. Lajoie, and R. E. Wallace, Modification of wave-cut and faulting-controlled landforms, *J. Geophys. Res., 89*, 5771-5790, 1984.

Kaufman, P., J. P. Grotzinger and D. S. McCormick, Depth-dependent diffusion algorithm for simulation of sedimentation in shallow marine depositional systems, *Kansas Geological Survey Bulletin 223*, 489-508, 1991.

Marks, N. S., Sedimentation on new ocean crust: the Mid-Atlantic Ridge at 37° N, *Mar. Geol., 43*, 65-82, 1981.

Shaw, P. R., and D. K. Smith, Robust description of statistically heterogeneous seafloor topography through its slope distribution, *J. Geophys. Res., 95*, 8705-8722, 1990.

Tucholke, B. E. and P. R. Vogt, Western North Atlantic: sedimentary evolution and aspects of tectonic history, *Init. Repts. DSDP, 43*, 791-825, 1979.

Tucholke, B. E., and others, in preparation, 1993.

van Andel, T. H. and P. D. Komar, Ponded sediments of the Mid-Atlantic Ridge between 22° and 23° North Latitude, *Geol. Soc. Am. Bull., 80*, 1163 1190, 1969.

H. F. Webb and T. H. Jordan, Department of Earth, Atmospheric and Planetary Sciences, 54-918, Massachusetts Institute of Technology, 77 Massachusetts Avenue, Cambridge, MA 02139

FIGURE CAPTIONS

Fig. 1. Plan-view relief images (*top*) and vertical cross-sections (*bottom*) of two sedimented seafloors obtained by the diffusive-transport algorithm described in the text, showing the effect of different diffusivities: $\kappa = 0.02$ m²/yr (*left*), $\kappa = 0.8$ m²/yr (*right*). The models have the same age ($T = 25$ Ma), sedimentation rate ($F = 4$ m/My), sediment load ($L = 100$ m) and basement topography ($H = 250$ m, $\lambda_s = 22$ km, $\lambda_n = 5.4$ km, $\zeta_s = 35°$, $D = 2.2$). The lower diffusivity produces a morphology in which sediments drape hillsides, while the higher value allows a more rapid downslope transport, exposing the peaks and creating flat sediment ponds. The dimensions of the images are 30 km × 30 km; color changes at elevations of −200, 200, and 600 m. Cross-sections are taken along the dashed lines and plotted with a vertical exaggeration of 7.5 : 1. The sections show basement topography, the sediment-water interface, and two intermediate horizons corresponding to isochrons at 5 My ($L = 20$ m) and 10 My (50 m).

Fig. 2. Cumulative slope distribution functions $S(\theta, u)$ for $u = 300$ m, calculated from profiles across sedimented-seafloor models. *Top diagram* illustrates the effect of varying sediment load ($L = 25, 50, 75, 100$ m) for fixed abyssal-hill amplitude and diffusivity ($H = 200$ m, $\kappa = .10$ m²/yr). *Bottom diagram* shows the effect of varying diffusivity ($\kappa = .02, .10, .30, .80$ m²/yr) for fixed L (50 m) and H (150 m in upper curves, 325 m in lower curves). All calculations are based on $F = 4$ m/My.

Fig. 3. Map of the ARSRP corridor, showing bathymetry, Ewing 9208 track lines, and values of the model parameters estimated for the 19 areas analyzed in this report. Track lines used to obtain slope distributions are highlighted; L (in meters) is given by large number centered on each area, with H (in meters) and κ (in m²/yr) listed as small numbers above and below. Color changes correspond to water depths of 3200, 4000, and 4800 m. Region of deep bathymetry (light brown) trending WNW through the center of the corridor is a ridge-segment boundary that separates higher amplitude abyssal hills to the north ($\overline{H} = 255 \pm 12$ m) from lower amplitude hills to the south ($\overline{H}$

$= 214 \pm 5$ m). The sediment load L ranges from 11 to 55 m, primarily as a function of crustal age (see Figure 5); maximum values occur in the center of the corridor ($T \approx 10-15$ Ma). Significant differences in the apparent diffusivity are obtained from the data analysis ($\kappa = 0.04-0.26$ m²/yr), but no spatial pattern is evident. Averaged over all 19 areas, $\overline{\kappa} = 0.13 \pm .014$ m²/yr.

Fig. 4. *Top diagram* is a plot of $S(\theta, u)$ for the area centered at 26.0° N, 46.5° W; dots are the data obtained from 170 km of Hydrosweep center-beam soundings, and the curve is the cumulative slope distribution derived from the best-fitting model topography ($H = 220 \pm 7$ m, $L = 34 \pm 3$ m, $\kappa = .09 \pm .02$ m²/yr). Lower diagrams are L vs. H (*center*) and L vs. κ (*bottom*), showing the best estimates (crosses) and 95% confidence regions (contour lines).

Fig. 5. Estimates of sediment load L as a function crustal age for the 19 areas analyzed in this report. Line corresponds to a constant sedimentation rate of 3.4 m/My. Shaded region delimits the interval of CCD deepening discussed by Tucholke and Vogt [1979]. We speculate that the non-monotonic behavior observed in the ARSRP corridor is due to this change in the CCD.
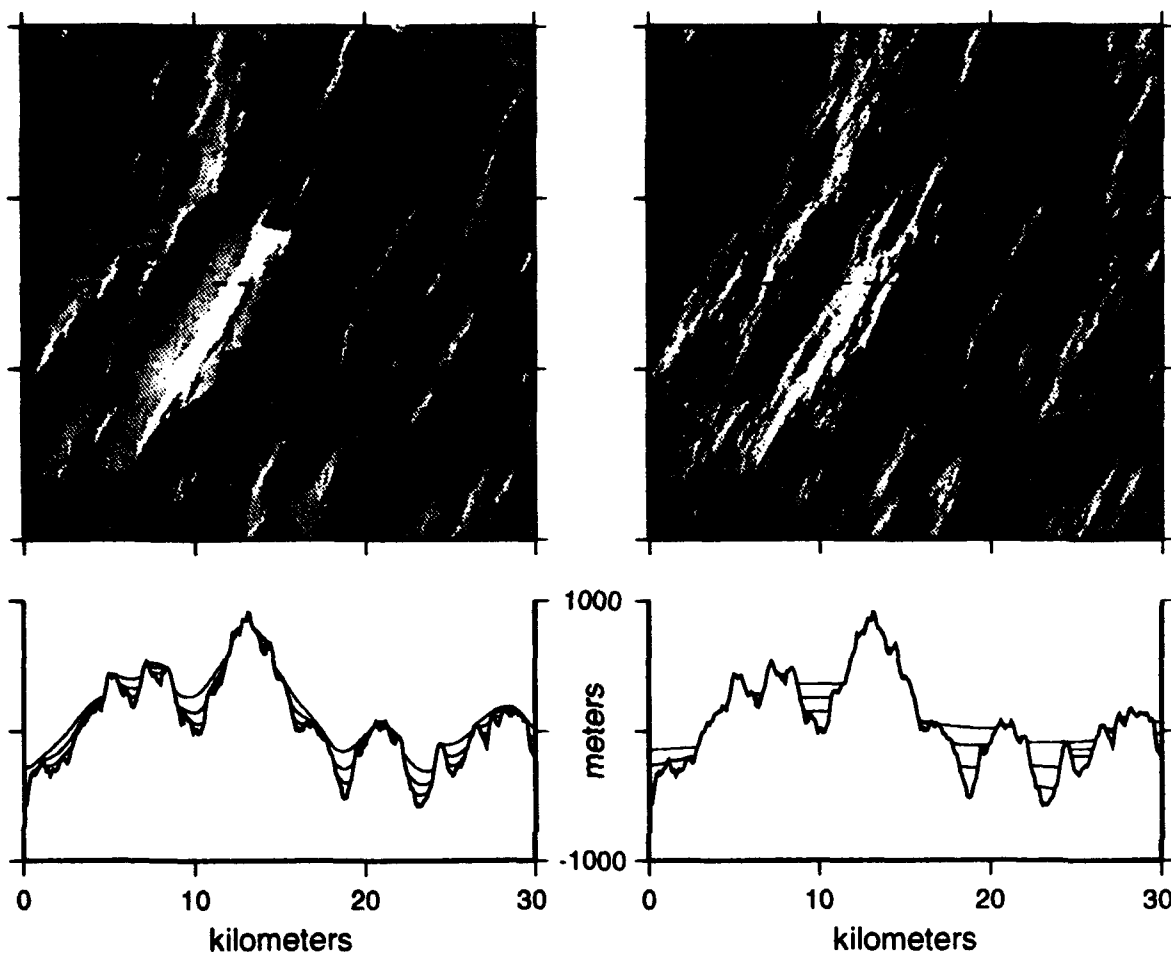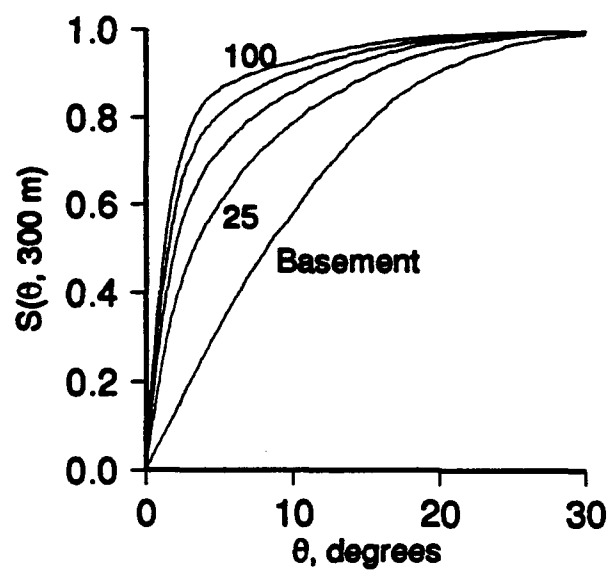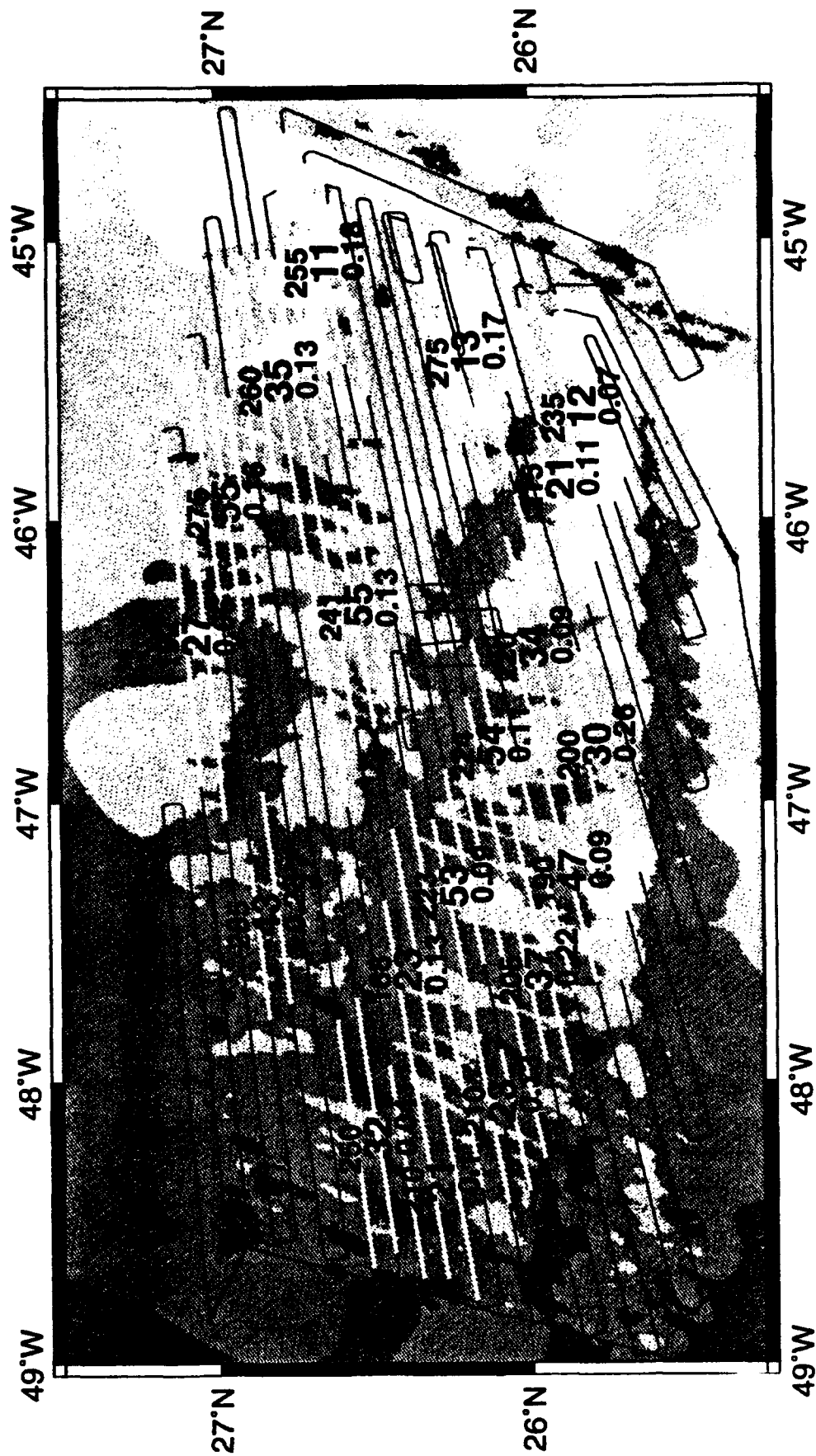
Webb and Jordan

Figure 1
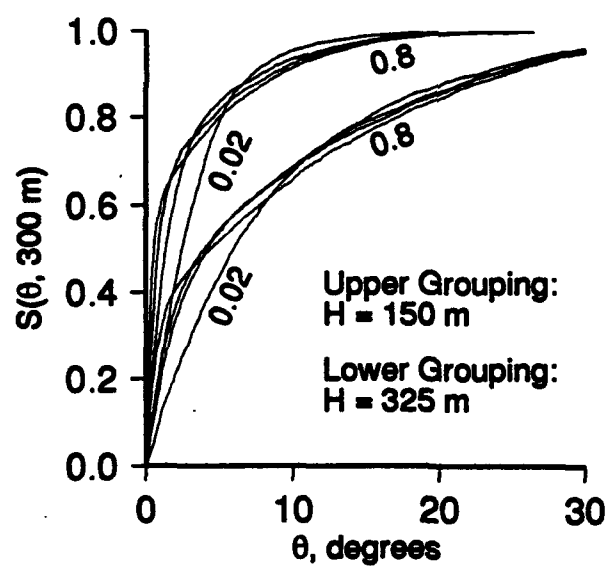
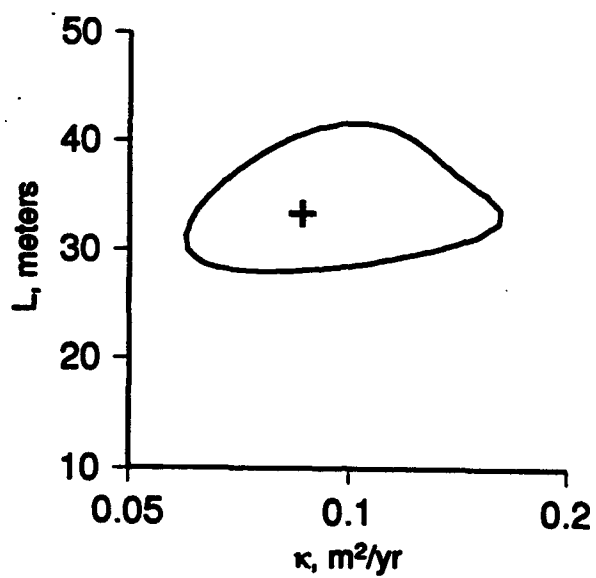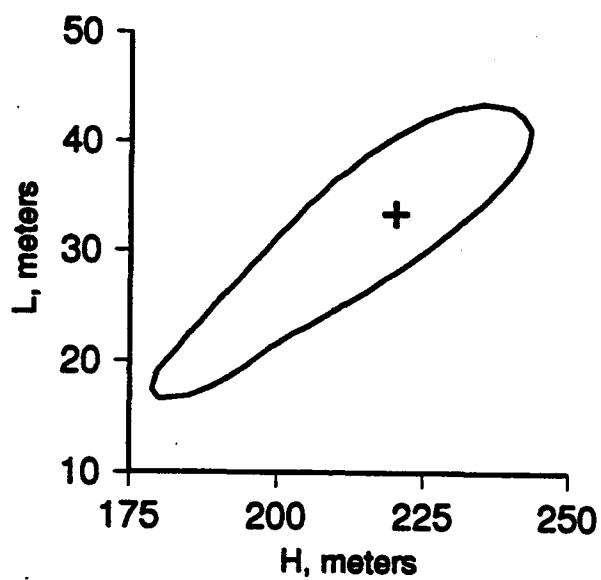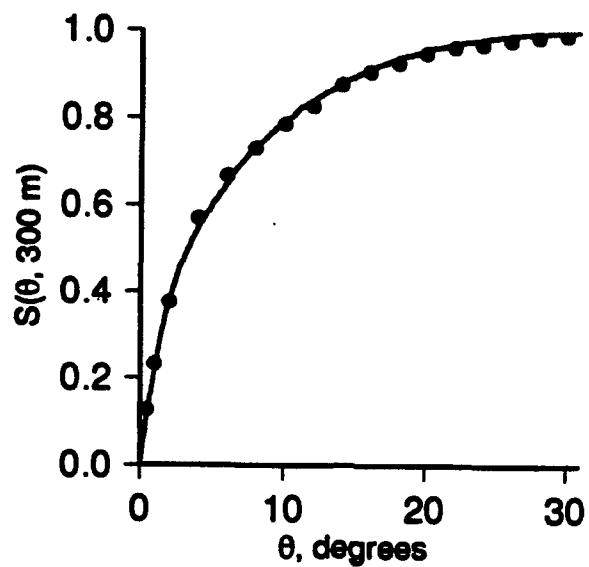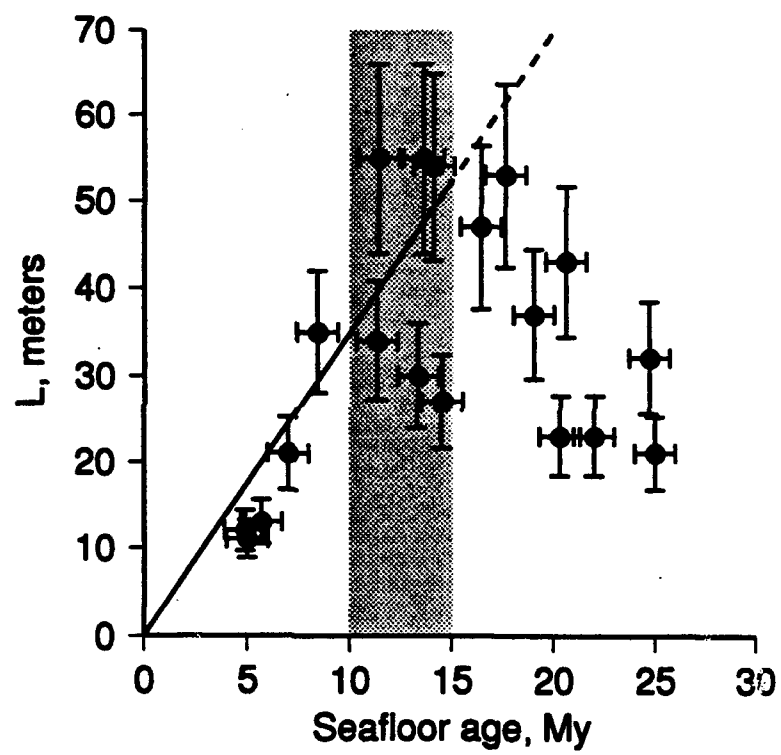Figure 2

Figure 3

Webb and Jordan

Figure 4

Figure 5

Modeling Sedimentation of a Rough Seafloor

Helen F. Webb

Abstract.   Sedimentation is the primary modifier of small-scale topography created by volcanic and tectonic processes in the vicinity of ridge crests. In particular, sediment accumulation tends to smooth small-scale topographic roughness. To study this process in pelagic environments, we model deep-sea sedimentation as a diffusion-like process characterized by two parameters, a sediment flux F and a diffusivity κ. We did not account for sediment compaction or the erosion of bedrock.

For low diffusivity values ($\kappa < 20,000$ m²/My) our model causes sediments to drape over the basement topography. For high values ($\kappa > 100,000$ m²/My) sediments are swept downslope and accumulate in topographic lows to form sediment ponds.

We found that the burial of a hard-rock surface characterized by a Gaussian height distribution generates a sediment-water interface whose statistics have a distinctly non-Gaussian character. As average sediment depth increases, the RMS height and fractal dimension decrease, and the characteristic length scales of the topography increase. Increasing the diffusivity constant of the sediment distribution process also decreases the RMS height and increases the characteristic length scale of the topography.

INTRODUCTION

The floor of the world's oceans is subject to a constant rain of sedimentation from wind-carried continental dust, the weathering of oceanic islands, and biological sources. Although sedimentation rates in pelagic environments are low (from less than 1 m/My to over 50 m/My), over time sedimentation smooths seafloor topography. Abyssal plains, which extend oceanward from passive continental margins, are products of tens of millions of years of sedimentation.

The processes of sediment transport and deposition in the abyssal environment are not well understood. The initial location of sediment deposition must be a function of sediment type and the interaction of seabottom currents with seafloor constructs. Over time, steady bottom currents [e.g. Dickson and Kidd, 1987], burrowing animals, and

1

localized storms (with water velocities of up to 0.73 m/sec [Richardson et al., 1981]) cause sediments to be redistributed. Changes in bottom water movement due to global climate changes and continental reconfigurations also can disturb sediments, leaving gaps in deepsea drill cores [e.g. Johnson, 1972; Thiede et al, 1981]. These processes cause the pattern of sedimentation to vary between different locations. In some regions, sediments form a terrain-mimicking blanket, preserving the shape of abyssal hills created at the ridge crest (Figure 1). In other regions, sedimentation fills up valleys while leaving the tops of abyssal hills bare, quickly evening the terrain (Figure 2). Most areas of the seafloor fall between these extremes, with thicker layers of sediment covering bedrock lows than cover highs. Photographs of the seafloor show that manganese nodules can remain uncovered, indicating that even small topographic highs can be kept clear of sediments [e.g. Heezen and Hollister, 1971], while sediment cores show that cracks between pillow basalts become filled soon after creation [e.g. Reynolds and Linsley, 1985].

If, over time, the lateral flux f of erodible sediment is proportional to the local gradient of height via a diffusivity constant κ, sediment transport can be modeled as a diffusive process in which erodible material is removed from topographic highs to fill lows. Cullings [1960] pioneered this approach to modelling geomorphological structures. Newman and Turcotte [1990] point out that diffusion will produce topography that is not scale invariant, but instead preferentially eliminates short-wavelength topography. Therefore, they conclude that diffusive models can not explain most of the topography found in nature. Published seafloor power spectra for continental rise regimes tend to have in increase, instead of a decrease, in power at high wavenumber [Fox and Hayes, 1985], so it is unlikely that diffusion would adequately explain their structure; however, the topography of the abyssal hill regime is quite different. On abyssal hills, the main effect of sediment movement is probably the filling of small cracks, which would reduce power at high wavenumber. Few, if any, events take place off axis over time which would increase power at high wavenumber.

2

Workers have successfully used diffusion to explain the evolution of scarplike landforms [Hanks et al., 1984] and the stratigraphy found in foreland basins [Flemings and Jordan, 1989] and in shallow marine settings [Kaufman et al., 1991]. The success of these models is due, in part, to the incorporation of geological processes such as isostatic compensation [Flemings and Jordan, 1989] and the decrease of wave energy with depth [Kaufman et al., 1991]. In our model of sediment transport, we have incorporated the geometry of the seafloor prior to sedimentation, although other physical factors contributing to sediment distribution, such as seabottom currents, have been ignored.

The total height $h(\mathbf{x},t)$ of the seafloor is given by

$$h(\mathbf{x},t) = s(\mathbf{x},t) + b(\mathbf{x}) \tag{1}$$

where $s(\mathbf{x},t)$ is the thickness of the erodible layer of sediment which covers a durable basement of height $b(\mathbf{x})$. We model sediment thickness over time as equal to the gradient of f plus the downward sediment flux F:

$$\frac{\partial s}{\partial t} = \kappa \frac{\partial^2(s+b)}{\partial x^2} + F(\mathbf{x},t) = \kappa \frac{\partial^2 h}{\partial x^2} + F(\mathbf{x},t) \tag{2}$$

subject to the constraint that $s(\mathbf{x},t) \geq 0$. We compute the sediment thickness $s(\mathbf{x},t)$ by solving (2) numerically.

SEDIMENTATION ALGORITHM

Numerical methods for solving parabolic equations are based on the approximation

$$\frac{\partial s}{\partial t} \equiv \frac{\partial h}{\partial t} \cong \frac{h(\mathbf{x},t+\Delta t) - h(\mathbf{x},t)}{\Delta t} \tag{3}$$

Values of $s(\mathbf{x},t)$ are calculated by iterating forward from $s(\mathbf{x},0) = 0$. In implicit methods such as the Crank-Nicolson method [Crank and Nicolson, 1947] and the alternating-direction-implicit scheme [Peaceman and Rachford, 1955], values of $h(\mathbf{x},t + \Delta t)$ are not just functions of $h(\mathbf{x},t)$ but also involve other values of h at the same time step. These

3

methods can be adapted to run efficiently on serial computers. However, a new class of computers, including the Connection Machine manufactured by Thinking Machines Corporation, is built to perform thousands of identical, simple operations simultaneously on grids of data. Speed is increased when data is passed only between neighboring grid points. To solve (2) using such a machine, we use an explicit method so that values of $h(x,t + \Delta t)$ are only dependent on $h(x,t)$, allowing all values of h for each time step to be calculated simultaneously. Our algorithm is a variation of the method of Schmidt [1924], who used the approximation

$$\frac{\partial^2 h}{\partial x^2} \cong \left[\frac{(h(x+\Delta x,t) - h(x,t)) + (h(x-\Delta x,t) - h(x,t))}{(\Delta x)^2} \right] \qquad (4)$$

We apply (4) and (3) to (2), obtaining, for the two-dimensional case,

$$s(x,t+\Delta t) \cong s(x,t) + \frac{\kappa \Delta t}{(\Delta x)^2}[(h(x+\Delta x,t) - h(x,t)) + (h(x-\Delta x,t) - h(x,t))] + \Delta t F(x,t) \qquad (5)$$

subject to the inequality $s(x,t+\Delta t) \geq 0$.

The speed of computation is proportional to the magnitude of $\kappa \Delta t/(\Delta x)^2$; however, for $\kappa \Delta t/(\Delta x)^2 > 1/3$ for the two-dimensional case, and $\kappa \Delta t/(\Delta x)^2 > 1/5$ for the three-dimensional case, the value of $h(x,t+\Delta t)$ is more dependent on h at neighboring points than at x. This causes h to oscillate. For $1/3 < \kappa \Delta t/(\Delta x)^2 \leq 1/2$ for the two-dimensional case, and $1/5 < \kappa \Delta t/(\Delta x)^2 \leq 1/4$ for the three-dimensional case, the oscillations damp out with increasing t. To prevent having minimum time requirements, and to maintain conformity between the two- and three-dimensional models of sediment transport, we use $\kappa \Delta t/(\Delta x)^2 = 0.2$ for both algorithms. Therefore, the timestep Δt needed to simulate a given diffusivity κ is calculated by

$$\Delta t = 0.2(\Delta x)^2/\kappa. \qquad (6)$$

4

For a given number of years T, $N = T/\Delta t$ iterations are needed.

The following steps comprise the two-dimensional algorithm. This algorithm is easily extended to three dimensions. A graphical example of the diffusion methodology is provided in Figure 3:

Initialization: Basement topography $h(x)$ is discretized on a straight line with horizontal spacing Δx and total horizontal length $X = K\Delta x$.

Execution The following steps are then performed N times:

(a) *Sediment Accumulation*: Parcels of dimensions $(\Delta x, F\Delta t)$ are accumulated at each horizontal position x_k.

(b) *Sediment Redistribution*: First, height differences $\Delta h_k^+ = h(x_k) - h(x_{k+1})$ and $\Delta h_k^- = h(x_k) - h(x_{k-1})$ are calculated at each point. To conserve sediment, $\Delta h_0^- \equiv 0$ and $\Delta h_K^+ \equiv 0$. The sediment excess

$$e_k = 0.2(\max(\Delta h_k^+, 0) + \max(\Delta h_k^-, 0)) \tag{7}$$

is then calculated. If $\Delta h_k^+ > 0$ and $s(x_k) < e_k$ then $\Delta h_k^+ = \Delta h_k^+(s(x_k)/e_k)$ and Δh_{k+1}^- is set equal to $-1.0(\Delta h_k^+)$. Likewise, if $\Delta h_k^- > 0$ and $s(x_k) < e_k$ then $\Delta h_k^- = \Delta h_k^-(s(x_k)/e_k)$ and Δh_{k-1}^+ is set equal to $-1.0(\Delta h_k^-)$. Finally, the amount of sediment change for each point, $\Delta s_k = -0.2(\Delta h_k^+ + \Delta h_k^-)$, is calculated and added to $s(x_k)$.

MODEL SEAFLOOR BATHYMETRY

We use Goff-Jordan [1988] model seafloor bathymetry to test our sedimentation methodology. Model bathymetry was used instead of real bathymetric data both because we lacked sediment-free data with uniform point spacings in the 25 - 100 m range, and so that we could more easily compare the statistical parameters of the resulting sedimented profiles and surfaces to the original topography. Goff and Jordan [1988] model the seafloor as a stationary, zero-mean, Gaussian random field completely specified by its two-point covariance function. This function has five parameters which correspond to RMS height H, characteristic along- and across-flowline corner wavenumbers k_n and k_s, local strike ζ, and fractal dimension D.

EXPERIMENTAL DESIGN

We modelled the sedimentation of both a three-dimension grid of simulated bathymetry and five two-dimension profiles of simulated bathymetry. Although three-dimensional modelling probably produces the more realistic results, large grids are required to cover multiple abyssal hills using even a course point spacing. Reducing Δx by a factor of α increases both the grid size and the number of iterations N by factors of α^2, leading to a total computation time increase of α^4, whereas a similar decrease in point spacing along a two-dimensional profile only leads to a total computation time increase of α^3. Therefore, two-dimensional profiles were used to test the sedimentation model on more closely spaced simulated bathymetry.

The three-dimensional grid of simulated bathymetry (Figure 4) was created by molding a surface generated using the Goff-Jordan methodology with DBDB5 data from the vicinity of 22° N, 47° W (near the Mid Atlantic Ridge, south of the Kane Fracture Zone) [Goff and Jordan, 1990]. This model seafloor bathymetry is already available to the

6

acoustics community via the Office of Naval Research's Special Research Project on Acoustic Reverberation. It consists of 1000 x 1000 points of bathymetry with a grid spacing Δx of 100 m. This spacing was chosen so that several abyssal hill wavelengths would be included in all directions. The region was sedimented for 20 My of model time using diffusivities of 1600 m^2/My, 16,000 m^2/My, 160,000 m^2/My, and 1,600,000 m^2/My. Flux was kept constant at 10 m/Myr, and sediment-water interface surfaces were recorded every 5 My of model time. Several of the surfaces generated are shown in Figure 5, and profiles taken across the middle of these regions are shown in Figure 6.

To test our model on a more closely spaced data set, we modeled the sedimentation of five 125 km-long profiles which had relatively small horizontal point spacings Δx of 25 m. The profiles were each sedimented for 10 My of model time using diffusivities of 1600 m^2/My, 16,000 m^2/My, 160,000 m^2/My, and 1,600,000 m^2/My. Flux was kept constant at 10 m/Myr, and sediment-water interface profiles were recorded every 2.5 My. These profiles are shown in Figure 7.

The parameters governing the diffusive process, κ, total time T, and flux F, can be combined to form a non-dimensional measure of diffusivity

$$K = \frac{\kappa}{TF^2}$$

(8)

Thus, for a given average sediment thickness (TF), increasing F and κ by the same factor produces equivalent topography.

RESULTS AND ANALYSIS

We found that our model was able to produce sediment distributions that resemble those found in nature. Using a diffusivity κ of 1.6×10^3 m^2/My (Figure 5(a,b); Figure 6(a); Figure 7(a)), we produced topography that resembles the "pelagic drape"

character of Figure 1. Higher values of κ lead to increased mobility of sediments, with sediments ponding between, and eventually covering, abyssal hills (Figure 5(c,d); Figure 6(d); Figure 7(d)). This topography resembles that of Figure 2.

When κ and t are small, sediments to not spread far from where they are originally located, so the variation of sediment thickness has a low amplitude and a small characteristic horizontal scale (Figure 8(a)). As T increases, this characteristic scale increases (Figure 8(b)), as sediments are gradually able to fill topographic lows. Increasing κ (Figure 8(c)) causes both the amplitude and characteristic scale to increase, owing to the formation of large, deep sediment ponds. When the sediment load is large enough (Figure 8(d)), the variations in $s(x,t)$ mimic those of the basement topography $b(x)$ (Figure 4).

The effects of this diffusivity-governed spread of sediment can be seen in histograms of sediment thickness and seafloor height. In a regime of high sediment diffusivity, the seafloor height distribution quickly loses its Gaussian character (Figure 9). For large sediment loads ($T = 20$ My), the height distribution contains many peaks, corresponding to the damming of sediments behind abyssal hills. Low-lying areas are quickly filled, causing an increase in the minimum heights with T; however, since peaks do not accumulate sediment, the upper tails of all of the distributions are similar. Histograms showing the height distribution of sedimented seafloor for $T = 20$ My and a variety of diffusivities show the development of this peakiness (Figure 10).

Sediment thickness histograms (Figures 11 and 12) show that, where sediment exists, it exhibits a Gaussian-like distribution of depths. However, as diffusivity increases, much of the seafloor is stripped of its blanket of sediment.

We used the results of sedimenting long, densely spaced (25 m) two-dimensional profiles shown in Figure 7 to determine the effects of sedimentation on seafloor power spectra and the Goff-Jordan statistical parameters. The power spectra of sedimented profiles resemble the power spectrum of the basement topography at low wavenumbers,

8

but feature roll-offs at intermediate wavenumbers. At high wave numbers, the slope of the power spectra of the sedimented profiles is usually the same as the slope of the basement's power spectrum.

After 2.5 My of sedimentation, the greatest deviations from the spectrum of the Goff-Jordan basement topography occur for low values of κ, where the sediment distribution is in the form of pelagic drape (Figure 13). The smoothing this entails causes low power at high wavenumbers. At high values of κ, uncovered peaks contribute energy at high wavenumbers. After 10 My of sedimentation, all diffusivities yield the same power at high wavenumber; however, increasing κ reduces power at intermediate wavenumbers (Figure 14).

Plots of power spectra of profiles with similar diffusivities show that, as the amount of sediment increases, power at intermediate and high wavenumbers decreases (Figures 15 to 18). The pattern is similar for all diffusivities, with the primary difference being a downward progression of the wavenumber, with increasing diffusivity, at which the power spectra of the sediment profiles separate from the power spectrum of the basement topography.

The power spectra roll-offs seen are common to models of mass distribution that entail diffusivity [Newman and Turcotte, 1990]. Just as there is a low corner wavenumber in the power spectrum of the simulated basement topography that corresponds to a characteristic upper topographic wavelength, the bends in the power spectra at intermediate wavenumber may correspond to a characteristic wavelength of topography that has been buried or filled in by sediment.

Although the power spectra of the sedimented profiles clearly do not follow the Goff-Jordan model, fitting ideal covariance functions to the covariance functions of the data to obtain values for RMS H, characteristic wavenumber k_n, and fractal dimension D allows us to quantify the effects of sedimentation on the larger scale statistics of the basement topography. These parameters are listed in Table 1. The immediate decrease in

fractal dimension shows that much of the small-scale characteristic roughness of the topography is filled in by sediment soon after abyssal hill formation; the increase in D with high diffusivity is caused by the reemergence of peaks. The decrease in H with sediment thickness (and, therefore, time) is caused by valleys filling with sediment, reducing abyssal hill height. Higher diffusivities probably cause sediment particles to be more rapidly transported from peaks to values, lowering H further. The decrease in characteristic wavenumber k_n with sediment thickness and diffusivity corresponds to an increase in the characteristic length scale of the topography, which is primarily caused by the submergence of lower-lying abyssal hills.

CONCLUSIONS

We have developed a model for the sedimentation of abyssal hills. Sediment transport is modeled as a diffusive process in which mass moves relative to local gradients. Profiles and surfaces created using our methodology vary with the diffusivity constant, but have the same character as sections of the actual seafloor (Figures 1 and 2).

Our model changes the depth distribution, power spectra, and statistical parameters of the seafloor. In particular, characteristic abyssal hill heights are decreased while the distances between peaks are increased. A corner in power spectra at intermediate wavenumber may indicate an lower limit for the wavelength of topographic features.

Our model is undoubtedly an oversimplification of the processes that govern sedimentation. For instance, we assume that there is no preferential direction for the lateral movement of sediment particles; however, in nature, unidirectional seafloor currents probably do affect sediment placement. We also assume that diffusivity is constant throughout a region; however, sedimentation processes may differ between peaks and valleys. To investigate how the sedimentation of an actual seafloor differs from our model, we plan to apply our methodology to grids of estimated basement depths and compare the

10

resulting sedimented surface to actual bathymetric data. Detailed data to be used for this comparison is currently being collected as part of a survey of the western flank of the Mid Atlantic Ridge south of the Kane Fracture Zone. This data set will also be used to develop methods for inverting single-channel bathymetry to determine the sediment diffusivity parameter, which may be a useful descriptor of the style of sedimentation of the seafloor.

REFERENCES

Crank, J. and P. Nicolson, *Proc. Camb. Phil. Soc.*, *43*, 50-67, 1947.

Culling, W. E. H., Analytical theory of erosion, *J. Geol.*, *68*, 336-344, 1960.

Dickson, R. R. and R. B. Kidd, Deep circulation in the southern Rockall Trough - the oceanographic setting of Site 610, *Init. Repts. DSDP*, *94*, 1061-1073, 1987.

Flemings, P. B. and T. E. Jordan, A synthetic stratigraphic model of foreland basin development, *J. Geophys. Res.*, *94*, 3851-3866, 1989.

Fox, C. G. and D. E. Hayes, Quantitative methods for analyzing the roughness of the seafloor, *Rev. Geophys.*, *23*, 1-48, 1985.

Goff, J. A. and T. H. Jordan, Stochastic Modeling of Seafloor Morphology: Inversion of Sea Beam data for second-order statistics, *J. Geophys. Res.*, *93*, 13589-13608, 1988.

Goff, J. A. and T. H. Jordan, Pacific and Atlantic models of small-scale seafloor topography, *Office of Naval Research S. R. P. on Acoustic Reverberation*, Technical Report No. 1, 1990.

Hanks, T. C., R. C. Bucknam, K. R. Lajoie, and R. E. Wallace, Modification of wave-cut and faulting-controlled landforms, *J. Geophys. Res.*, *89*, 5771-5790, 1984.

Heezen, B. C. and C. D. Hollister, *The Face of the Deep*, Oxford University Press, New York, 1971.

Johnson, David A., Ocean-floor erosion in the equatorial Pacific, *Geol. Soc. America Bull.*, *83*, 3121-3144, 1972.

Kaufman, P., J. P. Grotzinger and D. S. McCormick, Depth-dependent diffusion algorithm for simulation of sedimentation in shallow marine depositional systems, *Kansas Geological Survey Bulletin 223*, 489-508, 1991.

Newman, W. I. and D. L. Turcotte, Cascade model for fluvial geomorphology, *Geophys. J. Int.*, 100, 433-439, 1990.

Peaceman, D. W. and H. H. Rachford, The numerical solution of parabolic and elliptic differential equations, *J. Soc. Ind. Appl. Math.*, *3*, 28-41, 1955.

Rabinowitz, P. D., J. R. Heirtzler, T. D. Aitken, and G. M. Purdy, Underway geophysical measurements: *Glomar Challenger* Legs 45 and 46, *Init. Repts. DSDP*, *45*, 55-118, 1979.

Reynolds, L. A. and B. K. Linsley, Cross-lamination and graded interpillow limestones, Site 562, *Init. Repts. DSDP*, *82*, 543-545, 1985.

Richardson, M. J., M. Wimbush and L. Mayer, Exceptionally strong near-bottom flows on the continental rise of Nova Scotia, *Science*, *213*, 887-888, 1981.

Schmidt, E., *Foppls Festschrift*, Springer, 1924.

Thiede, J., J.-E. Strand and T. Agdestein, The distribution of major pelagic sediment components in the Mesozoic and Cenozoic North Atlantic Ocean, *SEPM Special Publication No. 32*, 67-90, 1981.

FIGURE CAPTIONS

Figure 1: These seismic reflection profiles from the North Atlantic southwest of the Kane Fracture zone show sediments draping topography. Estimated diffusivities for the top two profiles are $< 10,000 \ m^2/My$. The bottom profile has an estimated diffusivity of $50,000 \ m^2/My$. Verticle exaggeration is approximately 10:1.

Figure 2: The sediments shown in this seismic profile have formed flat sediment ponds. The estimated diffusivity for this region is $1,000,000 \ m^2/My$. This profile images crust on the eastern side of the Mid Atlantic Ridge south of the Kane Fracture Zone. Verticle exaggeration is approximately 10:1.

Figure 3: A sample basement topography is subjected to two iterations of the sediment distribution algorithm. The quantity $F\Delta x$ here is equal to 0.5 m, and $K = 3$. First, basement topography is discretized, yielding $b(0) = 1.0$, $b(1) = 3.0$, $b(2) = 2.0$, and $b(3) = 2.0$. At $t = 0$, $h(x) = b(x)$ (box (a)).

After adding $F\Delta x$ to each horizontal position x_k, $h(0) = 1.5$, $h(1) = 3.5$, $h(2) = 2.5$, and $h(3) = 2.5$ (box (b)).

Following the procedure described in the text, height differences are then calculated, giving $\Delta h_0^- = 0.0$, $\Delta h_0^+ = -2.0$, $\Delta h_1^- = 2.0$, $\Delta h_1^+ = 1.0$, $\Delta h_2^- = -1.0$, $\Delta h_2^+ = 0.0$, $\Delta h_3^- = 0.0$, and $\Delta h_3^+ = 0.0$. From equation (8), we then calculate $e_0 = 0.2(0.0) = 0.0$, $e_1 = 0.2(3.0) = 0.6$, $e_2 = 0.2(0.0) = 0.0$, and $e_3 = 0.2(0.0) = 0.0$. Since $\Delta h_1^+ > 0$ and $s(x_1) < e_1$ a new $\Delta h_1^+ = \Delta h_1^+(s(x_1)/e_1)$ is calculated, giving $\Delta h_1^+ = 1.0(0.5/0.6) = 0.833$. Δh_2^- is then reset to -0.833. Also, since $\Delta h_1^- > 0$ and $s(x_1) < e_1$ a new $\Delta h_1^- = \Delta h_1^- (s(x_1)/e_1)$ is calculated, giving $\Delta h_1^- = 2.0(0.5/0.6) = 1.667$. Δh_0^+ is then reset to -1.667. Using $\Delta s_k = -0.2(\Delta h_k^+ + \Delta h_k^-)$, we then compute $\Delta s_0 = 0.333$, $\Delta s_1 = -0.5$, $\Delta s_0 = 0.167$, and $\Delta s_0 = 0.0$. Adding these changes in sediment amount to $s(x_k)$ yields $h(0) = 1.833$, $h(1) = 3.0$, $h(2) = 2.667$, and $h(3) = 2.5$ (box (c)).

14

This completes one iteration of the algorithm. Repeating the steps above, adding $F\Delta x$ to each horizontal position produces the configuration in box (d). After redistribution, $h(0) = 2.567$, $h(1) = 3.2$, $h(2) = 3.2$, and $h(3) = 3.033$ (box (e)).

Figure 4: Grey-shaded color relief image of the basement topography $b(x)$ employed in our sediment accumulation calculations. This model was created by molding a surface generated using the Goff-Jordan [1988] methodology with DBDB5 data from the vicinity of 22° N, 47° W (near the Mid-Atlantic Ridge, south of the Kane Fracture Zone). Grid spacing is 100 m. Goff-Jordan parameters used to create the interpolating surface are $H = 225$ m, $D = 2.2$, $k_n = 0.55$ km^{-1} (corresponding to a characteristic abyssal hill spacing of 5.9 km) and $k_s = 0.15$ km^{-1} (corresponding to a characteristic abyssal hill length of 22 km).

Figure 5: Maps of total topography of the seafloor $h(x,t)$ after sedimentation, showing four cases:

(a)	$t = 5$ My,	$\kappa = 1.6 \times 10^3$ m^2/My
(b)	$t = 20$ My,	$\kappa = 1.6 \times 10^3$ m^2/My
(c)	$t = 5$ My,	$\kappa = 1.6 \times 10^6$ m^2/My
(d)	$t = 20$ My,	$\kappa = 1.6 \times 10^6$ m^2/My

In all four cases, the sediment flux $F(x,t)$ was held constant at 10 m/My.

The low-diffusivity cases (a) and (b) result in "pelagic drape", with an essentially uniform thickness of sediments overlying the basement topography; $h(x,t)$ therefore resembles a slightly smoothed version of $b(x)$.

For the high-diffusivity cases (c) and (d), the increased mobility of the sediments forms sediment ponds between abyssal hills; after 20 My of sediment accumulation (d), only the highest peaks emerge from the sediment.

Figure 6: Cross-sections through three-dimensional sedimented seafloor models, showing the variations in isopachs due to variations in the diffusivity κ. The black lines represent the basement topography corresponding to an east-west profile through the center of Figure 4. The colored lines are isopachs with spacings of 5 My. Diffusivities used to compute the profiles are:

(a) $\kappa = 1.6 \times 10^3 \ m^2/My$

(b) $\kappa = 1.6 \times 10^4 \ m^2/My$

(c) $\kappa = 1.6 \times 10^5 \ m^2/My$

(d) $\kappa = 1.6 \times 10^6 \ m^2/My$

Vertical exaggeration is 10:1.

Figure 7: Portions of model basement (black) and computed sediment isopachs (red) from one of the densely spaced (25 m) two-dimensional profiles used for determining the effects of sedimentation on seafloor power spectra and Goff-Jordan parameters. The basement profiles have Goff-Jordan parameters $H = 100$ m, $D = 1.4$, and $k_n = 0.4 \ km^{-1}$ (corresponding to a characteristic abyssal hill spacing of 7.4 km). Isopach spacing is 2.5 My. Diffusivities used to compute sediment profiles are:

(a) $\kappa = 1.6 \times 10^3 \ m^2/My$

(b) $\kappa = 1.6 \times 10^4 \ m^2/My$

(c) $\kappa = 1.6 \times 10^5 \ m^2/My$

(d) $\kappa = 1.6 \times 10^6 \ m^2/My$

16

Vertical exaggeration is 10:1. These diagrams are scaled so that abyssal hill heights and sediment layer thicknesses are approximately the same as in Figure 4.

Figure 8: Maps of sediment thickness $s(x,t)$, corresponding to the four cases (a)-(d) in Figure 5. For all of these plots, the salmon-red division of the color scale occurs at the average sediment thickness, which is 50 m for $t = 5$ My (a, c) and 200 m for $t = 20$ My (b, d).

When κ and t are small (case a), the variation of sediment thickness has a low amplitude and a small characteristic horizontal scale. As t increases, this characteristic scale increases (case b). Increasing κ (case c) causes both the amplitude and characteristic scale to increase, owing to the formation of large, deep sediment ponds. When the sediment load is large enough, the variations in $s(x,t)$ mimic those of the basement topography $b(x)$.

Figure 9: Histograms showing the height distribution of the basement topography (black line) and sedimented seafloor for $t = 5$ My (red), 10 My (blue), 15 My (green), and 20 My (purple), computed for $\kappa = 1.6 \times 10^6$ m^2/My (high diffusivity). For large sediment loads ($t = 20$ My), the height distribution has many sharp peaks. Low-lying areas are quickly filled, causing an increase in the minimum heights with t; however, since peaks do not accumulate sediment, the upper tails of all of the distributions are similar.

Figure 10: Histograms showing the height distribution of sedimented seafloor for $t = 20$ My and $\kappa = 1.6 \times 10^3$ m^2/My (red), 1.6×10^4 m^2/My (blue), 1.6×10^5 m^2/My (green), and 1.6×10^6 m^2/My (purple). Note the development of the peaks discussed in Figure 9.

Figure 11: Histograms showing the distribution of sediment thicknesses for $t = 5$ My (red), 10 My (blue), 15 My (green), and 20 My (purple), computed for $\kappa = 1.6 \times 10^6$

m^2/My (high diffusivity). The percentage of seafloor covered by less than one meter of sediment is 39%, 25%, 17%, and 11%, respectively.

Figure 12: Histograms showing the distribution of sediment thicknesses for $t = 20$ My and $\kappa = 1.6 \times 10^3$ m^2/My (red), 1.6×10^4 m^2/My (blue), 1.6×10^5 m^2/My (green), and 1.6×10^6 m^2/My (purple). The percentage of seafloor covered by less than one meter of sediment is 0%, 0.0003%, 3.5%, and 12%, respectively.

Figure 13: The power spectra of the 2.5 My layer subject to diffusivities of 1.6×10^3 m^2/My, 1.6×10^4 m^2/My, 1.6×10^5 m^2/My, and 1.6×10^6 m^2/My.

Figure 14: The power spectra of the 10 My layer subject to diffusivities of 1.6×10^3 m^2/My, 1.6×10^4 m^2/My, 1.6×10^5 m^2/My, and 1.6×10^6 m^2/My.

Figure 15: The power spectra of the basement and layers recorded after 2.5, 5, 7.5, and 10 My of sedimentation subject to a diffusivity of 1.6×10^3 m^2/My.

Figure 16: The power spectra of the basement and layers recorded after 2.5, 5, 7.5, and 10 My of sedimentation subject to a diffusivity of 1.6×10^4 m^2/My.

Figure 17: The power spectra of the basement and layers recorded after 2.5, 5, 7.5, and 10 My of sedimentation subject to a diffusivity of 1.6×10^5 m^2/My.

Figure 18: The power spectra of the basement and layers recorded after 2.5, 5, 7.5, and 10 My of sedimentation subject to a diffusivity of 1.6×10^6 m^2/My.

Table 1

κ (m²/My)	T (My)	H^2 (m²)	k_η (cycles/km)	Fractal Dimension
0	0	9538	0.45	1.4
1600	2.5	9326	0.55	1.2
1600	5.0	9212	0.6	1.1
1600	7.5	9124	0.6	1.05
1600	10.0	9050	0.6	1.05
16,000	2.5	8923	0.6	1.05
16,000	5.0	8506	0.55	<1.05
16,000	7.5	8210	0.55	<1.05
16,000	10.0	7976	0.5	<1.05
160,000	2.5	8389	0.55	1.05
160,000	5.0	7323	0.45	<1.05
160,000	7.5	6531	0.4	<1.05
160,000	10.0	5947	0.35	<1.05
1,600,000	2.5	8053	0.5	1.05
1,600,000	5.0	6458	0.35	1.1
1,600,000	7.5	5093	0.3	1.1
1,600,000	10.0	4054	0.25	1.1

Figure I

Seconds

7   8

02:00

19 JAN.

00:00

22:00

20:00

7   8

08:00

06:00

04:00

7   8

14:00

12:00

10:00
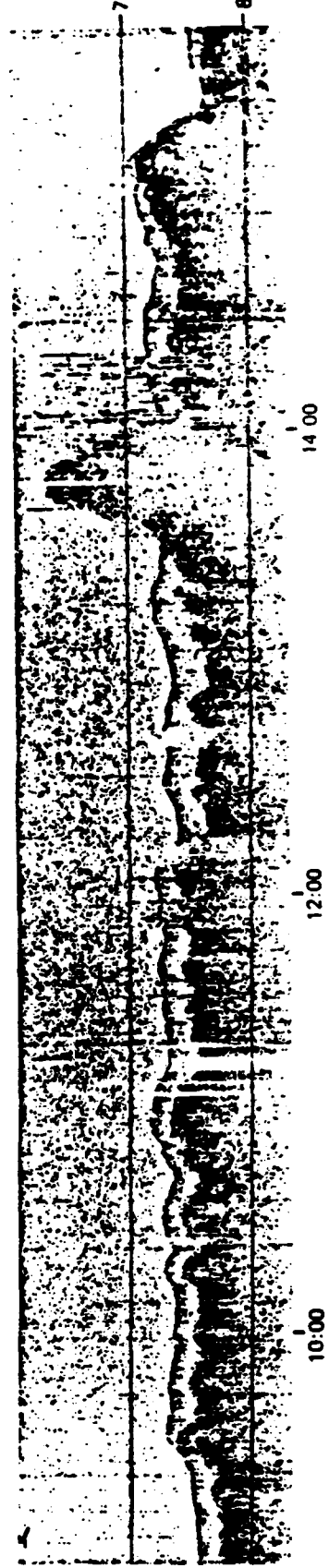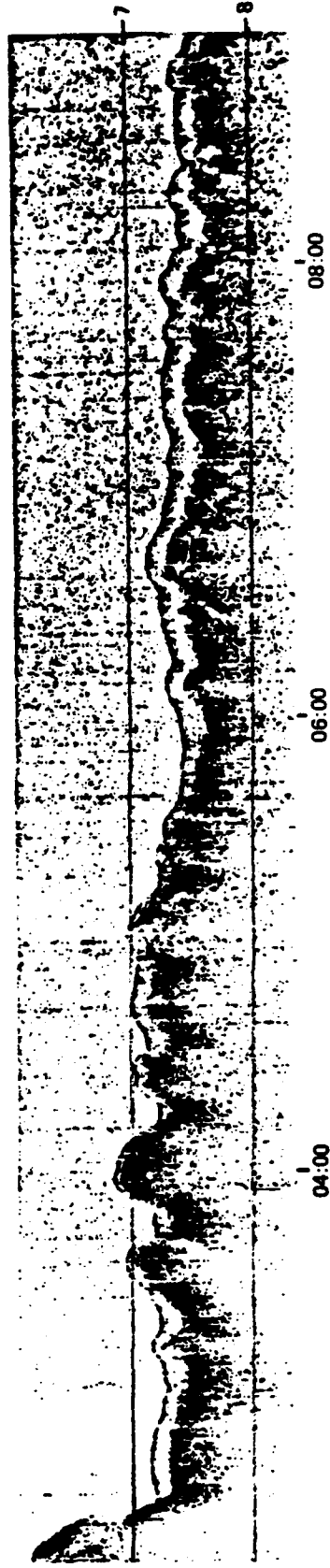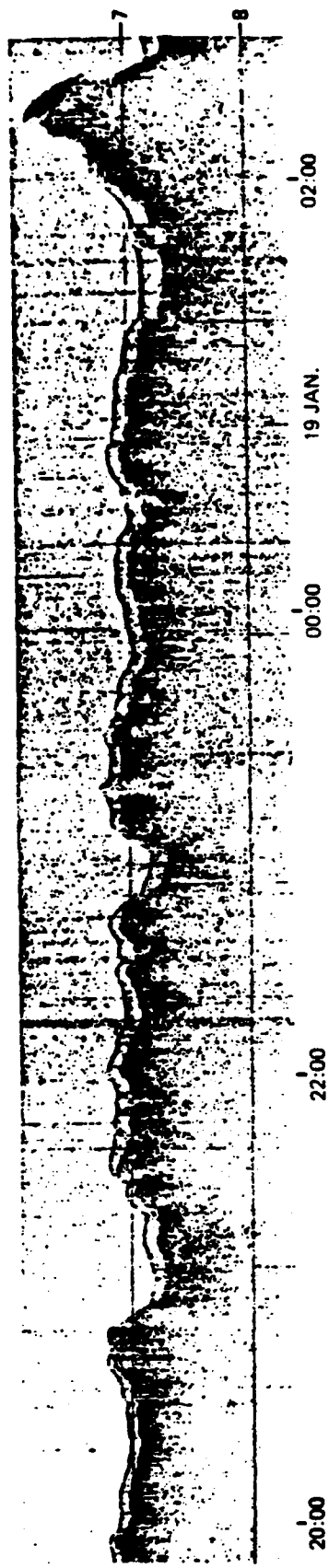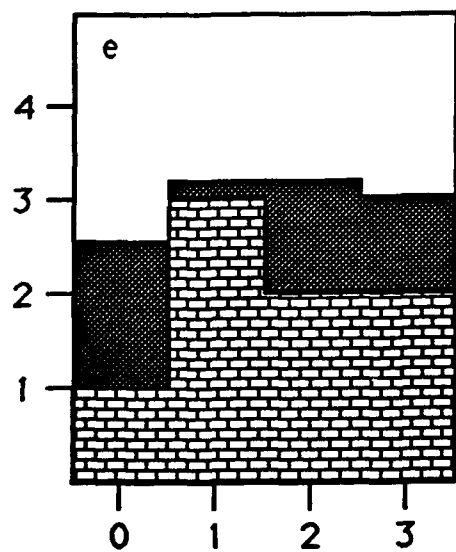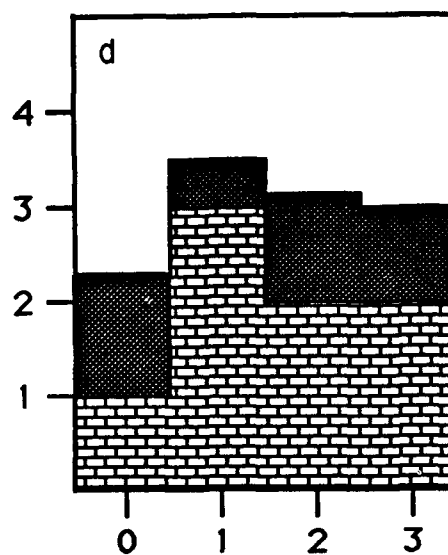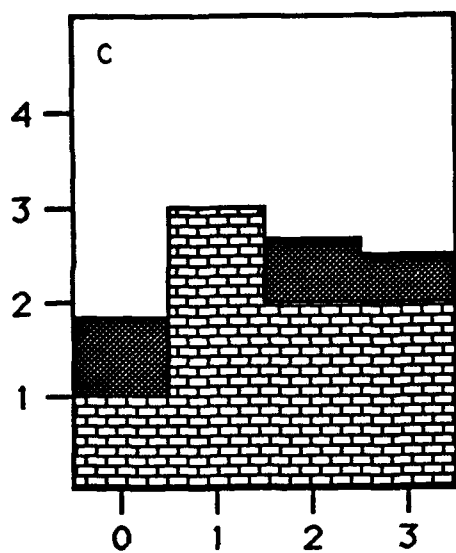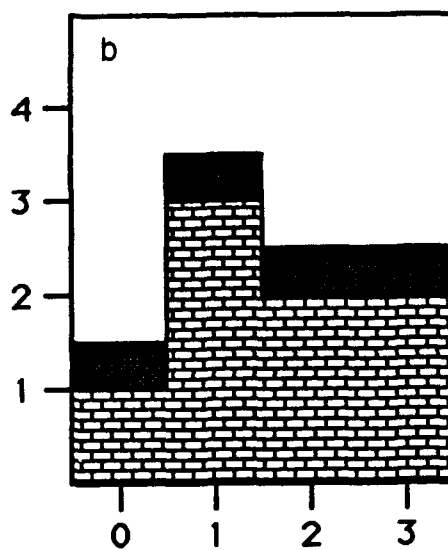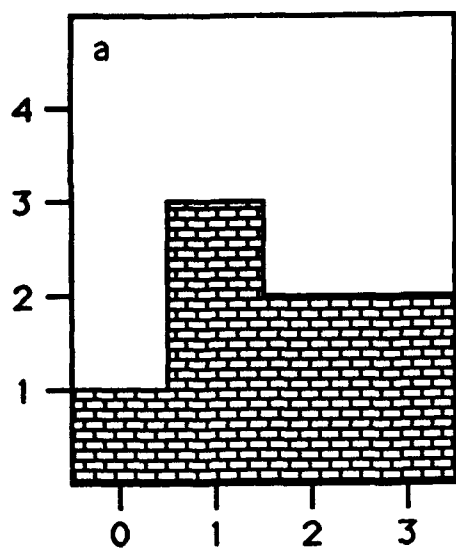
Figure 2

Figure 3

Figure 4

Basement

Figure 5(a)

Seafloor, $\kappa = 1600\ m^2/My$ $T = 5\ My$
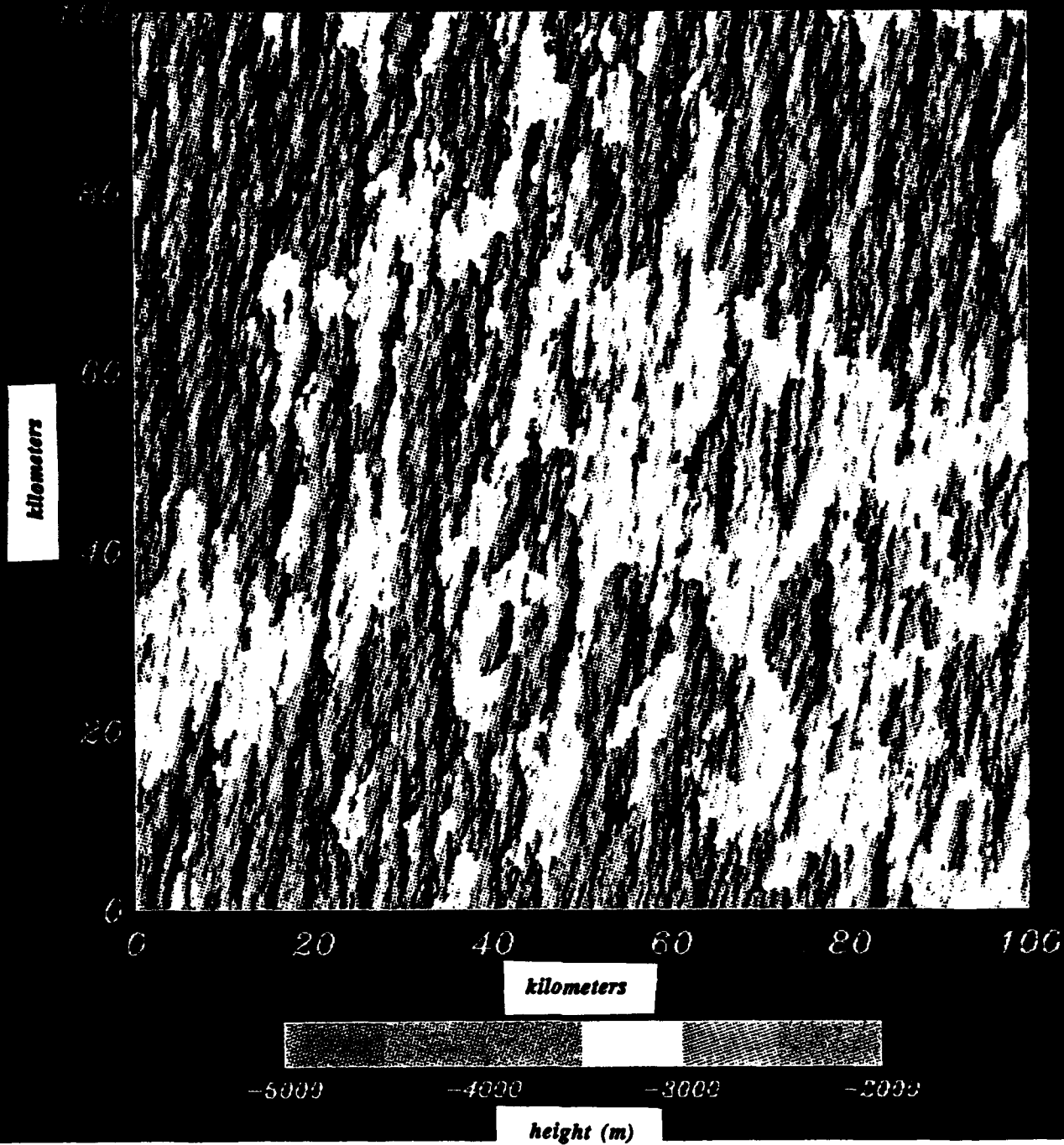
Figure 5(b)

Seafloor, $\kappa = 1600\ m^2/My$ $T = 20\ My$
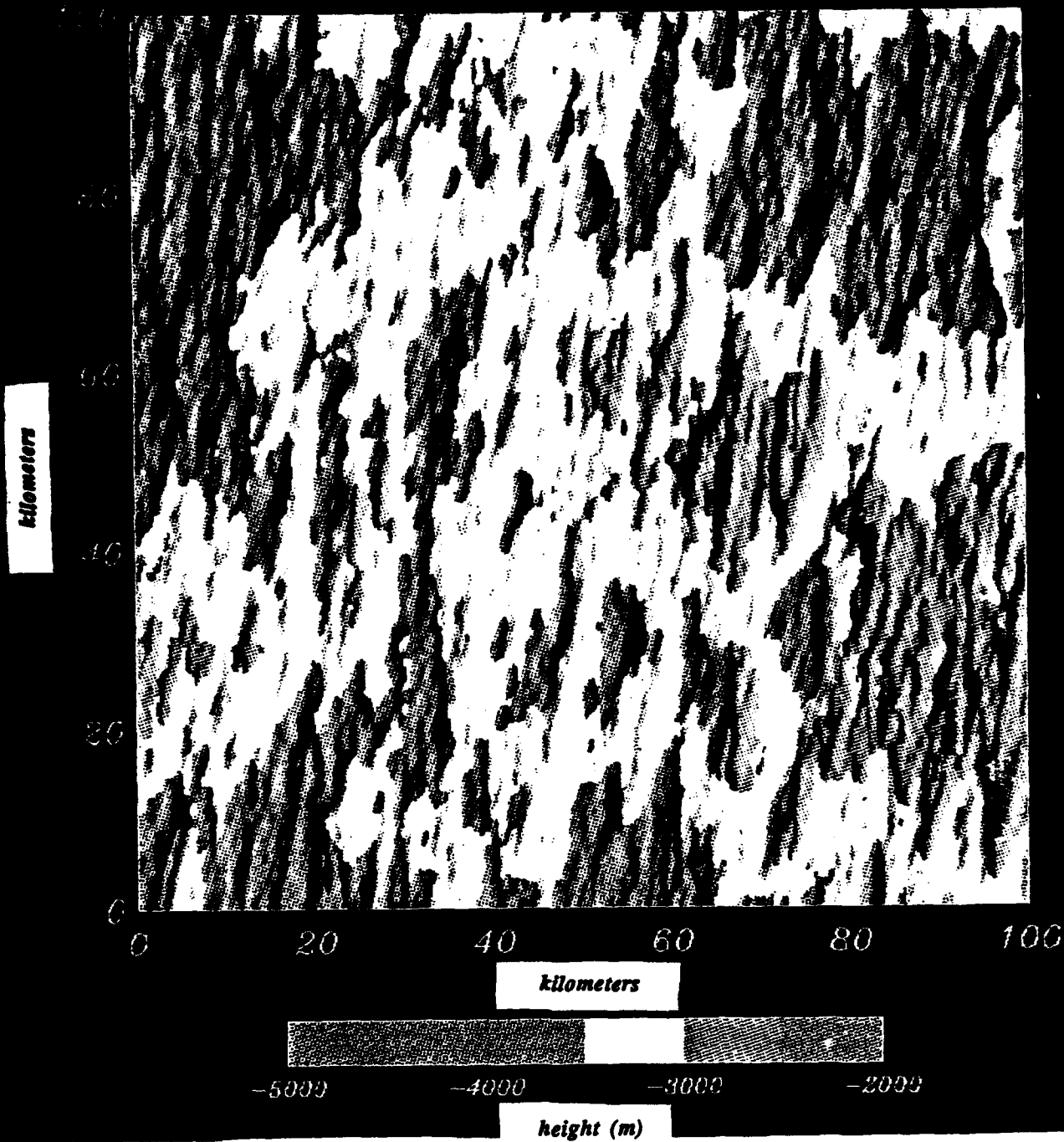
Figure 5(c)

Seafloor,   κ = 1,600,000 m²/My   T = 5 My

Figure 5(d)

Seafloor, $\kappa = 1,600,000 \ m^2/My$ $T = 20 \ My$
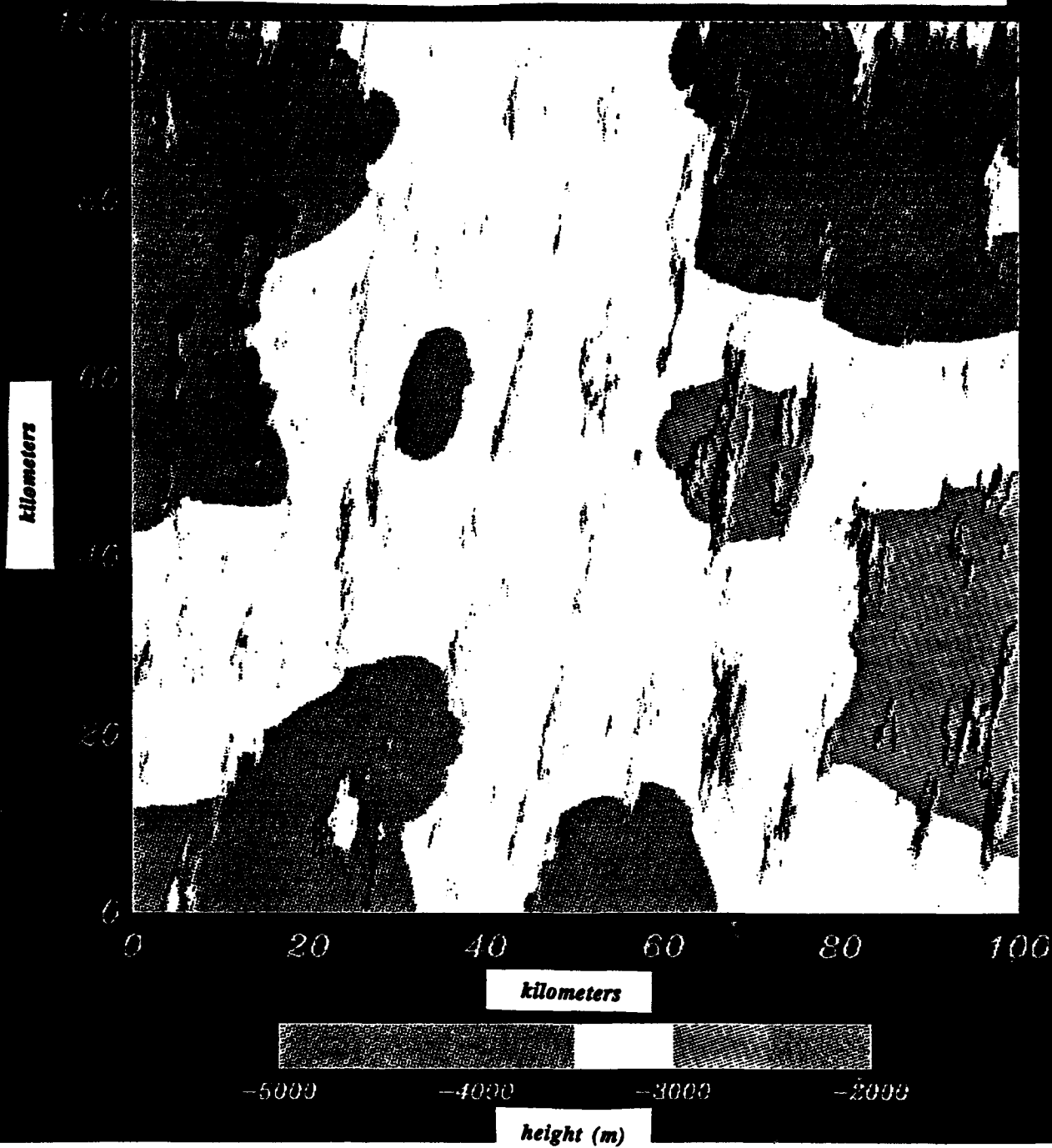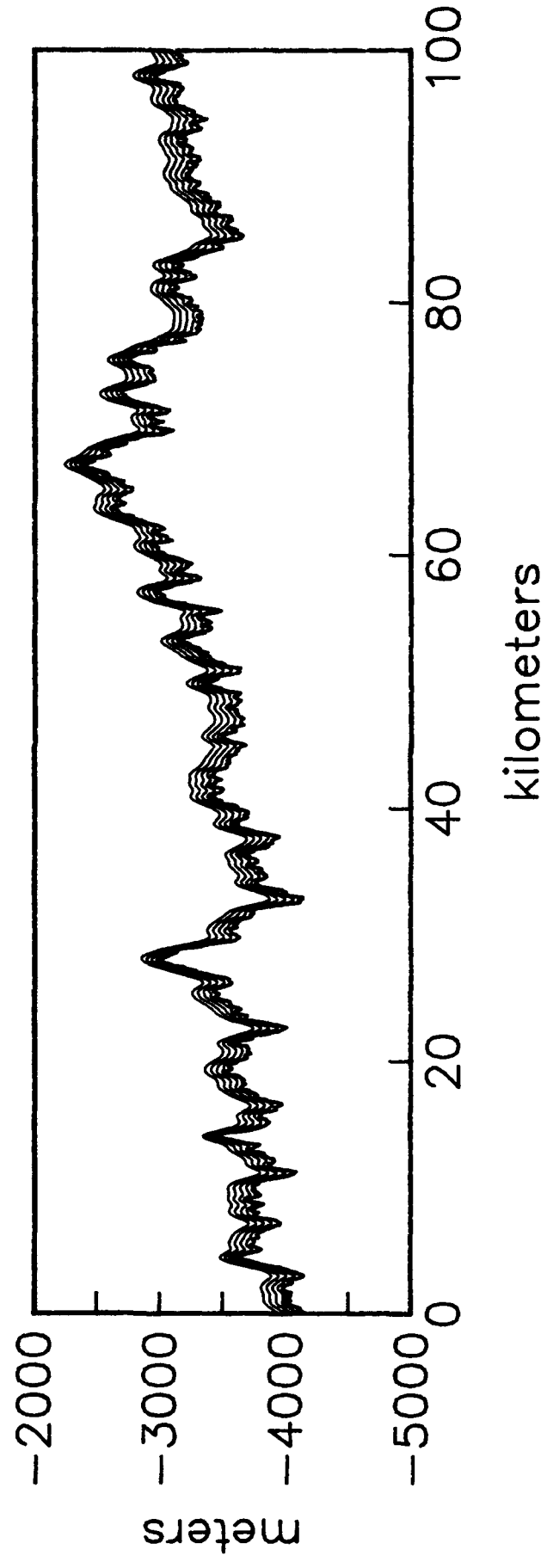
$\kappa = 1600 \ \text{m}^2/\text{My}$

Figure 6(a)

$\kappa = 16,000 \ \mathrm{m^2/My}$
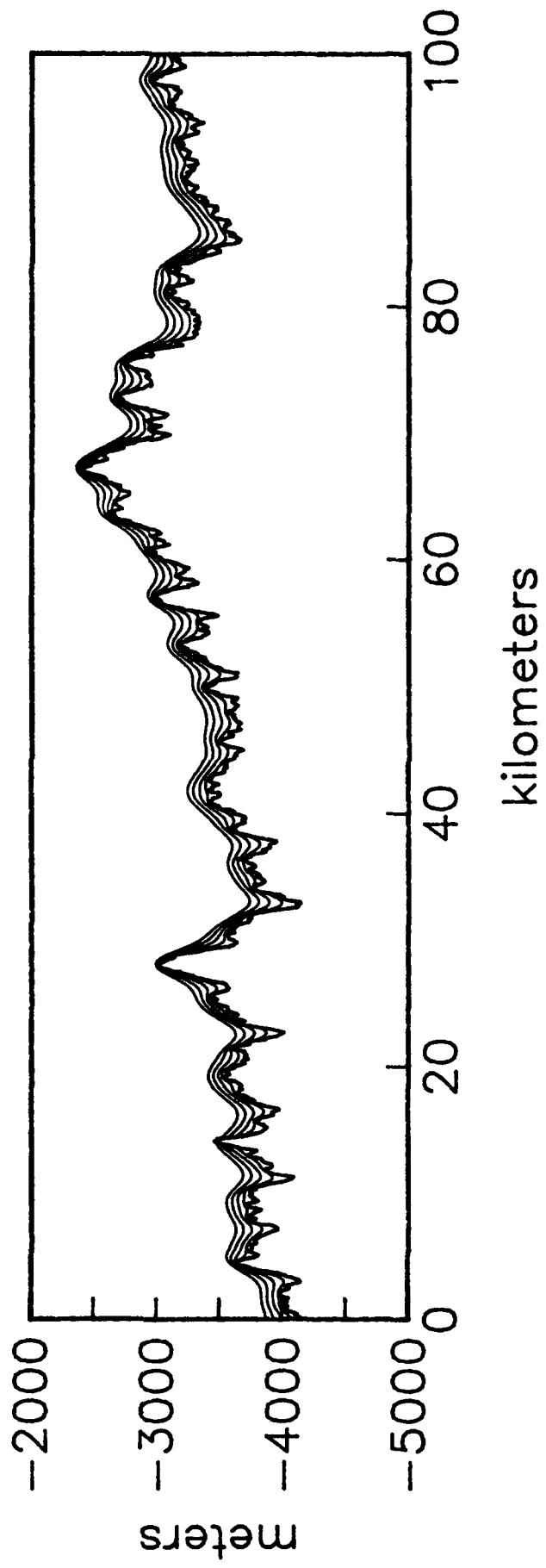
Figure 6(b)
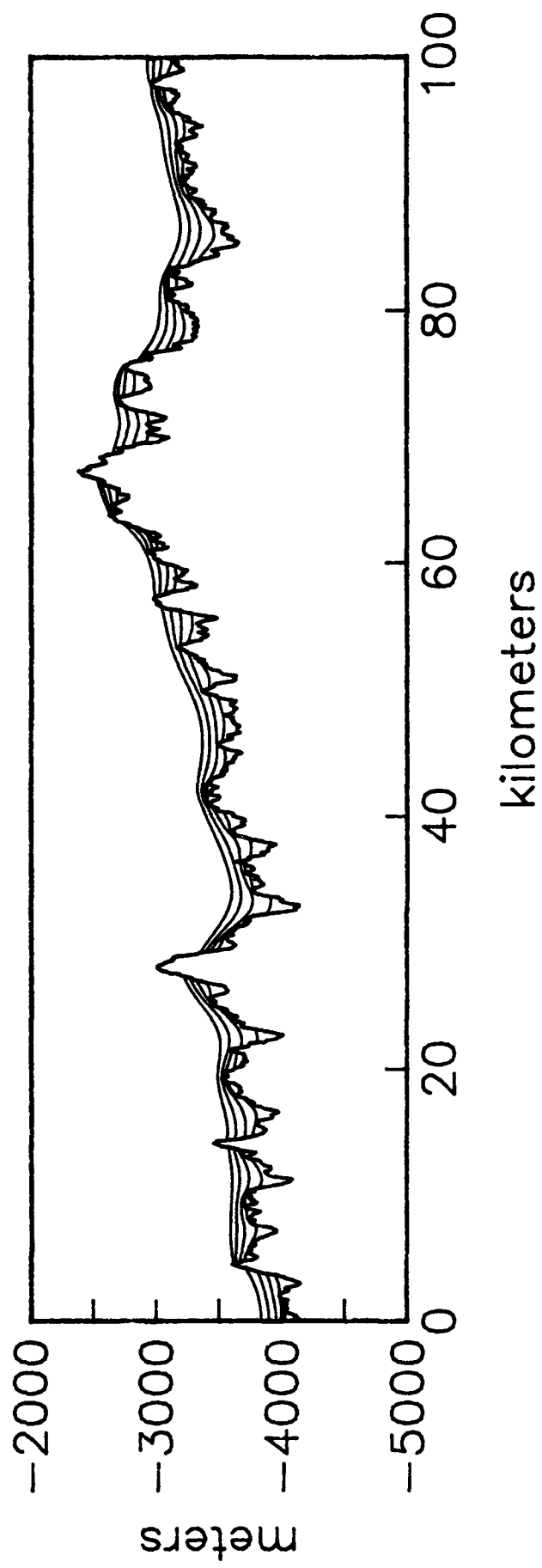
Figure 6(c)

$\kappa = 160,000 \ m^2/My$
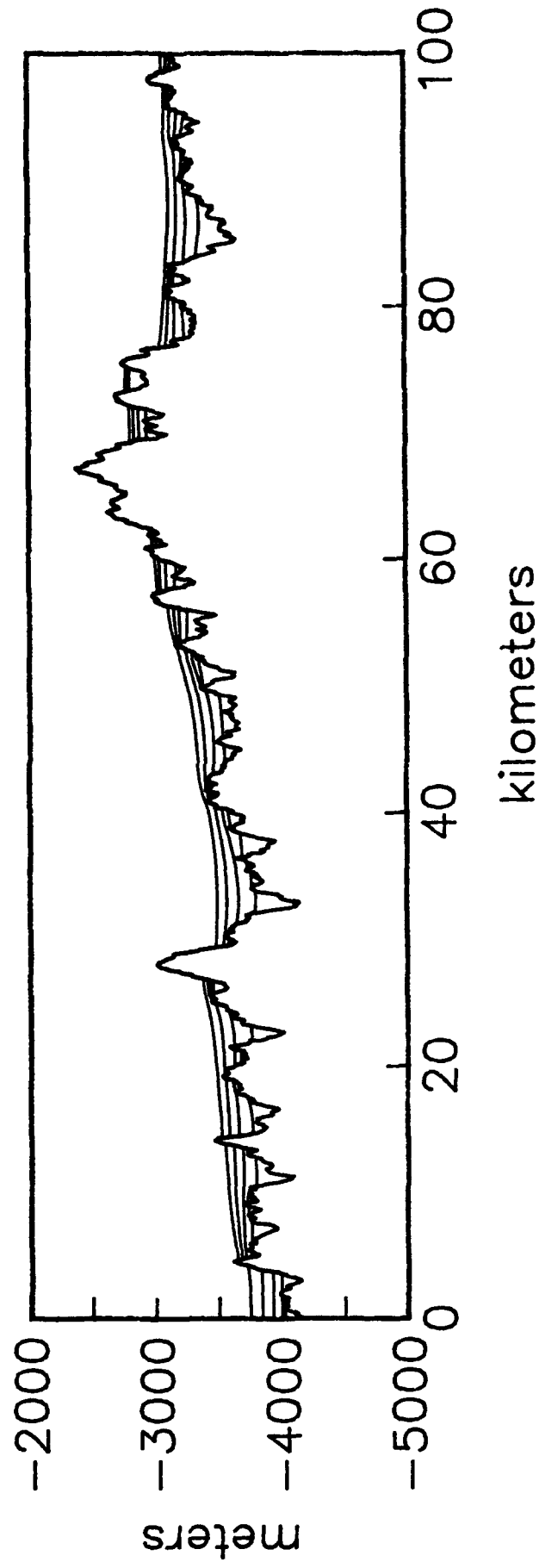
$\kappa = 1,600,000 \ \mathrm{m^2/My}$

Figure 6(d)

2D Profile: κ = 1600 m^2/My
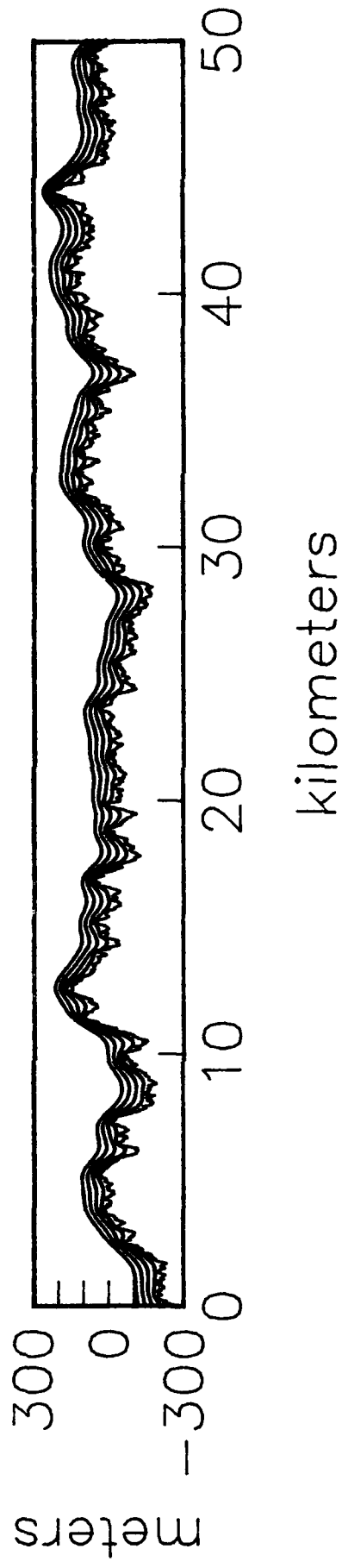
kilometers

meters

Figure 7(a)

2D Profile: κ = 16,000 m^2/My
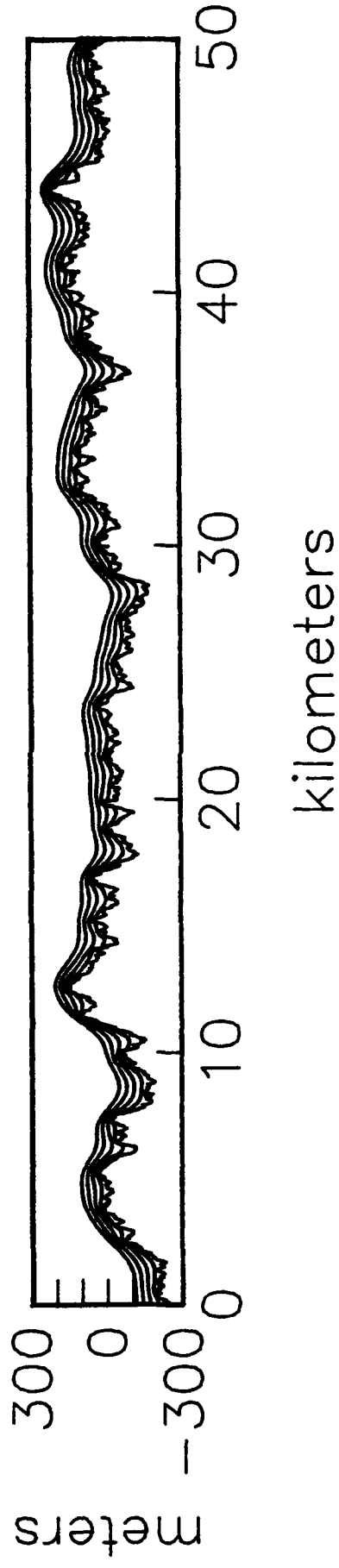
kilometers

meters

Figure 7(b)

2D Profile: $\kappa = 160,000 \ m^2/My$
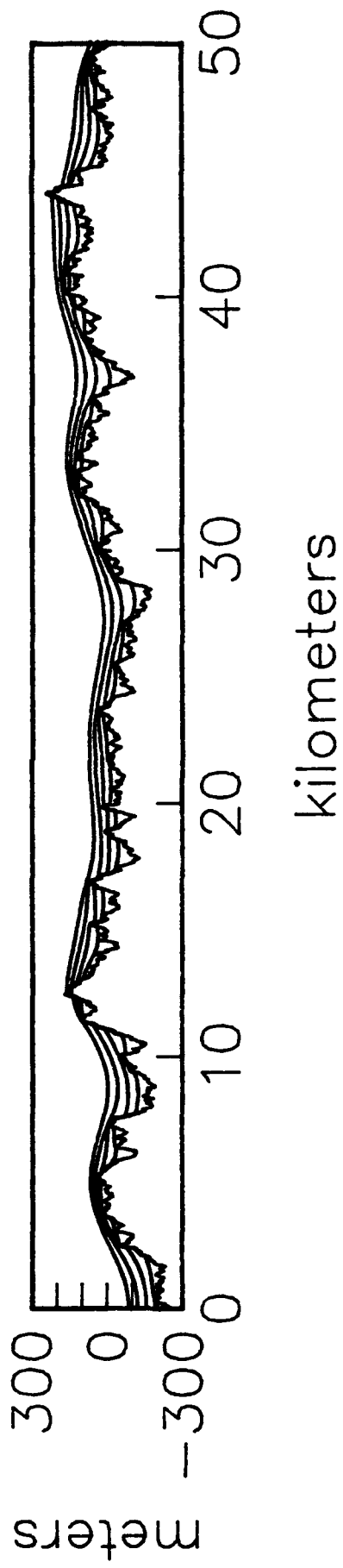
Figure 7(c)

2D Profile: κ = 1,600,000 m^2/My

kilometers
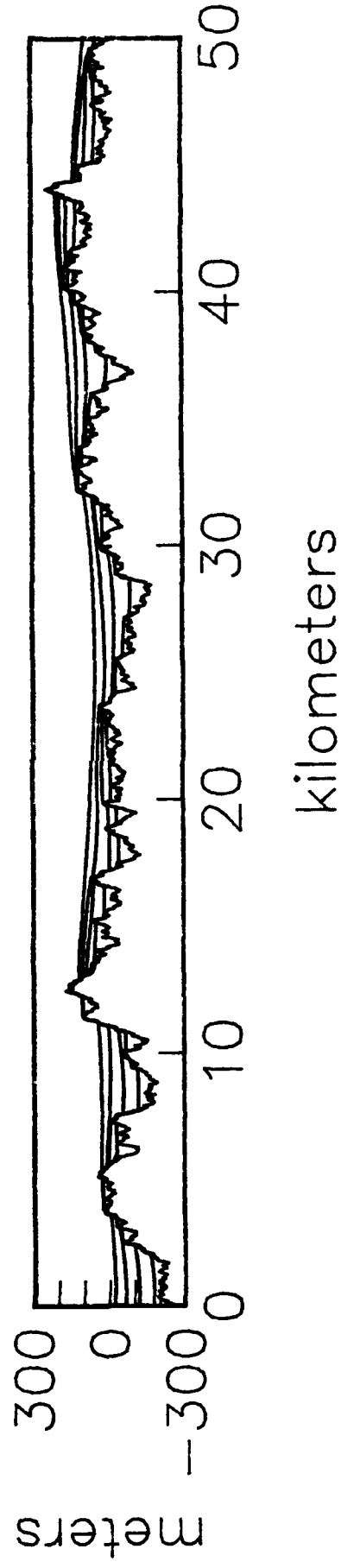
meters

Figure 7(d)

Figure 8(a)

Sediment Thickness, $\kappa = 1600 \, m^2/My$ $T = 5 \, My$
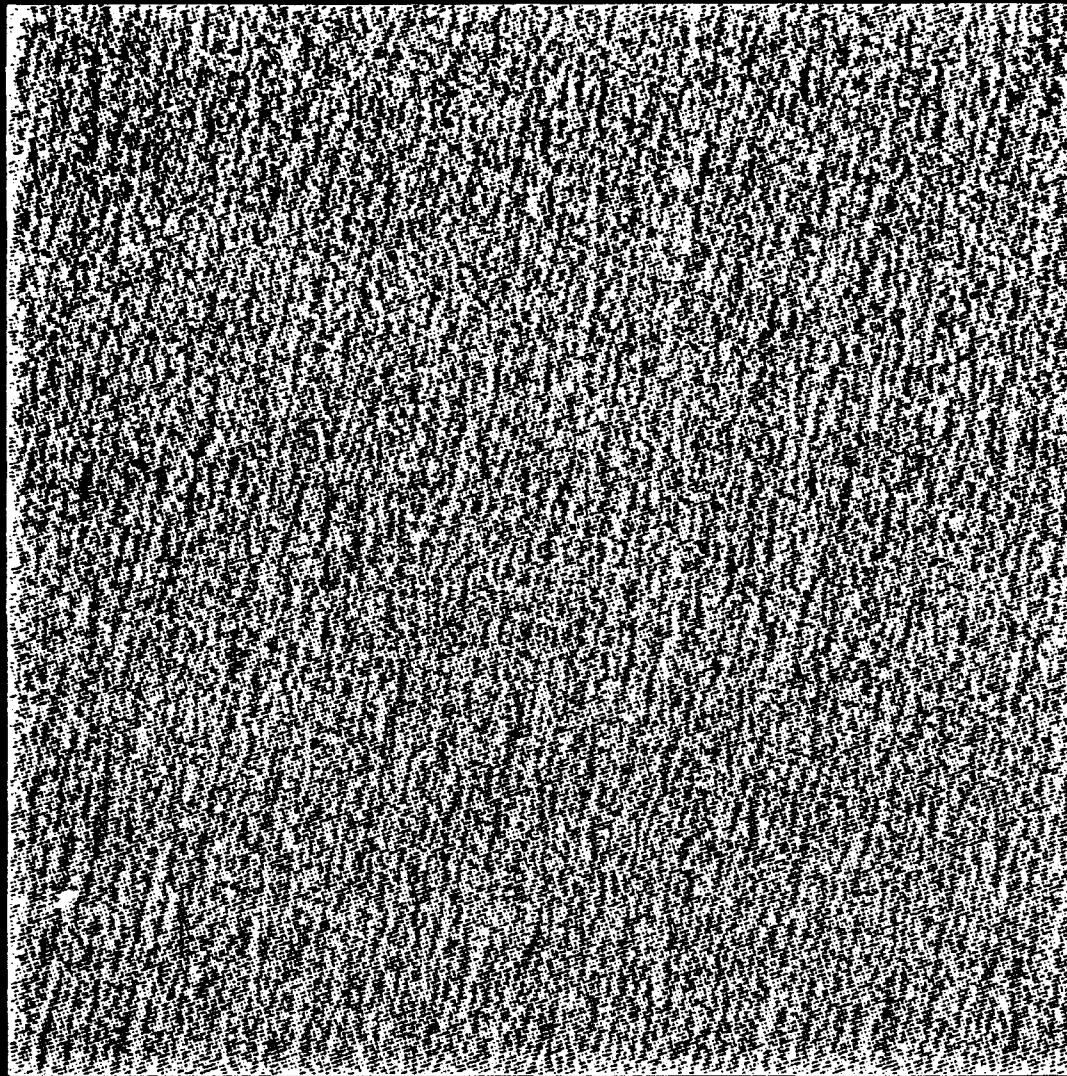
Figure 8(b)

Sediment Thickness, $\kappa = 1600\ m^2/My$ $T = 20\ My$

kilometers
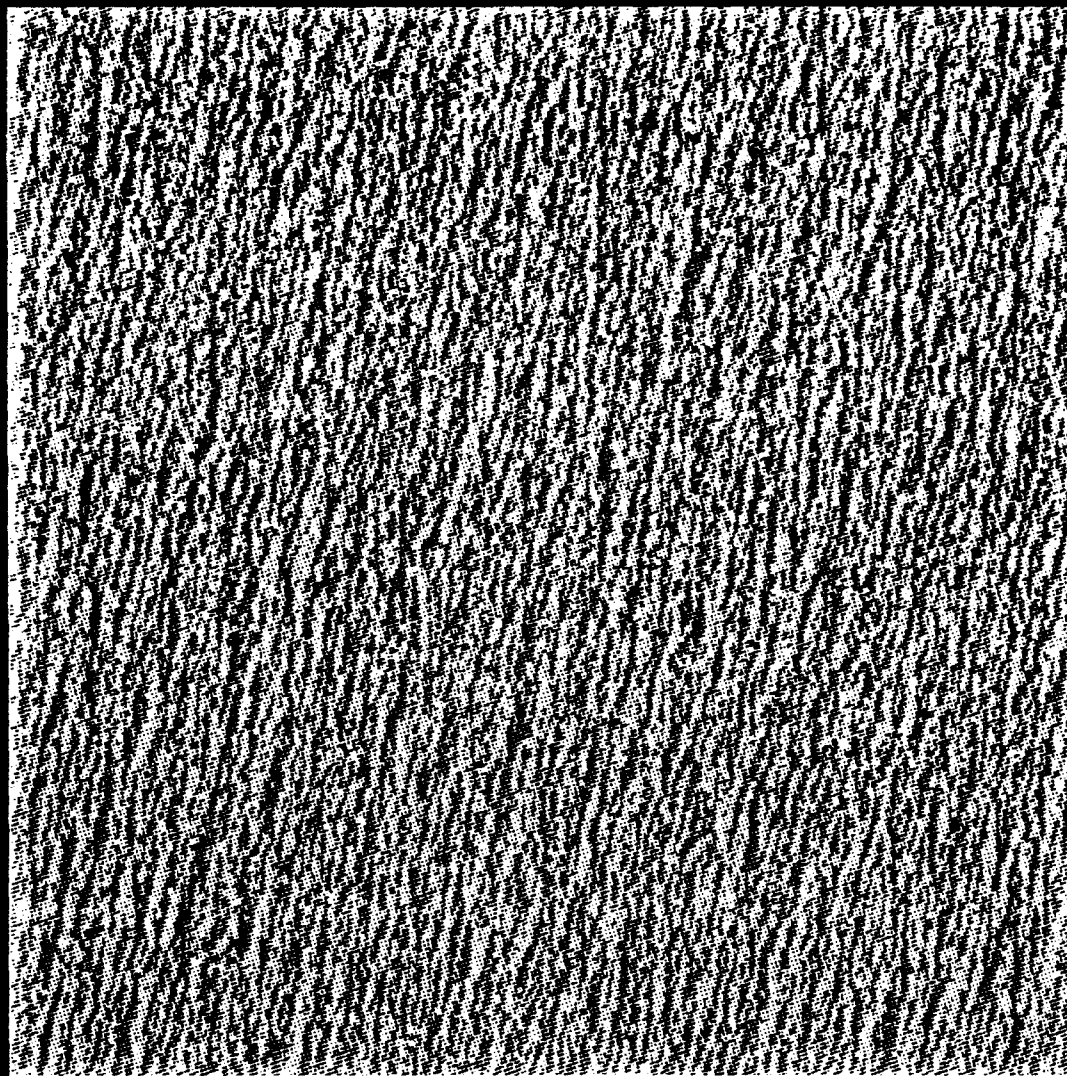
kilometers

thickness (m)

Figure 8(c)

Sediment Thickness, $\kappa = 1,600,000 \ m^2/My$ $T = 5 \ My$
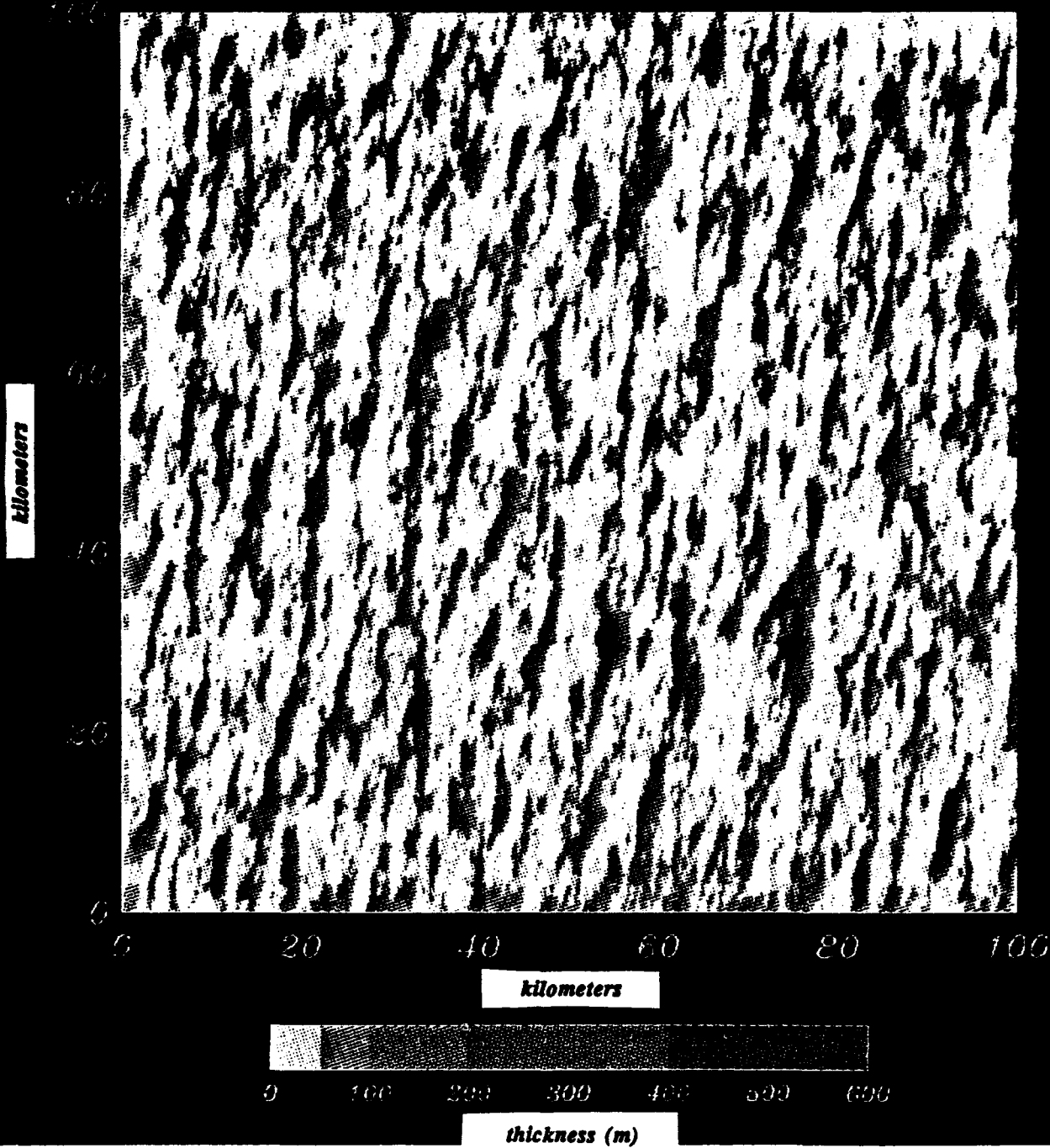
Figure 8(d)

Sediment Thickness, $\kappa = 1,600,000 \ m^2/My$ $T = 20 \ My$
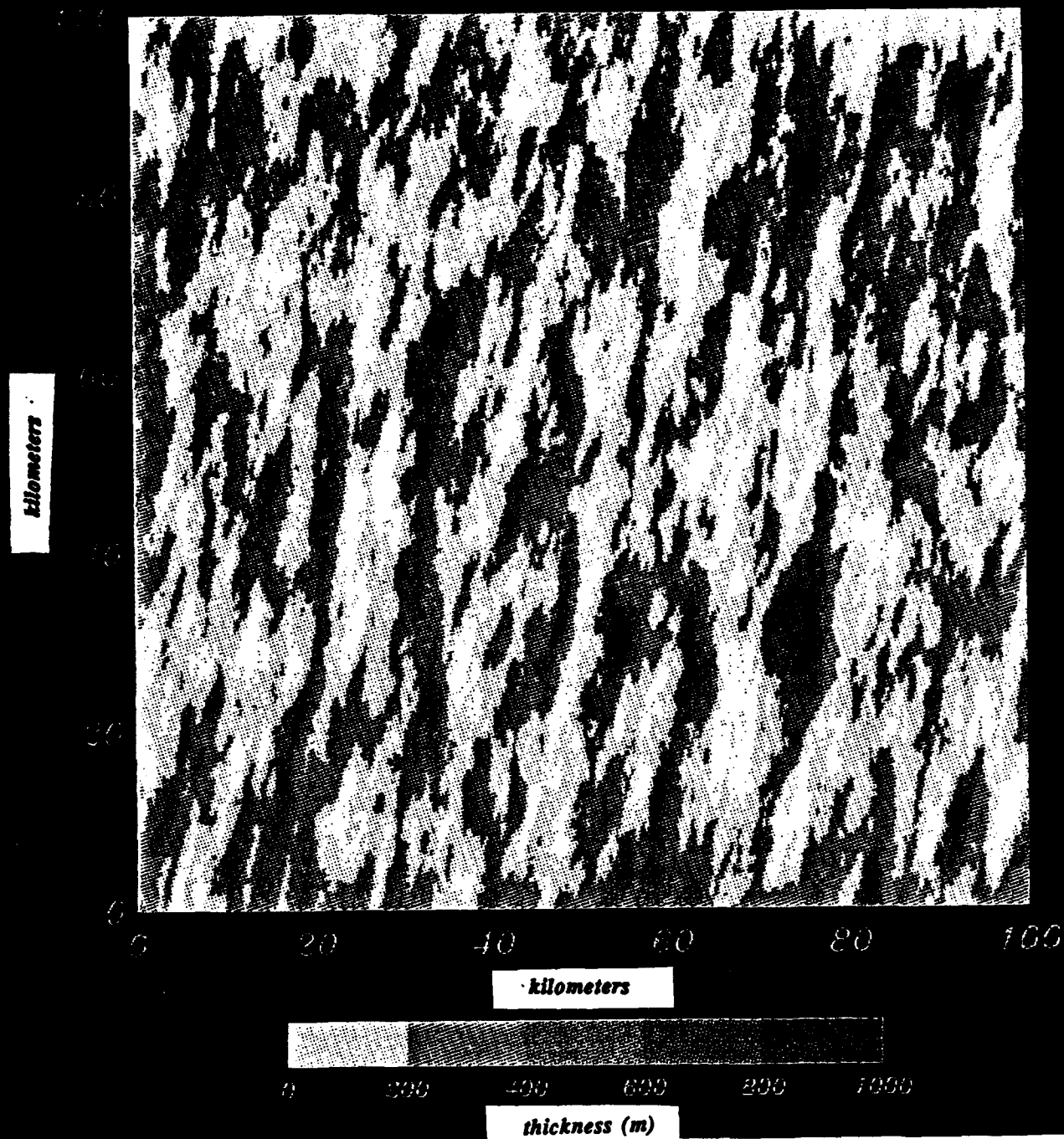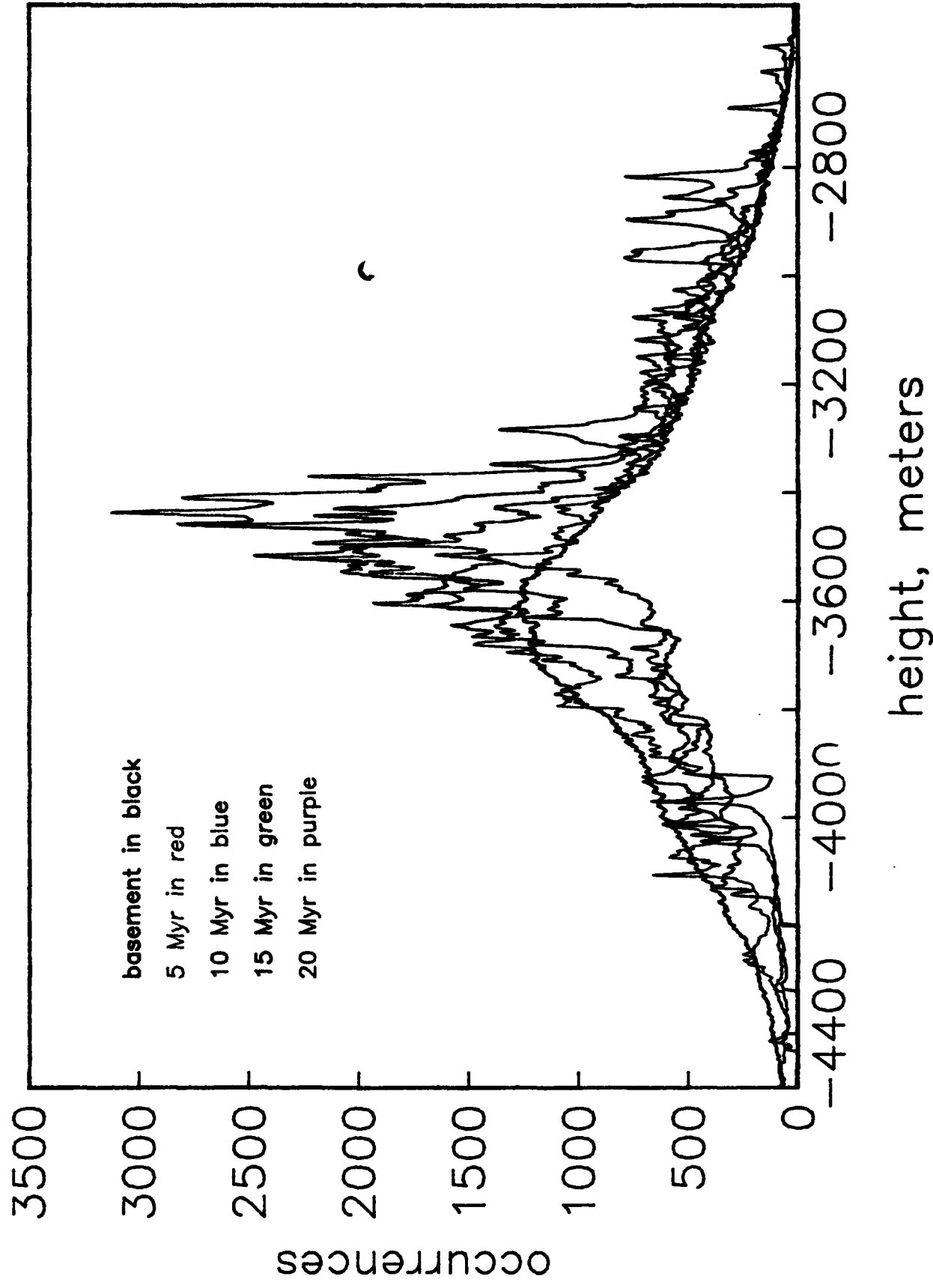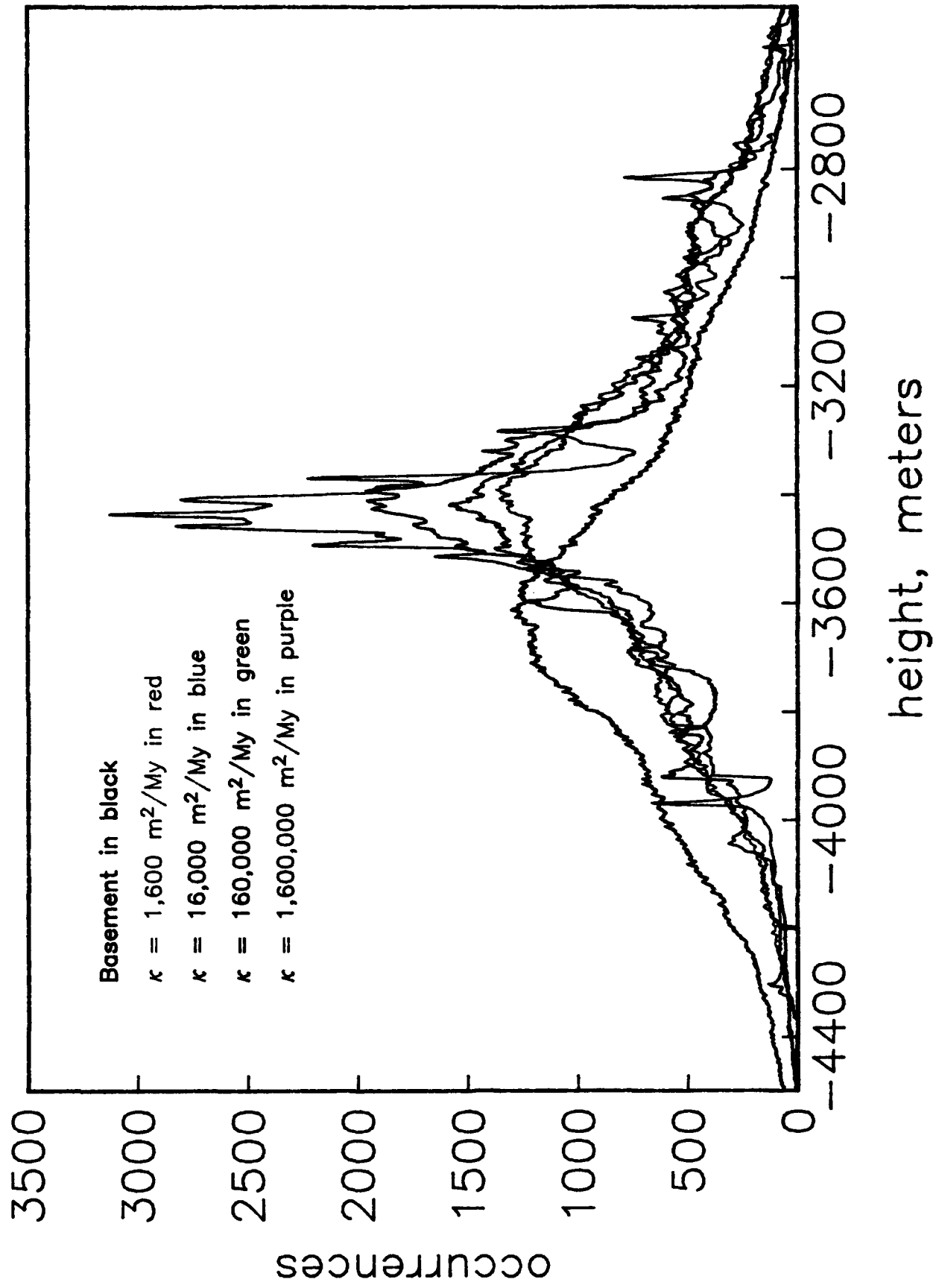
kilometers

thickness (m)

Figure 9

Figure 10

Sediment Thickness: $\kappa = 1,600,000 \ m^2/My$

T = 5 My in red
T = 10 My in blue
T = 15 My in green
T = 20 My in purple

thickness, meters

occurrences

Figure II

Sediment Thickness, T = 20 My

κ = 1,600 m²/My in red
κ = 16,000 m²/My in blue
κ = 160,000 m²/My in green
κ = 1,600,000 m²/My in purple

occurrences

thickness, meters

Figure 1a

2D Algorithm: T = 2.5 My

Basement in black
κ = 1,600 m²/My in red
κ = 16,000 m²/My in blue
κ = 160,000 m²/My in green
κ = 1,600,000 m²/My in purple

POWER, m²/(cycles/km)

WAVENUMBER, cycles/km
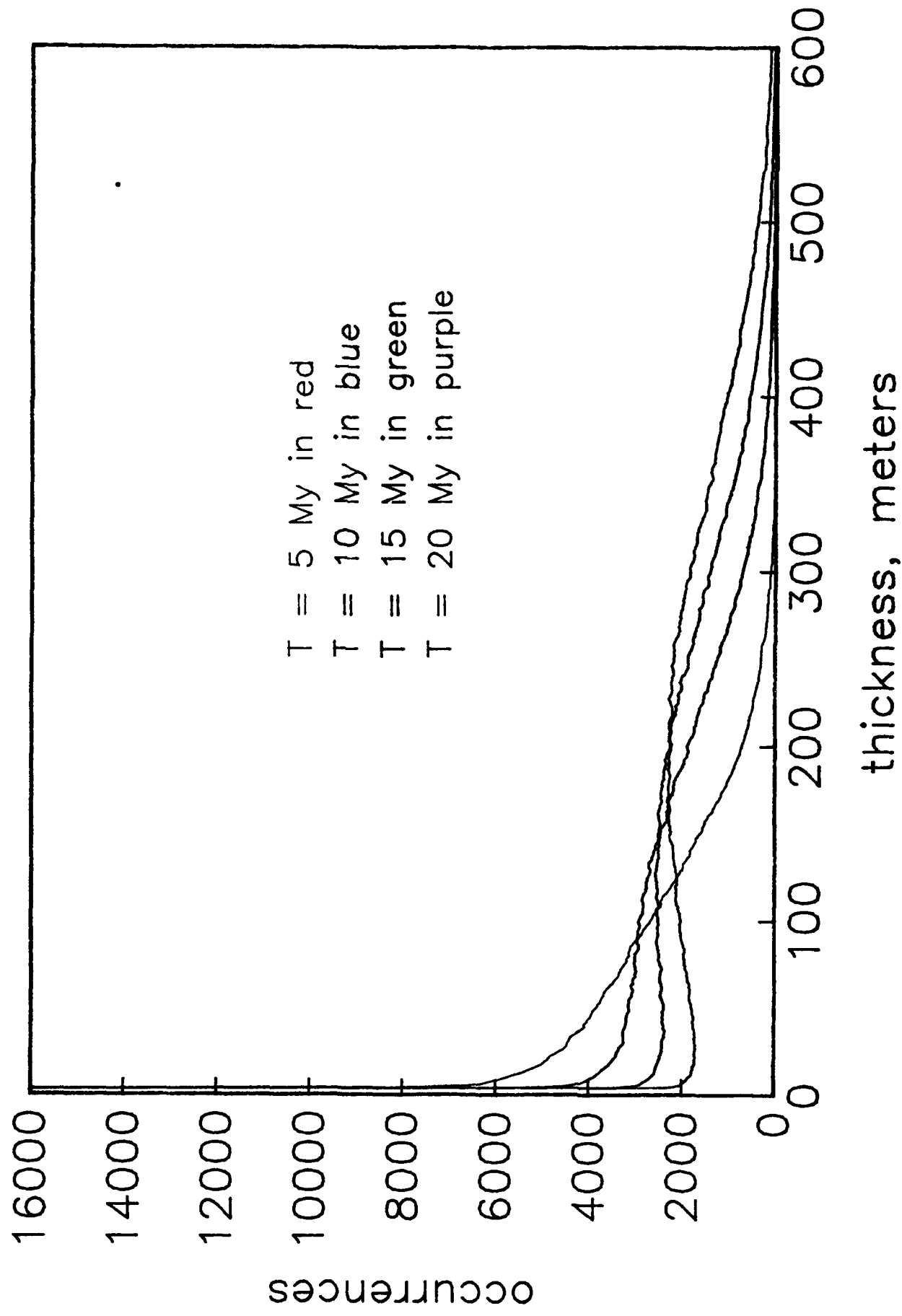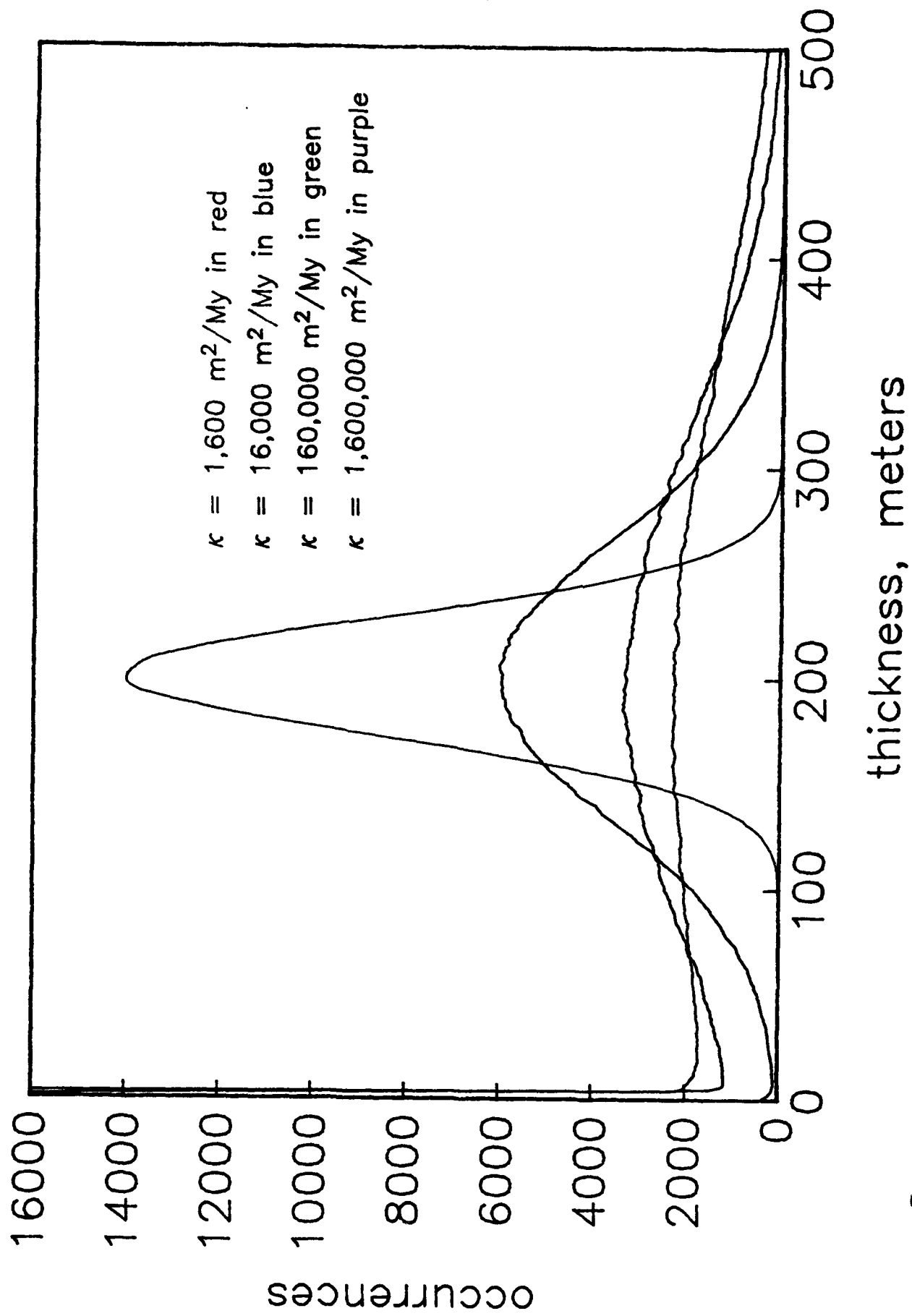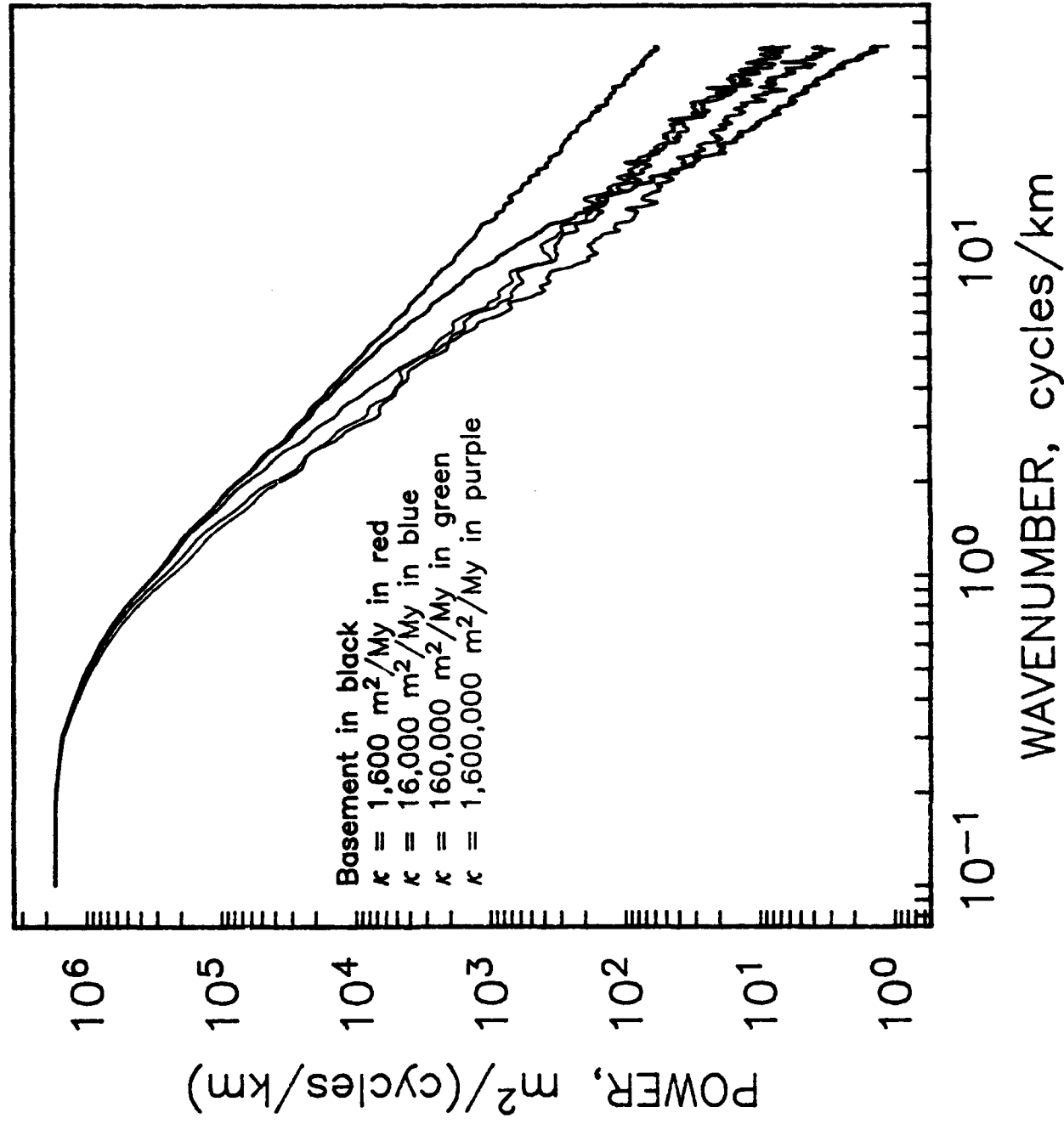
Figure 13

2D Algorithm: T = 10 My

Figure 14

POWER, m²/(cycles/km)

WAVENUMBER, cycles/km

Basement in black
κ = 1,600 m²/My in red
κ = 16,000 m²/My in blue
κ = 160,000 m²/My in green
κ = 1,600,000 m²/My in purple

2D Algorithm: $\kappa = 1,600 \ m^2/My$

Basement in black
T = 2.5 My in red
T = 5 My in blue
T = 7.5 My in green
T = 10 My in purple

WAVENUMBER, cycles/km

POWER, $m^2/(cycles/km)$

Figure 15

2D Algorithm: κ = 16,000 m²/My

Basement in black
T = 2.5 My in red
T = 5 My in blue
T = 7.5 My in green
T = 10 My in purple

WAVENUMBER, cycles/km

POWER, m²/(cycles/km)
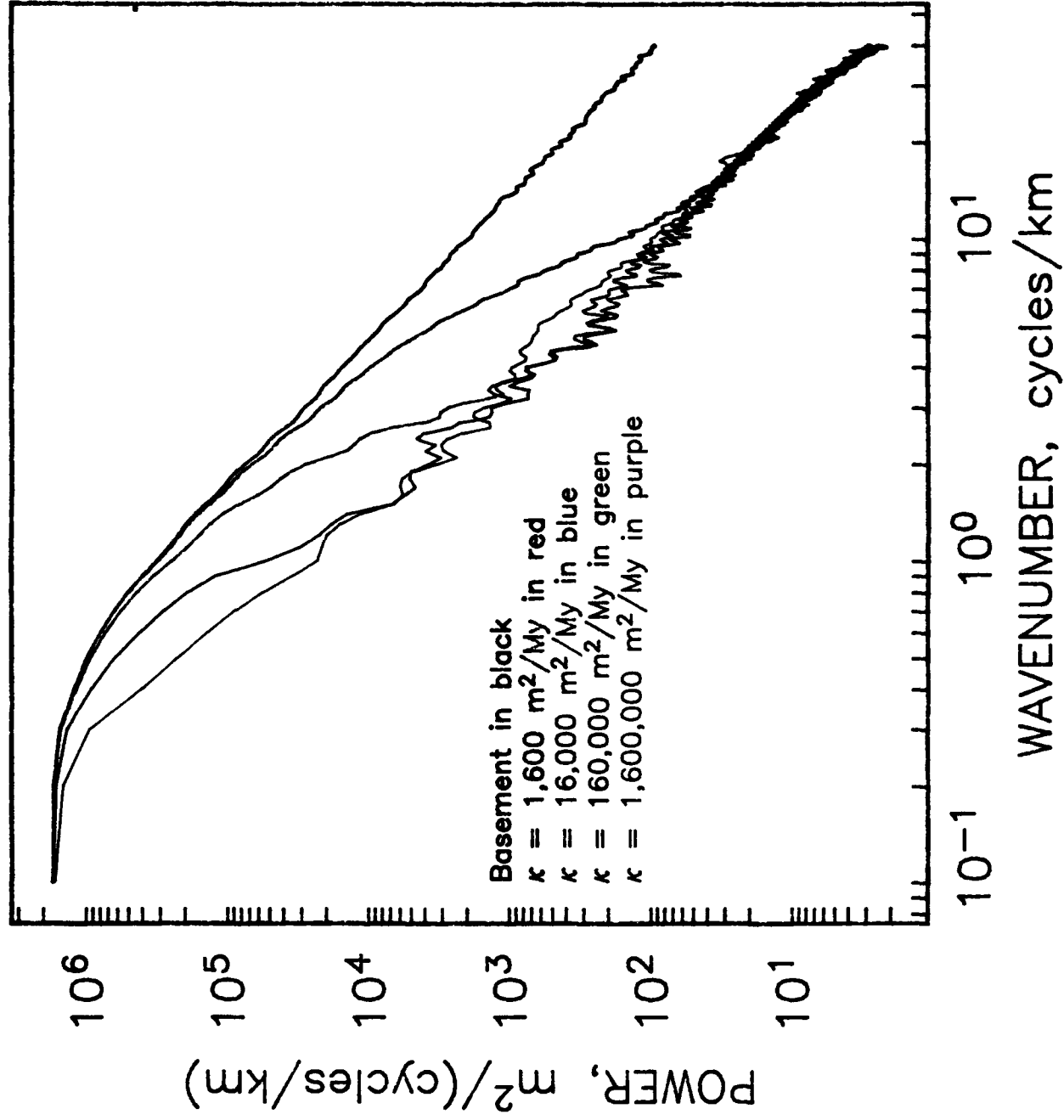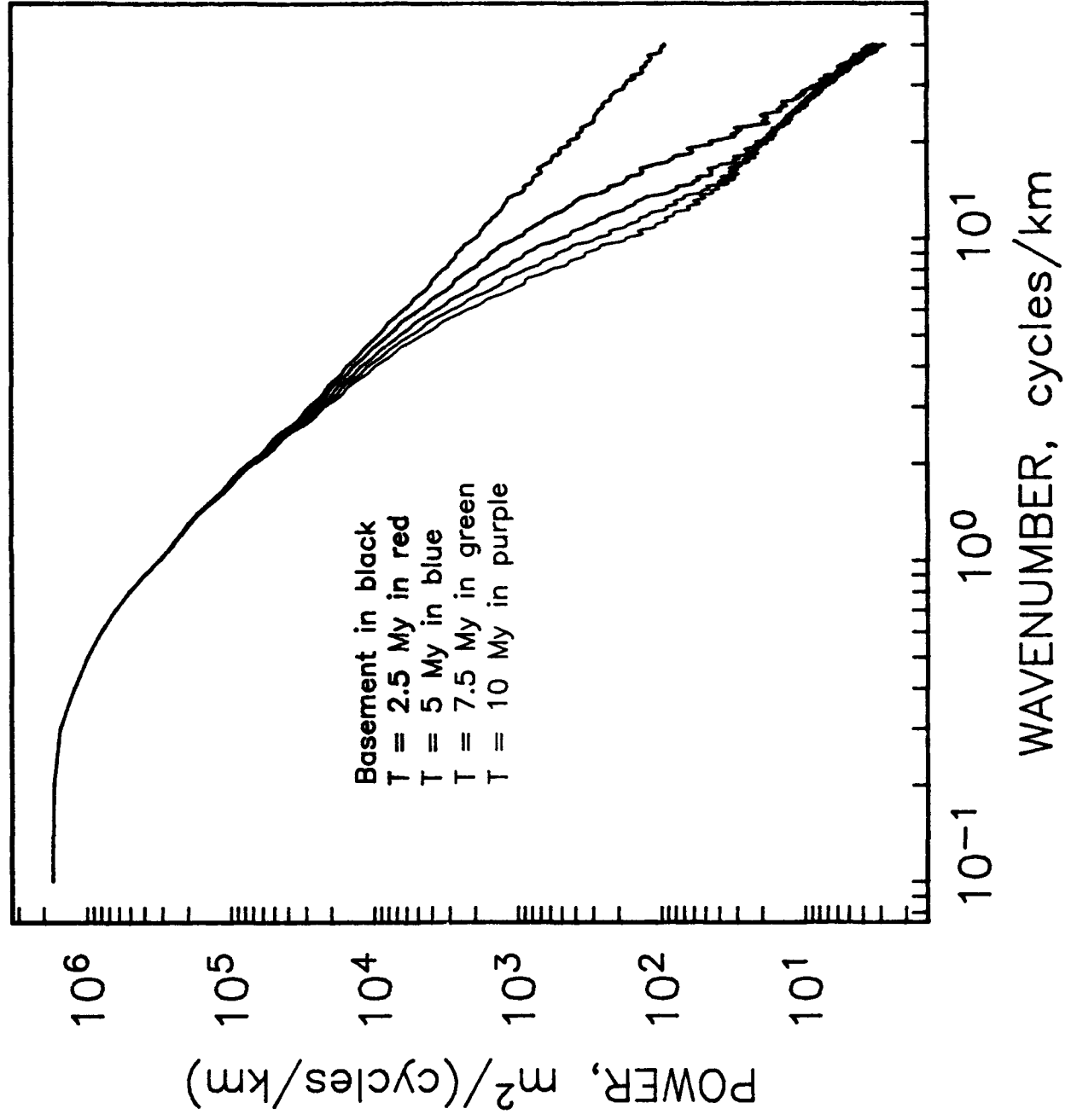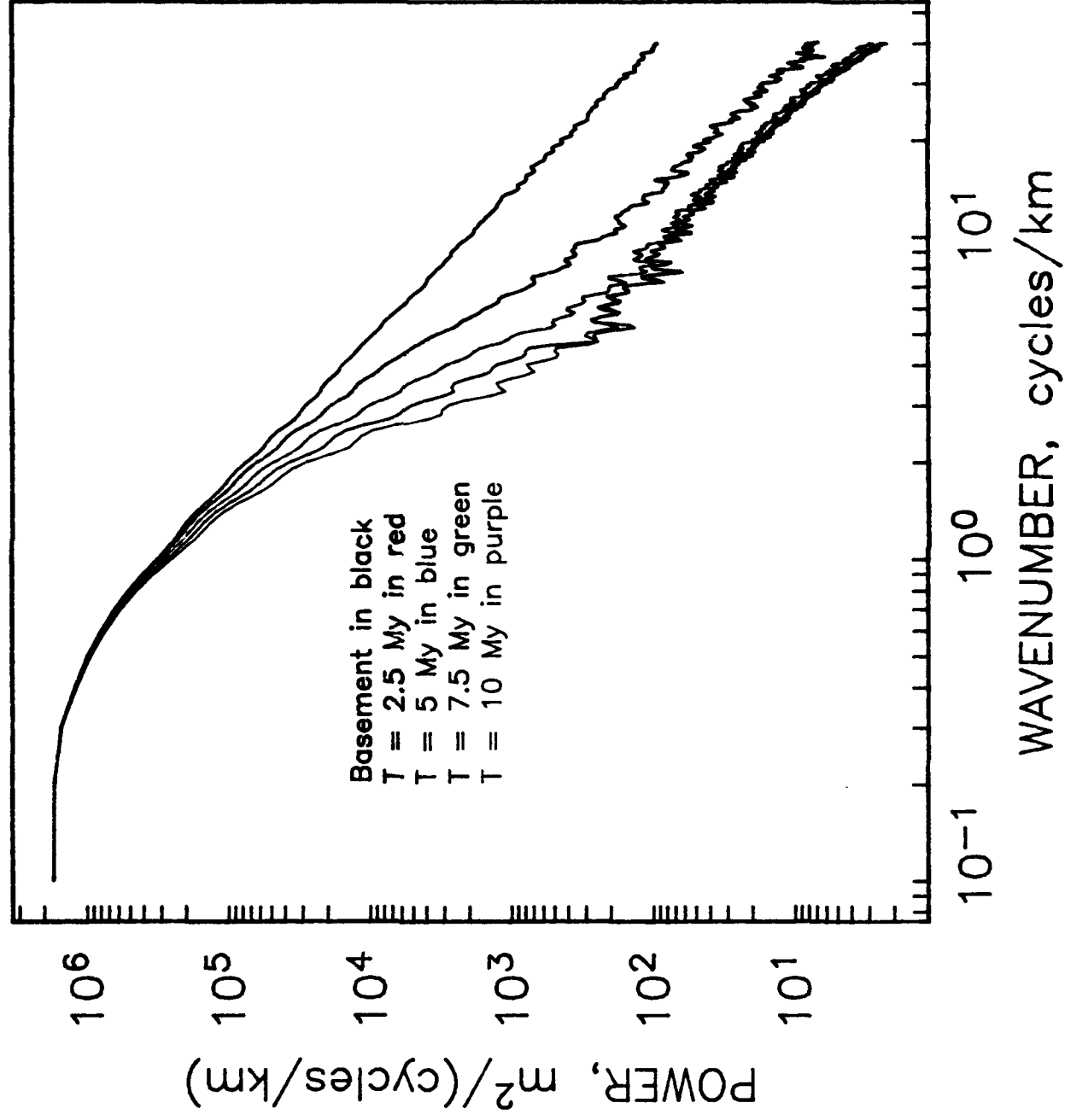
Figure 16

2D Algorithm: $\kappa = 160,000 \ m^2/My$

Basement in black
T = 2.5 My in red
T = 5 My in blue
T = 7.5 My in green
T = 10 My in purple

WAVENUMBER, cycles/km

POWER, $m^2/(cycles/km)$

Figure 17

2D Algorithm: κ = 1,600,000 m²/My

Basement in black
T = 2.5 My in red
T = 5 My in blue
T = 7.5 My in green
T = 10 My in purple

POWER, m²/(cycles/km)

WAVENUMBER, cycles/km
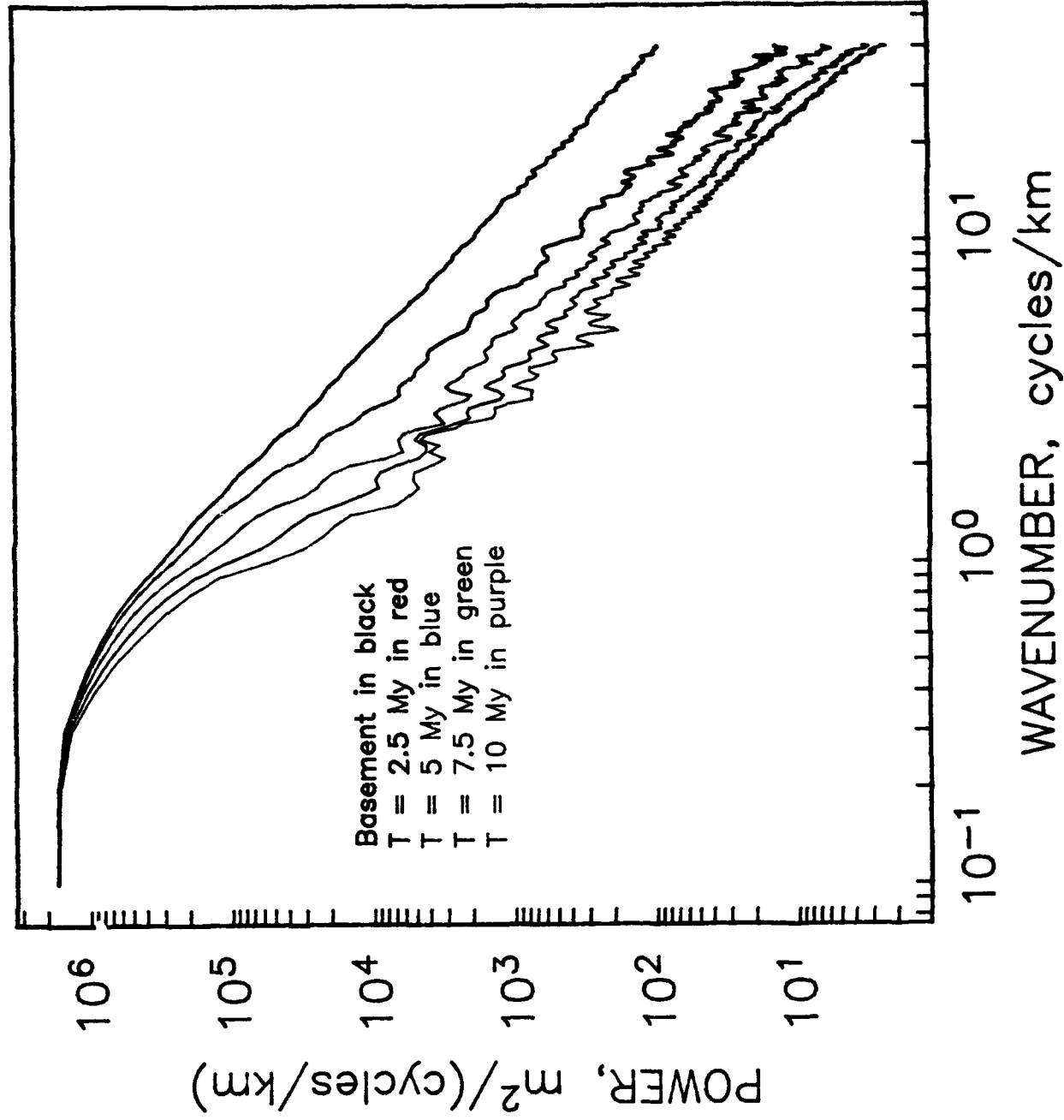
Figure 18

Stochastic Interpolation of a Wide-Beam Bathymetric Profile Within the ONR-ARSRP Acoustic Reverberation Corridor

John A. Goff[1], Helen F. Webb[2], and Thomas H. Jordan[2]

[1]*Department of Geology and Geophysics,
Woods Hole Oceanographic Institution, Woods Hole, MA 02543*

[2]*Department of Earth, Atmospheric and Planetary Sciences,
Massachusetts Institute of Technology, Cambridge, MA 02139*

SUMMARY

This technical report describes the procedure implemented in the stochastic interpolation of a bathymetric profile generated by a wide-beam echosounder. The principal purpose of this interpolation is to provide acoustic modelers with realistic, densely sampled profiles from which to predict backscatter pheno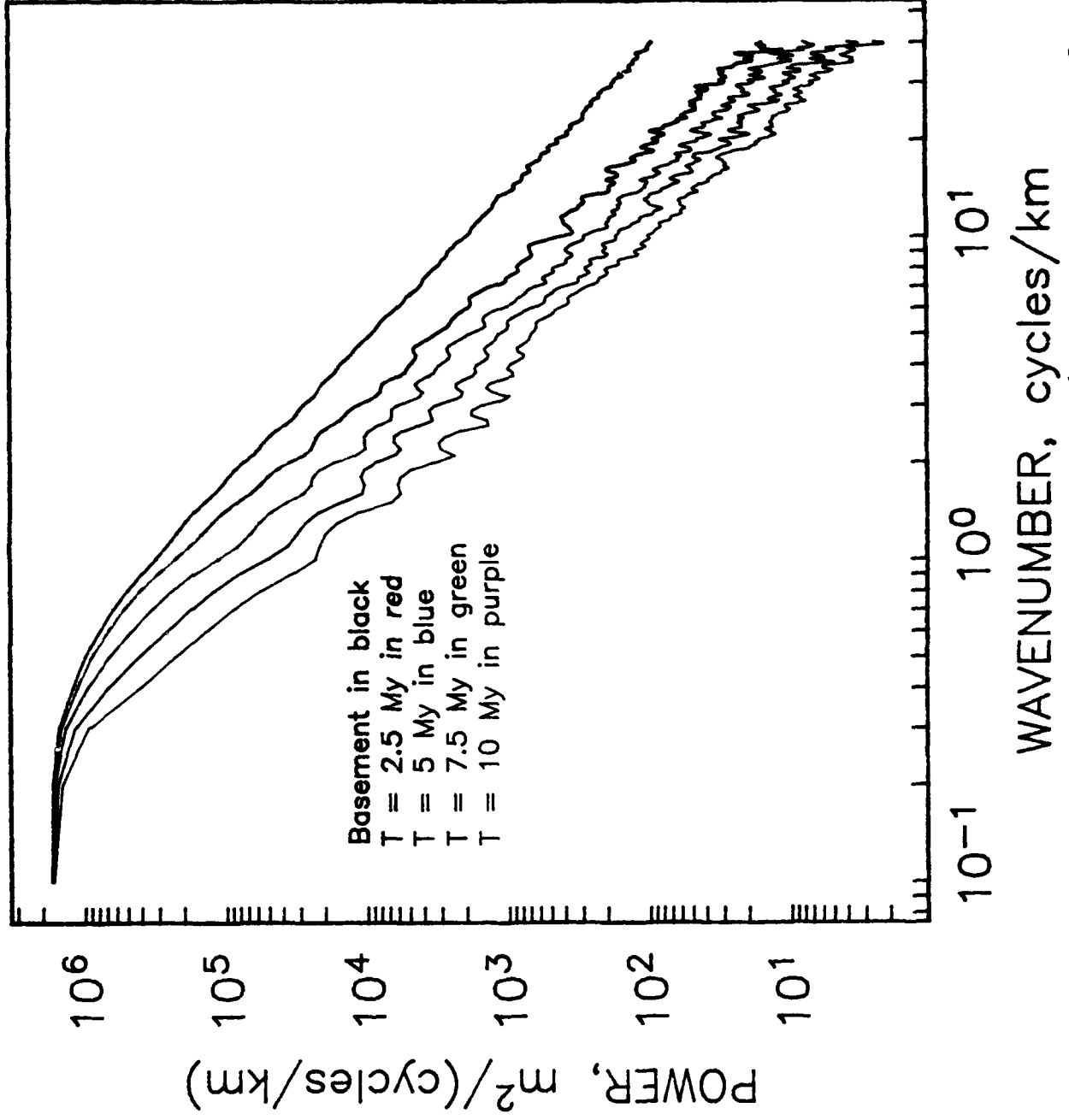mena. The profile chosen for interpolation, collected on the *Vema* 2602 cruise (V2602), passes through the ONR-ARSRP's acoustic reverberation corridor in the North Atlantic. After gridding the entire profile at data spacing of 1 km, three 20 km subsets were chosen for stochastic interpolation to 1 m data spacing. These sites are located near target areas for the 1991 acoustic reconnaissance experiment. Two sites, B and C, correspond, respectively, to a rough plateau and a steep escarpment. Site A corresponds to a sediment pond. For this site we estimated basement depths from the V2602 seismic profile and applied the interpolation to basement depths only. For sites B and C we postulate a thin veneer of sediments which fill the smaller nooks and crannies and which cannot be detected by the seismic profiler. To simulate this possible effect we have employed a numerical model for sedimenting a rough surface. The original and interpolated profiles, along with sediment depths (observed for site A, numerically estimated for sites B and C) for each will be provided to all interested ARSRP participants.

TABLE OF CONTENTS

1. INTRODUCTION

One of the primary goals of ONR's Acoustic Reverberation SRP (ARSRP) is to model the reverberation of acoustic energy from realistic representations of the ocean floor. The ocean floor, especially the basement generated at mid-ocean ridges, is rough, and contains features at all measurable scales. Currently, our principal and most successful means of modeling acoustic interaction with a rough interface is through numerical modeling (e.g. finite differences, finite elements, integral equations, etc.). This presents us with an unfortunate problem: our ability to deterministically map the seafloor falls far short of the detail that acoustic modelers need to accurately predict acoustic reverberation. For example, for the wavelengths considered in the ARSRP, ~15 m, the seafloor must be accurately represented at the meter scale or less. By contrast, surface operated swath mapping systems (e.g. Sea Beam, Sea Beam 2000, Hydrosweep, SeaMARC II, etc.), the only bathymetric instruments that have the ability to ensonify large enough tracts of ocean floor to be of interest to Navy needs, have lateral resolutions in deep water of 100 m at best.

For some purposes, the two orders of magnitude gap between what is needed by acoustic modelers and what can be delivered by seafloor mappers can be filled by extrapolation to high wavenumbers (interpolation to small scales) through the application of stochastic modeling techniques. Stochastic models, such as parameterizations of the covariance function or power spectrum, even very simple ones, inherently describe the statistical properties of morphology at all scales. For example, fractal models [e.g. *Bell*, 1975; *Mandelbrot*, 1983; *Fox and Hayes*; 1985; *Gilbert and Malinverno*; 1988; *Goff and Jordan*; 1988] predict that the statistical characteristics of small scale features are related, ad infinitum, to those of large scale features by a simple self-affine relationship. Thus, if the large scale/low wavenumber morphology is known, the small scale/high wavenumber morphology can be predicted. In the wavenumber domain, simple fractal models can be represented as straight lines in a log-log plot of the power spectrum for a topographic profile. The slope of this line determines the fractal dimension. High wavenumber extrapolation is accomplished simply by extending that line to higher wavenumbers than are resolved.

In the abyssal hill morphology encompassed by the ARSRP acoustic reverberation corridor (Figure 1), we have little indication as to whether the statistical behavior of small scale features can accurately be predicted, either by fractal or other models, from the statistical behavior of larger scale features. The geophysical reconnaissance portion of the ARSRP will address this question. Some encouragement comes from existing data in other

---

GOFF, WEBB, AND JORDAN   ARSRP TECHNICAL REPORT 2   PAGE 2

regions, however. For example, using both Sea Beam and Deep-Tow bathymetric data near the axis of the Galapagos ridge, *Goff and Kleinrock* [1991] demonstrated that a uniform fractal behavior can extend from the kilometer scale down to the ten meter scale.

Realistic stochastic models of seafloor morphology aid acoustic modelers in two ways: (1) by providing the basis for analytic acoustic models on ensembled sets and (2) by providing the means of generating realistic simulations or interpolations of bathymetry to arbitrary resolution and scale for use in numerical modeling procedures. It is in the latter capacity that this technical report is directed. In the first of these ARSRP technical reports [*Goff and Jordan*, 1990], an algorithm was presented for stochastically interpolating 2-D bathymetric data. In this report we specialize to 1-D bathymetric profiles. There are two motivations for this: (1) the current state of the art in acoustic modeling is best developed for 1-D and (2) we can generate long, highly resolved interpolations without the extensive nesting geometry that was necessary, due to space limitations, in 2-D.

To take advantage of the ARSRP acoustic reconnaissance experiment we have selected a wide beam profile from the *RV Vema* cruise 2602 (V2602) which passes through the acoustic reverberation corridor (Figure 1). This track line passes very near three of the acoustic target sites which were chosen in the planning stage of the cruise (Figure 1). Subsets of this profile, each 20 km long, representing the nearest passage of the V2602 track line to these target sites (see profile, Figure 2) were chosen for stochastic interpolation.

The interpolated, stochastic component of the profile is obtained as a single (arbitrary) realization of the three-parameter Gaussian-random-field model developed by *Goff and Jordan* [1988, 1989a] to represent 1-D abyssal-hill topography. The parameters include the rms height, H, the scale parameter, or corner wavenumber k_θ, and the fractal dimension D (valid at wavenumbers much greater than the corner wavenumber). In Section 3, we review the stochastic model and describe some of its mathematical properties. Numerical tests of the inversion algorithm are discussed by *Goff and Jordan* [1989b], and comparisons between synthetic realizations of the Gaussian model and actual Sea Beam and SeaMARC II data sets are presented by *Goff and Jordan* [1988] and *Goff et al.* [1991]. The data-synthetic comparisons indicate that the model is generally successful at matching the low-order characteristics of abyssal hill terrain. Improvements in the model are anticipated, primarily through improved parameterizations of the two-point correlation function and the addition of higher-order terms in the stochastic characterization [*Goff*, 1990]. However, it is hoped that the preliminary Gaussian models presented here will prove useful in testing numerical schemes for modeling acoustic reverberations generated by small-scale seafloor topography.

Realizations of the stochastic model are used to interpolate, to 1 m resolution, the three 20 km subsets chosen from the V2602 track line. The parameters assumed in computing the stochastic realizations are normally estimated by applying the inversion procedures of *Goff and Jordan* [1988] to multi-narrow beam swaths. In this case, however, the resolution of the single-wide beam data is insufficient to estimate the fractal dimension, and we do not have access to multibeam data in the vicinity. For the realizations generated here, we assume a fractal dimension based on other estimates in the North Atlantic [*Goff*, 1991] and then eyeball the rms height and scale parameter for which the covariance model best fits the covariance estimated from the V2062 profile. Interpolation is accomplished by 'molding' the synthetic topography to the constraints provided by the deterministic profile, as introduced by *Goff and Jordan* [1990] for two dimensional fields. The net effect of molding is to replace the smoother features of the unconstrained stochastic realization with those obtained from the measured profile. The molding algorithm is described in Section 4.

One of the sites chosen for stochastic interpolation is a sediment pond (site A on Figure 2). A seismic record from the V2602 cruise (Figure 3) reveals the large scale structure of the basement of this pond. In this case, this basement structure was digitized and interpolated stochastically, while the bathymetric profile (i.e., the nearly flat sediment pond) was interpolated linearly. Interpolated basement bathymetry and sediment cover are filed separately so that their geophysical properties can be distinguished. No substantial sediment cover can be detected over sites B and C in the seismic profile (Figure 3). However, it is likely that a thin veneer of sediments, undetectable because of its thinness, fills in the nooks and cranies. Filling in the nooks and crannies with sediment may or may not prove important for the acoustic models.

To model the possible contribution of sediments we have employed an efficient numerical algorithm for modeling the sediment distribution on very rough (fractal) models of seafloor topography. The algorithm, developed by *Webb and Jordan* [1991, 1992], is based upon a cellular-automaton description of sediment-particle dynamics. The algorithm is outlined in Section 5.

Technical specifications regarding the V2602 profile and interpolated subsets are given in Section 6.

2. DETERMINISTIC AND STOCHASTIC COMPONENTS OF SEAFLOOR TOPOGRAPHY

We let $z(x)$ be the height of the seafloor above some mean reference level at a position x, and we suppose we have a map of this topography, denoted $z_M(x)$. Because the map is

based on limited data, it may accurately represent age-dependent subsidence, thermal swells, major fracture zones, oceanic plateaus, and other "large-scale" features, but does not contain topographic variations with horizontal dimensions below some "cutoff scale" x_M. We assume the map can be approximated as the output of some filter $M[z(x)]$. To the extent that the mapping cutoff is sharp — i.e., M passes features larger than x_M with no distortion but completely annihilates features smaller than x_M — this filter is a projection operator: $z_M(x) = M[z_M(x)]$. An example of $z_M(x)$, the one used in this report, is the V2602 profile which has been gridded at, and has an effective cutoff scale of 1 km.

We seek to supplement this deterministic description of the seafloor with some stochastic representation of the small-scale features. Let $h(x)$ be a stochastic process, or random field, which represents the statistics of the topographic variation at all length scales. We define $h_M(x) = M[h(x)]$ and take as our model of seafloor topography

$$\tilde{z}(x) = z_M(x) + h(x) - h_M(x) \qquad (1)$$

In other words, we replace the stochastic components of the field with scale lengths greater than the cutoff x_M by the known ("deterministic") components. If M is a projection operator, then applying it to this model recovers the map: $M[\tilde{z}(x)] = z_M(x)$.

3. ONE-DIMENSIONAL GAUSSIAN MODEL OF SMALL-SCALE TOPOGRAPHY

The stochastic model used in this report is a stationary (spatially homogeneous) Gaussian random field with zero mean and a 2-point moment (covariance) function,

$$C_{hh}(x) = \langle h(x_1) \, h(x_1 + x) \rangle \qquad (2)$$

where $\langle \cdot \rangle$ is the expected value and x is the spatial lag vector. Under the Gaussian assumption, all higher moments of the random field can be expressed in terms of (2). The power spectrum of the Gaussian field is the Fourier transform of this covariance function [Bracewell, 1978], and its phase spectrum is a random process uniformly distributed on $(0, 2\pi]$ [Priestly, 1981].

Although the distribution of seafloor depths often fails the Kolmogorov-Smirnov test for acceptance of the Gaussian hypothesis [Gilbert and Malinverno, 1988], approximating small-scale topography by a Gaussian field provides a simple and mathematically convenient description of its most important features [Bell, 1975; Goff and Jordan, 1988]. These include its RMS height variation, the orientation and characteristic wavenumbers of its "tectonic grain," and the variation of roughness with spatial scale. Moreover, a

Gaussian description is the basis for the study of higher-order statistical properties, which can be expressed as perturbations from a Gaussian form [*Goff*, 1990, 1991].

Covariance model. The mathematical properties of the two-dimensional Gaussian process employed in this study are detailed in *Goff and Jordan* [1988, 1989a; 1990]. This model is expressed in a two dimensional form to account for azimuthal anisotropy (tectonic grain). Before specializing to 1-D, we first present the general 2-D form so that the 1-D model may be placed in context with previous work. To represent small-scale abyssal-hill topography, we have proposed a covariance function of the form

$$C_{hh}(\mathbf{x}) = H^2 \, G_\nu(r(\mathbf{x})) \, / \, G_\nu(0) \tag{3}$$

where H is the rms height and G_ν is defined by

$$G_\nu(r) = r^\nu K_\nu(r), \quad 0 \le r < \infty, \quad \nu \in [0,1] \tag{4}$$

K_ν is the modified Bessel function of the second kind of order ν. G_ν is plotted for three values of ν in Figure 4 (top panel). The order parameter ν controls the behavior of $G_\nu(r)$ at the origin; its slope at $r = 0$ is zero for $\nu = 1$ and infinite for $\nu = 0$. $G_{1/2}(r)$ is simply an exponential function.

Azimuthal variation is expressed by the dimensionless ellipsoidal (Riemannian) norm

$$r(\mathbf{x}) = [\mathbf{x}^T \, Q \, \mathbf{x}]^{1/2} = \sqrt{q_{11} x_1^2 + 2 q_{12} x_1 x_2 + q_{22} x_2^2} \tag{5}$$

The scale matrix, Q, can be expressed in terms of its ordered eigenvalues $k_n^2 \ge k_s^2$ and its normalized eigenvectors $\hat{\mathbf{e}}_n$ and $\hat{\mathbf{e}}_s$,

$$Q = k_n^2 \, \hat{\mathbf{e}}_n \hat{\mathbf{e}}_n^T + k_s^2 \, \hat{\mathbf{e}}_s \hat{\mathbf{e}}_s^T \tag{6}$$

Q specifies the "outer scale" of the topography through the characteristic wavenumbers k_n and k_s, yielding an aspect ratio $a = k_n/k_s$ for the lineation or "tectonic grain" of the abyssal hills. The orientation of this anisotropy is given by the directions of the principal axes. Since the covariance decays least rapidly along the $\hat{\mathbf{e}}_s$ axis, the structure tends to be lineated in this direction.

Thus, five parameters determine the 2-D stochastic model: the rms height H, the order parameter ν, the characteristic wavenumbers k_n and k_s, and the azimuth ζ_s of $\hat{\mathbf{e}}_s$ in the geographic reference frame. The scale parameters define an aspect ratio $a = k_n/k_s$.

To specialize to one dimensional surfaces, we choose a profile, or ship track direction $\hat{e}_\theta$ where θ is the angle between the $\hat{e}_s$ and $\hat{e}_\theta$ directions. The lag variable r is then expressed as a function of lag x in the ship track direction:

$$r(x) = k_\theta x, \quad k_\theta = \sqrt{k_s^2 \cos^2\theta + k_n^2 \sin^2\theta} = \left[\hat{e}_\theta^T Q \hat{e}_\theta\right]^{1/2} \tag{7}$$

Only three parameters determine the 1-D stochastic model: rms height H, the order parameter ν, and the scale parameter in the ship track direction k_θ.

Power spectrum. The 1-D power spectrum obtained from Fourier transforming (3) with the 1-D form of r given by (7) is

$$P_h(k) = \frac{\Gamma(\nu + 1/2)}{\Gamma(\nu)} \frac{2H^2 \pi^{1/2} k_\theta^{2\nu}}{(k_\theta^2 + k^2)^{\nu + 1/2}} \tag{8}$$

The one-dimensional forms of the power spectrum at three values of ν are shown in Figure 4 (bottom panel). Equation (8) is a power-law spectrum with a corner wavenumber k_θ. At high wavenumbers the power spectrum decays at a rate $k^{-(\nu+1/2)}$; at low wavenumbers, it is flat.

Hausdorff dimension and self-affine scaling. The Hausdorff (fractal) dimension D of a topographic surface can be related to the asymptotic properties of the covariance function at small lag [*Adler*, 1981]. *Goff and Jordan* [1989] show that the Hausdorff dimension associated with (3) is

$$D = 2 - \nu \tag{9}$$

Decreasing the parameter ν increases the roughness, with the limiting cases of unity and zero corresponding to a Euclidean random field with continuous derivative (D = 1) and one which is "space-filling" (D = 2), respectively. The interum case D = 1.5 (exponential covariance function) corresponds to a Markov process (the Ornstein-Uhlenbeck process) [*Feller*, 1971].

The Hausdorff dimension describes a self-affine scaling relationship at wavenumbers much larger than k_θ [*Goff and Jordan*, 1988, 1989a]. A topographic surface $h(\mathbf{x})$ is self-affine if there exists an $\alpha \in [0,1]$ such that, for all $R > 0$ the topographic difference function $d(\mathbf{x} - \mathbf{x}_0) = h(\mathbf{x}) - h(\mathbf{x}_0)$ is identical in distribution to $R^{-\alpha}d(R\mathbf{x} - R\mathbf{x}_0)$. For the

covariance model (3), *Goff and Jordan* [1988] demonstrate that $\alpha = v$. The self-affine property allows the topography at high wavenumber to be simply interpolated to smaller scales. However, the validity of this interpolation at scales below the resolution of bathymetric mapping devices is hypothetical; some work suggests that the spectral exponent [*Fox and Hayes*, 1985] and aspect ratio [*Goff et al.*, 1991] are scale-variable. On the other hand analysis of a deep-tow record near the Galapagos ridge indicates that, in a rough, recently formed terrain, the topography exhibits very uniform fractal behavior from the kilometer scale down to the 10 meter scale [*Goff and Kleinrock*, 1991]. Small-scale stochastic interpolation using the covariance model (3), including the high-resolution synthetic realizations accompanying this technical report, require testing in the natural-laboratory settings that will be investigated during the ARSRP.

Characteristic scales. Unlike spectral models usually associated with fractals [e.g. *Mandelbrot*, 1983], a random field whose second-order properties are described by (3) or (7) does not have infinite power at zero wavenumber. Rather, the low-wavenumber part of the spectrum is governed by a characteristic length, or outer scale. As discussed in *Goff and Jordan* [1988], the characteristic length in the θ direction, λ_θ, can be defined in terms of the second moment of the covariance function in the θ direction, which yields

$$\lambda_\theta = \frac{2\sqrt{2(v + 1/2)}}{k_\theta}$$

(10)

where k_θ is the scale parameter in the θ direction. λ_n is interpreted as the characteristic abyssal-hill width, and λ_s as the characteristic abyssal-hill length.

4. MOLDING ALGORITHM

The algorithm for stochastic interpolation involves two basic steps: (1) generating a synthetic realization at the desired profile length and data spacing using the stochastic model, and (2) 'molding' the synthetic realization to the constraints provided by the deterministic bathymetry. To generate synthetic realizations, we compute the Fourier spectrum on a regularly spaced wavenumber grid by multiplying the square root of the power spectrum (8) by a phase factor $exp(i\phi)$, where ϕ is a random number uniformly distributed on the interval $[0, 2\pi)$ [*Priestly*, 1981]. The space domain image is then obtained from a fast Fourier transform. A stochastic realization is generated such that its

total length and sample spacing correspond respectively to the length of bathymetric to be interpolated and the desired resolution. This yields the $h(x)$ term in equation (1).

The molding algorithm contains the following steps:

1. The bathymetric profile is regridded at a regular interval (in this case, 1 km spacing). The portion to be stochastically interpolated is first linearly interpolated (another interpolating scheme may be used) to the desired resolution (in this case, 1 m spacing). This step yields the $z_M(x)$ term of equation (1); i.e. it represents a mapping of the seafloor depth $z(x)$.

2. The stochastic realization is subsampled at the same resolution as the regridded bathymetric profile (1 km spacing). This subsampled realization is then linearly interpolated (or by the same scheme that was used to interpolate the bathymetric profile) to the original data spacing of the stochastic realization (1 m). This step yields the $h_M(x)$ term in equation (1).

3. $h_M(x)$ is subtracted from $h(x)$; i.e. the large-scale stochastic morphology is stripped from the stochastic realization. What remains is added to $z_M(x)$ to complete the molding, yielding the $\tilde{z}(x)$ of equation (1). Note that $\tilde{z}(x) = z_M(x)$ where x is equal to one of the original (1 km) grid locations (i.e., $M[\tilde{z}(x)] = z_M(x)$).

The following model parameters were used to generate stochastic realizations: $H = 235$ m, $k_\theta = 0.45$ km^{-1}, and $v = 0.85$ (D = 1.15, $\lambda_\theta = 7.3$ km). Because of the poor resolution of the wide-beam bathymetry, v could not directly be estimated from the V2602 profile. However, the value of $v = 0.85$ is consistent with estimates from narrow beam records from other near-ridge, unsedimented sites in the Atlantic [*Goff*, 1990; 1991]. For this value of v, we estimated values for H and k_θ simply by a fit-by-eye match to the estimated covariance for a portion of the profile in the vicinity of the three interpolated sites (Figure 5).

Figure 6 shows the results of the molding algorithm applied to the basement morphology of site A (compare with Figures 2 and 3). In this figure, the dashed line represents the topography linearly interpolated from the 1 km gridded wide-beam bathymetry, while the solid line represents the 1 m stochastic interpolation. Note that at the location of the 1 km grid points both profiles coincide. The linearly interpolated sediment cover for site A, estimated from the seismic profile (Figure 3), is also shown in Figure 6.

5. SEDIMENTATION ALGORITHM

The existence of sediments may have an important effect on the acoustic response of the seafloor. Sedimentation rates in the vicinity of the acoustic reverberation corridor are on the order of 30 m/my [*Lisitzin*, 1972], and the half-rate of seafloor spreading at this latitude is ~15 km/my [*Tucholke and Schouten*, 1988]. In the absence of any reworking of the

sediment cover, we would expect to see ~270 meters sediment cover at site A (~9 my crustal age), ~510 meters sediment cover at site B (~17 my crustal age), and well over a kilometer of sediment cover at the oldest crustal ages (~40 my) spanned by the acoustic reverberation corridor. A cursory examination of the V2602 seismic profile record (Figure 3) reveals a much more complex relationship between basement age and the sedimentation volume in this region. The basin containing by the greatest volume of sediment (up to 500 m thick) is located at some of the youngest crustal ages on this record (site A). The paucity of sediments at older crustal ages (to the right side of Figure 3) and the fact that all detected sediment volumes are flat-lying indicate that vigorous post-depositional sediment transport processes are operating. No sediments can be detected at sites B and C on the 1 km scale (Figure 3), but we can assume that sediments have been deposited in the nooks and crannies at the 1 m scale and larger, significantly smoothing the surface profile at those scales.

Without a high-resolution, two-dimensional map of the seafloor topography and a better of understanding of the nature of the sediment transport processes, it is difficult to quantify in any precise way the distribution of pelagic sediments in this particular area. For the purposes of prescribing plausible models for numerical modeling of acoustic backscattering, however, it is possible to do some preliminary calculations. *Webb and Jordan* [1991, 1992] have developed an efficient numerical algorithm for calculating the sediment distribution on very rough, one-dimensional models of seafloor topography. The algorithm is based upon a cellular-automation description of sediment-particle kinematics. It consists of the following steps:

1. *Initialization.* A specified basement topography $h^{(0)}(x)$ is discretized on a rectangular grid with vertical spacing δh, horizontal spacing δx, and total horizontal length $X = K \delta x$.

2. *Sediment Accumulation.* Parcels of dimensions $(\delta x, \delta h)$ are accumulated at each horizontal position x_k for M time steps, yielding a topography $h_k = h_k^{(0)} + M \delta h$.

3. *Sediment Redistribution.* Parcels are redistributed for $2N$ time steps. Transport during each time step alternates between right-directed and left-directed sediment flow:

   a. *Right-directed transport.* Beginning at $k = 1$ and moving right to $k = K-1$, h_{k+1} is reset to $h_{k+1} + \Delta h_{k+1}$, where $\Delta h_{k+1} = \min\{(h_k - h_k^{(0)}), -\min[(h_{k+1} - h_k)/2, 0]\}$.

   b. *Left-directed transport.* Beginning at $k = K$ and moving left to $k = 2$, h_{k-1} is reset to $h_{k-1} + \Delta h_{k-1}$, where $\Delta h_{k-1} = \min\{(h_k - h_k^{(0)}), -\min[(h_{k-1} - h_k)/2, 0]\}$.

The sediment-water interface at the end of $2N$ time steps defines a topographic profile $h_k^{(1)}$, which remains fixed during subsequent sediment accumulation and redistribution.

4. Steps (2) and (3) are repeated with $h_k^{(1)}$ replacing $h_k^{(0)}$.

5. The process is iterated to obtain L sediment layers.

Webb and Jordan [1991, 1992] have demonstrated that this cellular-automota algorithm yields a diffusive redistribution process. That is, sediments are transported across a flat basement according to a diffusion equation in which the forcing term for sediment flux is the gradient in sediment thickness. This transport is characterized by a diffusivity κ which scales as the ratio of the redistribution time to the accumulation time,

$$\kappa \sim N / M \tag{11}$$

For a small value of κ, the redistribution rate is low, and sediments drape over the basement topography. For a large value, the rate is high, and sediments are swept downslope and accumulate in topographic lows to form ponds.

The cellular-automota algorithm has been used to redistribute sediments on the basement topography generated by stochastic interpolation for sites B (Figure 7) and C (Figure 8). A sediment volume equal to a layer with a uniform thickness of 20 meters was assumed for both sites. We set κ equal to 4.7×10^{-3} m^2/yr for site B and 2.0×10^{-3} m^2/yr for site C. Although no diffusivities have been estimated for pelagic sedimentation deep oceanic settings, these values are on the order of those observed for the Bonneville shoreline scarp, a region of semiarid hillslope degradation [*Colman and Watson*, 1983; *Hanks et. al* 1984]. They are sufficiently large that sediment ponding occurs, in qualitative agreement with the distribution observed on high-resolution profiles [W. Ryan, personal communication, 1991].

It should be noted that the sediment distributions obtained in Figures 6 and 7 have been generated by an algorithm that allows lateral transport in only one dimension. Allowing transport down topographic slopes in the cross-profile direction will have the effect of making the sediment distribution less uniform. It is possible to extend the Webb-Jordan algorithm to this full three-dimensional problem and to apply it to basement topography stochastically extrapolated out of the plane of the profile. This will be the subject of a future report.

6. TECHNICAL SPECIFICATIONS FOR STOCHASTIC INTERPOLATIONS

The following model parameters were used to generate stochastic realizations: $H = 235$ m, $k_\theta = 0.45$ km^{-1}, and $\nu = 0.85$ ($D = 1.15$, $\lambda_\theta = 7.3$ km).

The following files are available from the first author, all in ASCII format:

1. Original V2602 profile, 'v2602.lld'. Header: number data points. Data format: latitude (decimal degrees N), longitude (decimal degrees E), depth (meters).

(For the remaining files, the header contains the following: number of data points, data spacing in kilometers. The data format is: depth (meters).)

2. Regridded V2602 profile, 'v2602.prof'.

3. Stochastically interpolated site A basement, 'v2602a_si.base'. Site A corresponds to points indexed 111-131 of regridded V2602 profile.

4. Sediment thickness for site A, 'v2602a_si.sed'.

5. Stochastically interpolated site B basement, 'v2602b_si.base'. Site B corresponds to points indexed 235-255 of regridded V2602 profile.

6. Sediment thickness for site B, 'v2602b_si.sed'.

7. Stochastically interpolated site C basement, 'v2602c_si.base'. Site C corresponds to points indexed 131-151 of regridded V2602 profile.

8. Sediment thickness for site C, 'v2602c_si.sed'.

The surface profile for any site is generated simply by adding the '.base' and '.sed' files. To obtain files either by telnet mail or FTP, contact John Goff at goff@jeffreys.whoi.edu (telnet address 128.128.16.216).

7. REFERENCES

Adler, R. J., *The Geometry of Random Fields*, 280 pp., John Wiley, New York, 1981.

Bell, T. H., Statistical features of sea-floor topography, *Deep Sea Res.*, 22, 883-892, 1975.

Bracewell, R., *The Fourier Transform and its Applications*, 381 pp., McGraw-Hill, New York, 1978.

Colman, S. M., and K. Watson, Ages estimated from a diffusion equation model for scarp degradation, *Science*, 221, 263-265, 1983.

Feller, W., *An Introduction to Probability Theory and Its Applications*, Vol. 2, 669 pp., John Wiley, New York, 1971.

Fox, C. G., and D. E. Hayes, Quantitative methods for analyzing the roughness of the seafloor, *Rev. Geophys.*, **23**, 1-48, 1985.

Gilbert, L. E., and A. Malinverno, A characterization of the spectral density of residual ocean floor topography, *Geophys. Res. Lett.*, **15**, 1401-1404, 1988.

Goff, J. A., Stochastic Modeling of Seafloor Morphology (Ph.D. Thesis), Massachusetts Institute of Technology/Woods Hole Oceanographic Institution, Cambridge, 266 pp., 1990.

Goff, J. A., A global and regional stochastic analysis of near-ridge abyssal hill morphology, submitted to *J. Geophys. Res.*, 1991.

Goff, J. A., and T. H. Jordan, Stochastic modeling of seafloor morphology: inversion of Sea Beam data for second-order statistics, *J. Geophys. Res.*, **93**, 13589-13609, 1988.

Goff, J. A., and T. H. Jordan, Stochastic modeling of seafloor morphology: a parameterized Gaussian model, *Geophys. Res. Lett.*, **16**, 45-48, 1989a.

Goff, J. A., and T. H. Jordan, Stochastic modeling of seafloor morphology: resolution of topographic parameters by Sea Beam data, *IEEE J. Oceanic Eng*, **14**, 326-337, 1989b.

Goff, J. A., and T. H. Jordan, Pacific and Atlantic models of small-scale seafloor topography, *Office of Naval Research S. R. P. on Acoustic Reverberation*, Technical Report No. 1, 1990.

Goff, J. A, T. H. Jordan, M. H. Edwards, and D. J. Fornari, Comparison of a stochastic seafloor model with SeaMARC II bathymetry and Sea Beam data near the East Pacific Rise 13° - 15° N, *J. Geophys. Res.*, **96**, 3867-3885, 1991.

Goff, J. A., and M. C. Kleinrock, Quantitative comparison of bathymetric survey systems, submitted to *Geophys. Res. Lett.*, 1991.

Hanks, T. C., R. C. Bucknam, K. R. Lajoie, and R. E. Wallace, Modification of wave-cut and faulting-controlled landforms, *J. Geophys. Res.*, **89**, 5771-5790, 1984.

Lisitzin, A. P., *Sedimentation in the World Ocean*, 218 pp., Society of Economic Paleontologists and Mineralogists, Spec. Pub. 17, Tulsa, 1972.

Mandelbrot, B. B., *The Fractal Geometry of Nature*, 468 pp., W. H. Freeman, New York, 1983.

Priestly, M. B., *Spectral Analysis and Time Series*, 890 pp., Academic, San Diego, 1981.

Tucholke, B. E., and H. Schouten, Kane Fracture Zone, *Mar. Geophys. Res.*, **10**, 1-39, 1988.

Webb, H., and T. H. Jordan, Distribution of sediments on a rough seafloor (abstract), *Eos, Trans. AGU*, **72**, 269, 1991.

Webb, H., and T. H. Jordan, A cellular-automaton model for pelagic sedimentation on a rough seafloor, *Geophys. Res. Lett.*, submitted, 1992.

8. FIGURES

Figure 1. Track line of the V2602 bathymetric profile and seismic record through the ARSRP acoustic reverberation corridor (dashed box). Tick marks are spaced every 100 data points. x's within box represent preliminary acoustic target sites for the upcomming ARSRP acoustic reconnaissance experiment. The Mid-Atlantic Ridge plate boudary is also shown, with double lines representing spreading ridge segments, and single lines representing ridge offsets.

Figure 2. V2602 wide beam bathymetric profile. For consistency with the seismic profile (Figure 3), East is to the left. 20 km sections chosen for stochastic interpolation are marked as sites A, B, and C. These sites correspond to the nearest points of passage to the respective sites A, B, and C marked in Figure 1. The axis of the Mid-Atlantic Ridge (MAR) is also marked.

Figure 3. V2602 seismic profile. Compare with bathymetric profile in Figure 2. This record was used to digitize the basement depths for site A. Note general absence of sediments at older crustal ages (crustal age progresses left-to-right).

Figure 4. Functional form of the model covariance function $G_\nu(r)$, plotted for values of $\nu = 0$, 1/2, and 1 (top panel), and their normalized Fourier transforms plotted on a log-log scale (bottom panel).

Figure 5. Covariance function estimated from a 200 km section of the V2602 profile (solid curve) and fit-by-eye covariance model (dashed curve) (Equation 3). The 200 km subset begins at 140 km and ends at 340 km from the beginning of the V2602 profile. The parameters used in the covariance model are $H = 195$ m, $k_\theta = 0.45$ km^{-1}, and $\nu = 0.85$ (D = 1.15, $\lambda_\theta = 7.3$ km).

Figure 6. Stochastically interpolated basement depth for site A (bottom solid curve) with measured sediment cover (top solid curve). Dashed lines represent 1-km gridded basement depths which were used to constrain the large-scale behavior of the stochastic realization.

Figure 7. Stochastically interpolated basement depth for site B (bottom solid cuvre) with numerically generated sediment cover (top solid curve). The average sediment cover is 20

---

m. Dashed lines represent 1-km gridded basement depths which were used to constrain the large-scale behavior of the stochastic realization.

Figure 8. Stochastically interpolated basement depth for site C (bottom solid curve) with numerically generated sediment cover (top solid curve). The average sediment cover is 20 m. Dashed lines represent 1-km gridded basement depths which were used to constrain the large-scale behavior of the stochastic realization.

Figure 1

V2602

Figure 2

500 m

100 km

Figure 3

Figure 4

COVARIANCE, m²

LAG, km

50000

10

-10
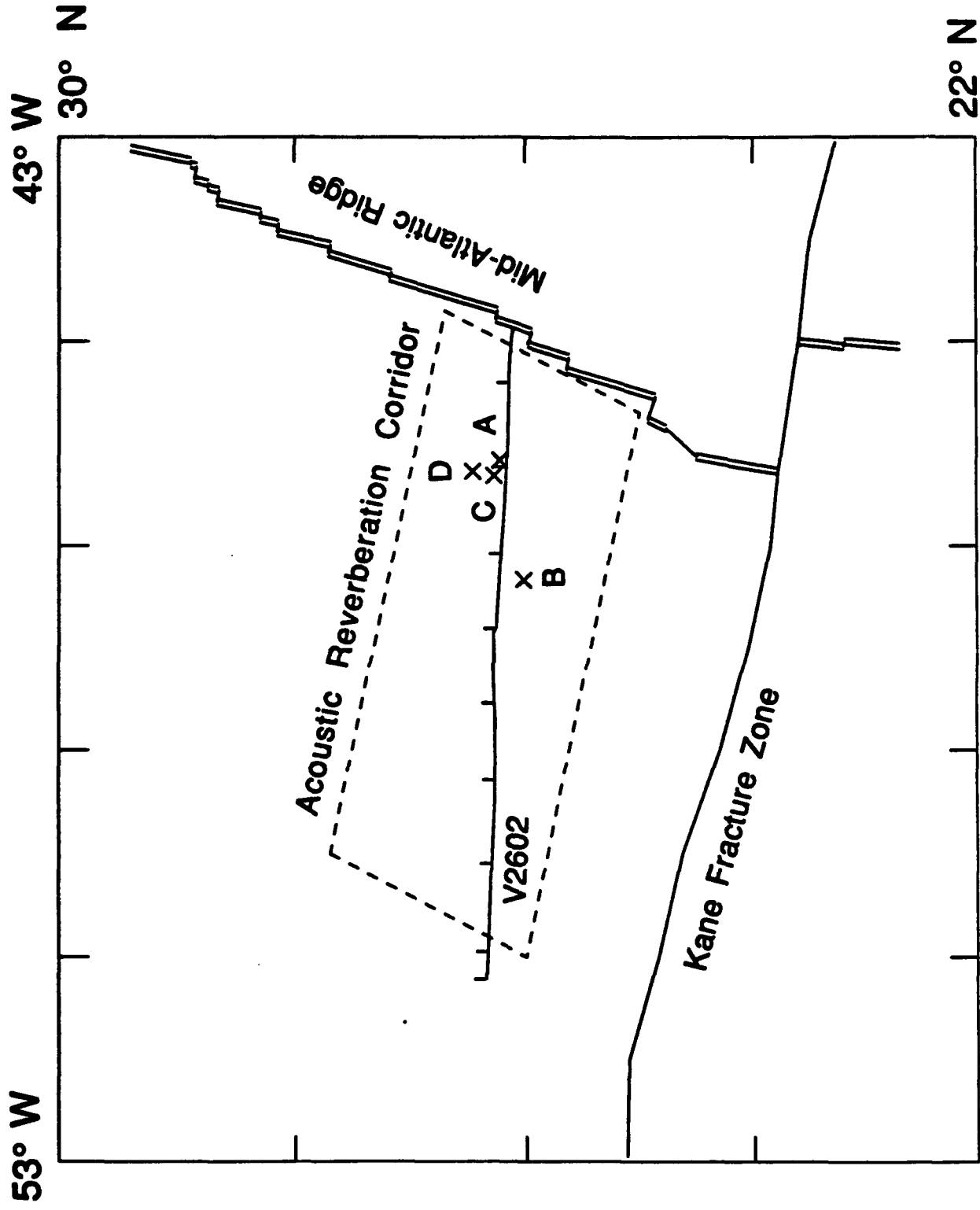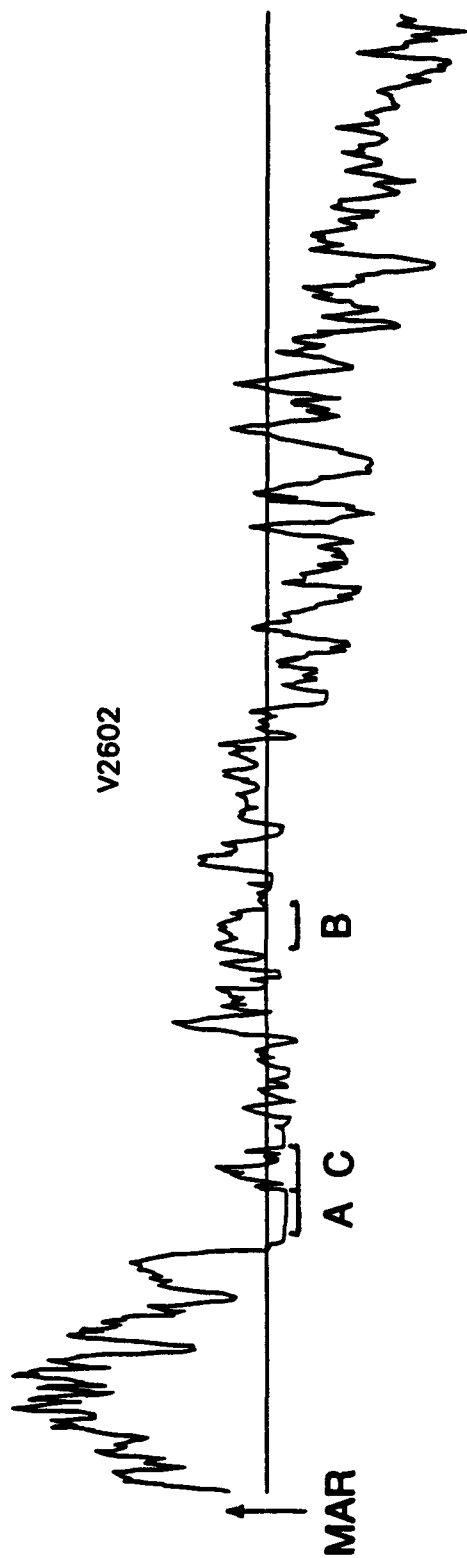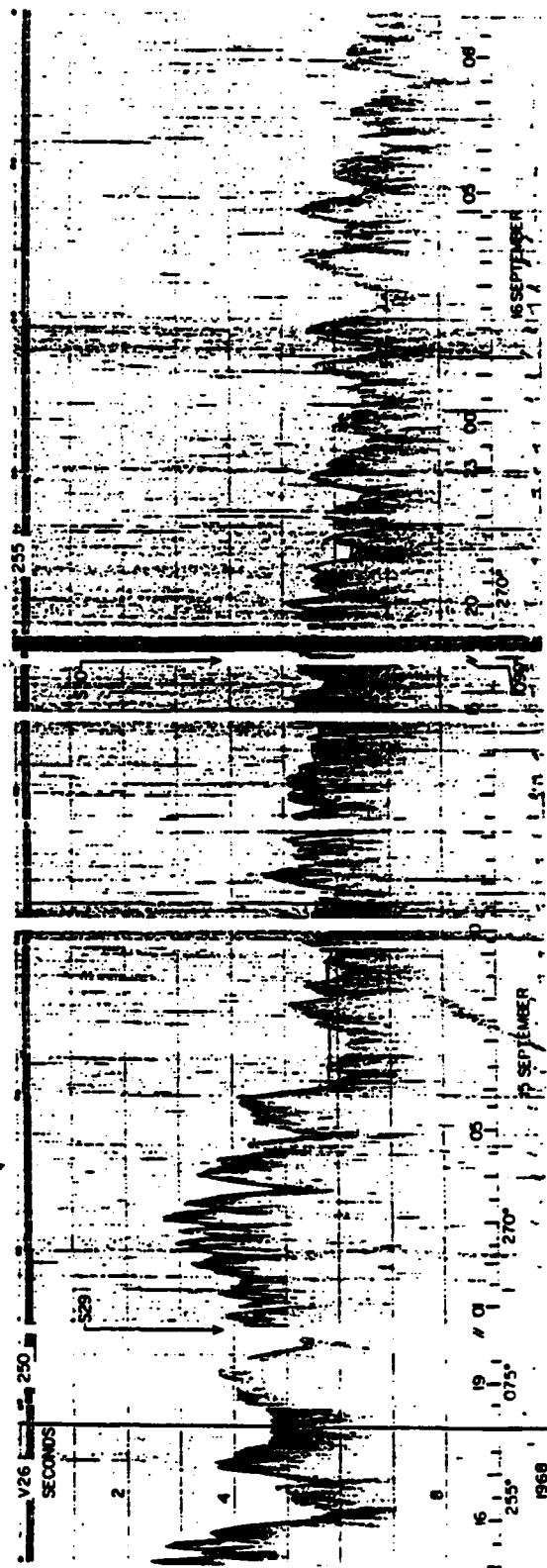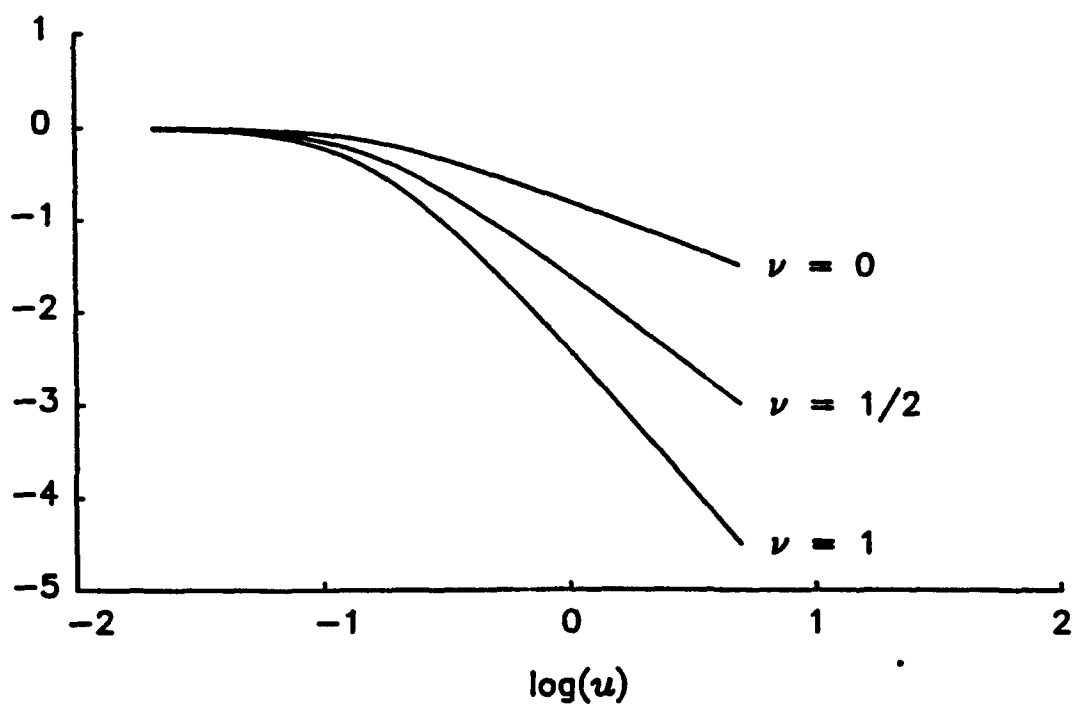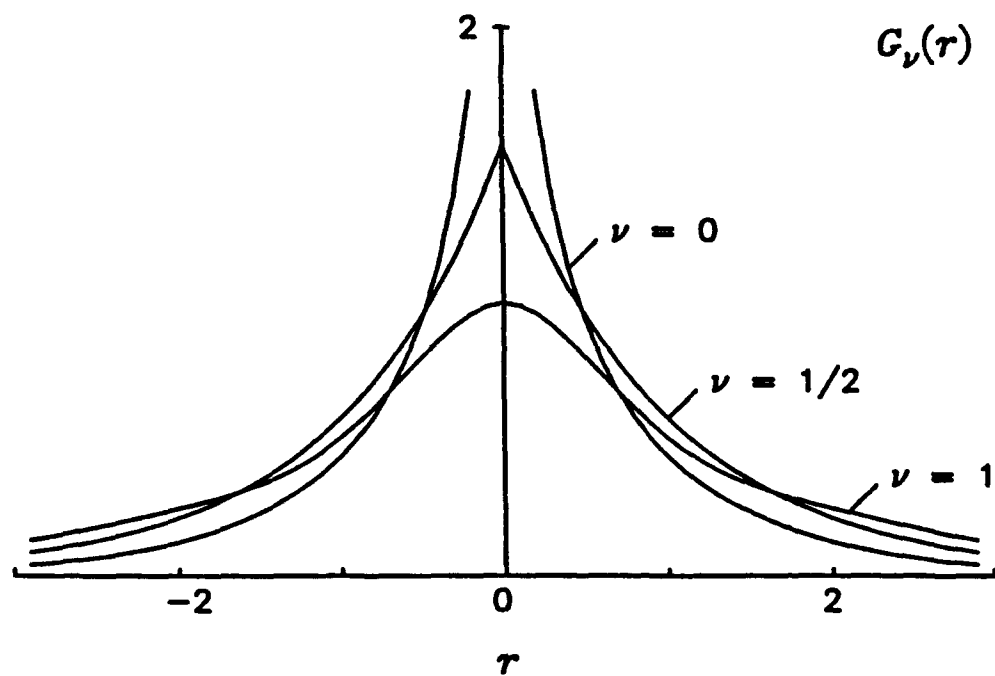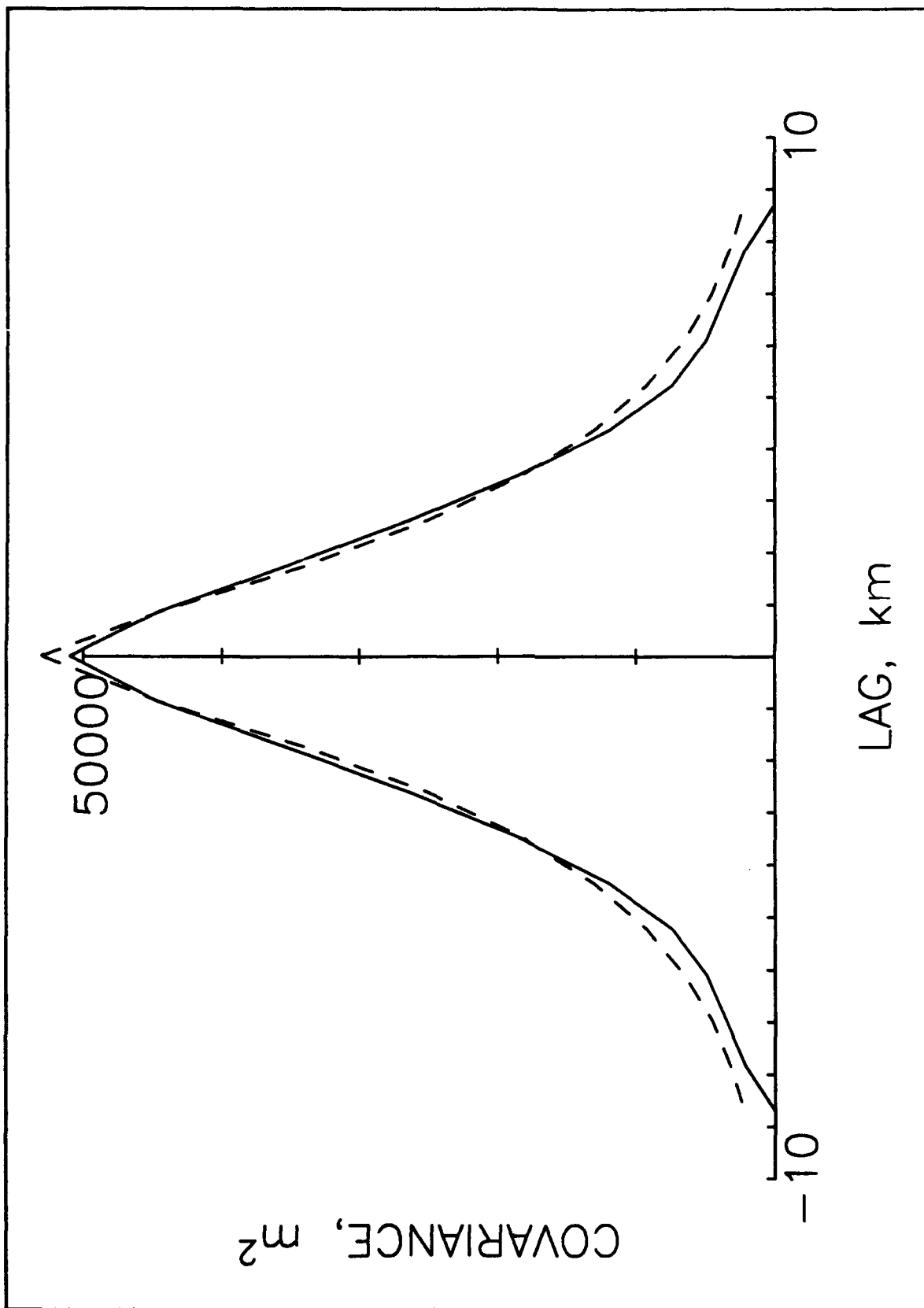
Figure 5
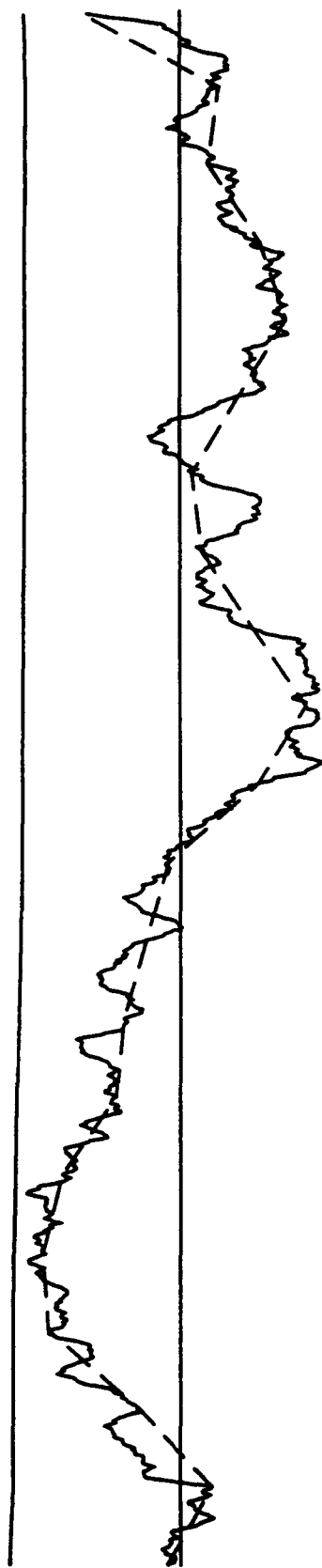
V2602 Site A

100 m

2 km

Figure 6

V2602 Site B

100 m

2 km

Figure 7

V2602 Site C

100 m

2 km

Figure 8